



Higgs boson production cross-section measurements and their EFT interpretation in the 4ℓ decay channel at $\sqrt{s} = 13$ TeV with the ATLAS detector

ATLAS Collaboration*

CERN, 1211 Geneva 23, Switzerland

Received: 8 April 2020 / Accepted: 9 July 2020 / Published online: 16 October 2020
© CERN for the benefit of the ATLAS collaboration 2020, corrected publication 2020

Abstract Higgs boson properties are studied in the four-lepton decay channel (where lepton = e, μ) using 139 fb^{-1} of proton–proton collision data recorded at $\sqrt{s} = 13$ TeV by the ATLAS experiment at the Large Hadron Collider. The inclusive cross-section times branching ratio for $H \rightarrow ZZ^*$ decay is measured to be $1.34 \pm 0.12 \text{ pb}$ for a Higgs boson with absolute rapidity below 2.5, in good agreement with the Standard Model prediction of $1.33 \pm 0.08 \text{ pb}$. Cross-sections times branching ratio are measured for the main Higgs boson production modes in several exclusive phase-space regions. The measurements are interpreted in terms of coupling modifiers and of the tensor structure of Higgs boson interactions using an effective field theory approach. Exclusion limits are set on the CP-even and CP-odd ‘beyond the Standard Model’ couplings of the Higgs boson to vector bosons, gluons and top quarks.

Contents

1	Introduction	1
1.1	Simplified template cross-sections	2
1.2	Higgs boson couplings in the κ -framework	3
1.3	Tensor structure of Higgs boson couplings in the effective field theory approach	4
2	ATLAS detector	5
3	Data set and event simulation	5
4	Event selection	7
4.1	Event reconstruction	7
4.2	Selection of the Higgs boson candidates	8
5	Event categorisation and production mode discrimination	11
5.1	Event categorisation	11
5.2	Multivariate production mode discriminants	12
6	Background contributions	15
6.1	Background processes with prompt leptons	15

6.2	Background processes with non-prompt leptons	15
7	Systematic uncertainties	17
7.1	Experimental uncertainties	17
7.2	Theoretical uncertainties	19
8	Measurement of the Higgs boson production mode cross-sections	20
8.1	Observed data	20
8.2	Measurement of simplified template cross-sections	21
9	Constraints on the Higgs boson couplings in the κ -framework	27
10	Constraints on the tensor coupling structure in the EFT approach	28
10.1	EFT signal model	29
10.2	EFT interpretation results	30
11	Conclusion	33
	References	35

1 Introduction

The observation of the Higgs boson by the ATLAS and CMS experiments [1,2] with the Large Hadron Collider (LHC) Run 1 data set at centre-of-mass energies of $\sqrt{s} = 7$ TeV and 8 TeV was a major step towards an understanding of the electroweak (EW) symmetry breaking mechanism [3–5]. Tests of its spin and CP quantum numbers strongly indicate that the observed particle is of scalar nature and that the dominant coupling structure is CP-even, consistent with the Standard Model (SM) expectation [6–8]. The measurements of the Higgs boson production and differential cross-sections, branching ratios, and the derived constraints on coupling-strength modifiers, assuming the SM coupling structure, have also shown no significant deviation from the predictions for the SM Higgs boson with a mass of 125 GeV [9–12]. Furthermore, constraints have been set on various coupling parameters beyond the SM (BSM) that modify the tensor structure of the Higgs boson couplings to SM particles [8, 13–20].

* e-mail: atlas.publications@cern.ch

Motivated by a clear Higgs boson signature and a high signal-to-background ratio in the $H \rightarrow ZZ^* \rightarrow 4\ell$ decay channel (where $\ell = e$ or μ), the updated measurements of the Higgs boson coupling properties in this channel are presented using the entire Run 2 data set with 139 fb^{-1} of proton–proton (pp) collision data collected at $\sqrt{s} = 13 \text{ TeV}$ by the ATLAS detector between 2015 and 2018. Three types of results are presented in this paper: (i) measurements of the Higgs boson production cross-sections times branching ratio, hereafter referred to as cross-sections, for the main production modes in several exclusive phase-space bins in dedicated fiducial regions; (ii) interpretation of the measurements in terms of constraints on the Higgs boson coupling-strength modifiers within the κ -framework [21]; and (iii) interpretation of the measurements in terms of modifications to the tensor structure of Higgs boson couplings using an effective field theory (EFT) approach.

In addition to a nearly four times higher integrated luminosity, there are several other important differences compared to the previous results in this analysis channel [17]:

- an improved lepton isolation to mitigate the impact of additional pp interactions in the same or neighbouring bunch crossings (pile-up),
- an improved jet reconstruction using a particle flow algorithm [22],
- additional event categories for the classification of Higgs boson candidates,
- new discriminants to enhance the sensitivity to distinguish the various production modes of the SM Higgs boson,
- the use of data sidebands to constrain the dominant ZZ^* background process,
- a dedicated control region to constrain the background in the reconstructed event categories probing ttH production,
- improved estimates of Z +jets, tt , and WZ backgrounds, and
- an EFT interpretation, based on a parameterisation of the cross-sections rather than a direct parameterisation of the reconstructed event yields.

1.1 Simplified template cross-sections

In the framework of *Simplified Template Cross Sections* (STXS) [23–25], exclusive regions of phase space are defined for each Higgs boson production mechanism. These phase-space regions, referred to as production bins, are defined to reduce the dependence on theoretical uncertainties that directly fold into the measurements and at the same time maximise the experimental sensitivity to measure the bins, enhance the contribution from possible BSM effects, and allow measurements from different Higgs boson decay

modes to be combined. The number of production bins is limited to avoid loss of measurement sensitivity for a given amount of integrated luminosity.

The definitions of the production bins used for this measurement are shown in the left panel of Fig. 1 (shaded area). All production bins are defined for Higgs bosons with rapidity $|y_H| < 2.5$ and no requirement is placed on the particle-level leptons. Two sets of production bins with different granularity are considered, as a trade-off between statistical and theoretical uncertainties.

The first set of production bins (Production Mode Stage) [24] is defined according to the Higgs boson production modes: gluon–gluon fusion (ggF), vector-boson fusion (VBF) and associated production with vector bosons (VH , where $V = W$ or Z) or top quark pairs (ttH). Since b -jets from bbH associated production are emitted at small angles relative to the beam axis and usually outside of the detector acceptance, the bbH and ggF Higgs boson production modes have similar signatures and acceptances. Their contributions are considered together with their relative ratio fixed to the SM prediction. In the following, the sum of their contributions is referred to as ggF. Similarly, single top production (tH) is considered together with ttH , with their relative ratio fixed to the SM prediction. In contrast to the Stage-0 production bins described in Ref. [24], the VH events with hadronic decays of the vector boson V are included in the VH production bin rather than in the ggF or VBF bins. In this way, each of the four main Higgs boson production modes can be measured separately.

The second set of production bins (Reduced Stage 1.1) is more exclusive than the first one. Starting from the production bins of a more granular Stage 1.1 set [25], several production bins are merged as the full set of bins cannot be measured separately in the $H \rightarrow ZZ^* \rightarrow 4\ell$ channel with the current data sample. The definitions of the bins are based on the multiplicity of particle-level jets, the Higgs boson transverse momentum p_T^H and the invariant mass m_{jj} of the two jets with the highest transverse momentum. Particle-level jets are built from all stable particles (particles with lifetime $c\tau > 10 \text{ mm}$) including neutrinos, photons, and leptons from hadron decays or those produced in the parton shower. The anti- k_t jet reconstruction algorithm [26,27] with a radius parameter $R = 0.4$ is used. All Higgs boson decay products, as well as the leptons and neutrinos from the decays of the associated V bosons are excluded from the jet building, while the decay products from hadronically decaying associated V bosons, are included. The jets are required to have $p_T > 30 \text{ GeV}$, with no restrictions on rapidity.

Events from ggF production and $gg \rightarrow ZH$ production with a hadronically decaying Z boson are split into seven common production bins. Six bins have a Higgs boson transverse momentum below 200 GeV , while the seventh bin with

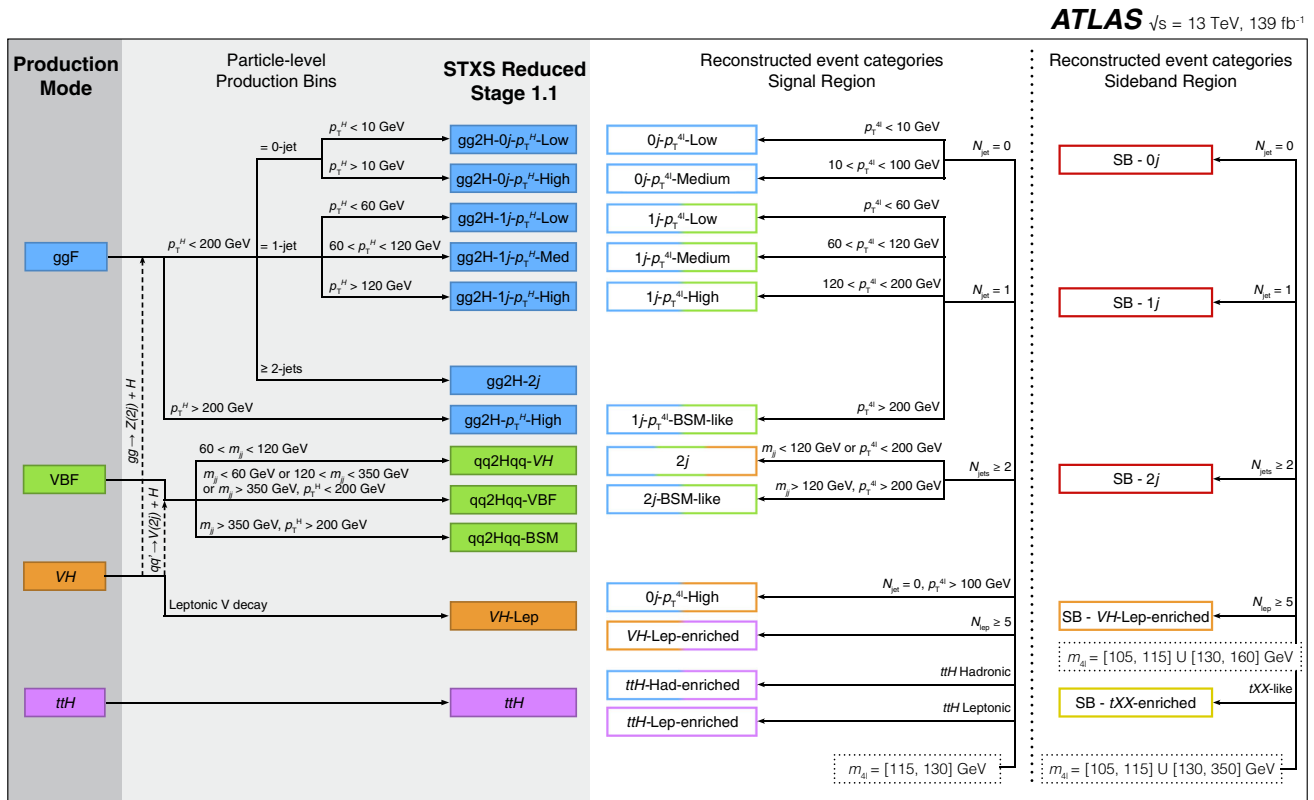


Fig. 1 Two sets (Production Mode Stage and Reduced Stage 1.1) of exclusive phase-space regions (production bins) defined at particle-level for the measurement of the Higgs boson production cross-sections (left and middle-left shaded panels), and the corresponding reconstructed event categories for signal (middle-right panel) and sidebands (right panel). The description of the production bins is given in Sect. 1.1,

while the reconstructed signal region and sideband event categories are described in Sects. 5 and 6, respectively. The bbH (tH) contribution is included in the ggF (ttH) production bins. The colours of each reconstructed event category box indicates the contributions from the relevant production processes

Higgs boson transverse momentum above 200 GeV (gg2H- $0j$ - p_T^H -High) is sensitive to contributions from BSM physics. For p_T^H below 200 GeV, further splits are made according to the jet multiplicity and p_T^H . Events with no jets are split into two bins with p_T^H below and above 10 GeV. Events with one jet are split into three bins with p_T^H below 60 GeV, between 60 and 120 GeV, and above 120 GeV. Finally, Higgs boson events with two or more jets are combined into one bin. The bins are respectively denoted by gg2H- $0j$ - p_T^H -Low, gg2H- $0j$ - p_T^H -High, gg2H- $1j$ - p_T^H -Low, gg2H- $1j$ - p_T^H -Med, gg2H- $1j$ - p_T^H -High and gg2H- $2j$.

As described in Ref. [25], VBF and VH production with hadronically decaying V bosons represent the t -channel and s -channel contributions to the same electroweak qqH production process and are therefore considered together for further splitting. Three bins are defined: one bin, sensitive to BSM contributions (qq2Hqq-BSM), with p_T^H above 200 GeV and m_{jj} above 350 GeV; one bin (qq2Hqq-VH) with m_{jj} between 60 and 120 GeV to target the VH production mode; and one bin (qq2Hqq-VBF) with the Higgs boson not satisfying these criteria to ensure sensitivity to the

VBF process. qqH events in which one or both jets have transverse momenta below the 30 GeV threshold are treated as a part of the qq2Hqq-VBF bin.

The VH process with the associated V boson decaying leptonically is considered separately (VH-Lep). The leptonic decay includes the decays into τ -leptons and neutrino pairs. The ttH production bin remains the same as in the Production Mode Stage.

The middle-right and right panels of Fig. 1 summarise the corresponding categories of reconstructed events in which the cross-section measurements and background estimations are performed. These are described in detail in Sect. 5.

1.2 Higgs boson couplings in the κ -framework

To probe physics beyond the SM, the measured production cross-sections are interpreted within a leading-order-motivated κ -framework [21], in which a set of coupling modifiers $\bar{\kappa}$ is introduced to parameterise deviations from the SM predictions of the Higgs boson couplings to SM bosons and fermions. The framework assumes that the data origi-

nate from a single CP-even Higgs boson state with a mass of 125 GeV and the tensor coupling structure of the SM for its interactions. Only the coupling strengths are allowed to be modified by the BSM processes. The Higgs boson width is assumed to be small enough such that the narrow-width approximation is valid, allowing the Higgs boson production and decay to be factorised:

$$\sigma \cdot \mathcal{B}(i \rightarrow H \rightarrow f) = \sigma_i(\vec{\kappa}) \cdot \frac{\Gamma_f(\vec{\kappa})}{\Gamma_H(\vec{\kappa})},$$

where σ_i is the production cross-section via the initial state i , \mathcal{B} and Γ_f are the branching ratio and partial decay width for the decay into the final state f , respectively, and Γ_H is the total width of the Higgs boson. For a Higgs boson production and decay process via couplings i and f , respectively, coupling-strength modifiers are defined as

$$\kappa_i^2 = \frac{\sigma_i}{\sigma_i^{\text{SM}}} \quad \text{and} \quad \kappa_f^2 = \frac{\Gamma_f}{\Gamma_f^{\text{SM}}},$$

so that

$$\sigma \cdot \mathcal{B}(i \rightarrow H \rightarrow f) = \kappa_i^2 \cdot \kappa_f^2 \cdot \sigma_i^{\text{SM}} \cdot \frac{\Gamma_f^{\text{SM}}}{\Gamma_H(\kappa_i^2, \kappa_f^2)}.$$

1.3 Tensor structure of Higgs boson couplings in the effective field theory approach

The κ -framework assumes that the tensor structure of the Higgs boson couplings is the same as in the SM. In order to probe for possible non-SM contributions to the tensor structure of the Higgs boson couplings, the measured simplified template cross-sections are interpreted using an EFT approach. In this approach, which exploits exclusive kinematical regions of the Higgs boson production and decay phase space, the BSM interactions are introduced via additional higher-dimensional operators $\mathcal{O}_i^{(d)}$ of dimension d , supplementing the SM Lagrangian \mathcal{L}_{SM} ,

$$\mathcal{L}_{\text{EFT}} = \mathcal{L}_{\text{SM}} + \sum_i \frac{C_i^{(d)}}{\Lambda^{(d-4)}} \mathcal{O}_i^{(d)} \quad \text{for } d > 4.$$

The parameters $C_i^{(d)}$ specify the strength of new interactions and are known as the *Wilson coefficients*, and Λ is the scale of new physics. Only dimension-six operators are considered for this paper, since the dimension-five and dimension-seven operators violate lepton and baryon number conservation and the impact of higher-dimensional operators is expected to be suppressed by more powers of the cutoff scale Λ [28]. For energies less than the scale of new physics, only the ratio $c_i = C_i^{(d=6)}/\Lambda^2$ can be constrained by the data.

Constraints are set on the Wilson coefficients defined within the Standard Model Effective Field Theory (SMEFT) formalism [29] in the Warsaw basis [30]. The measurements in the $H \rightarrow ZZ^* \rightarrow 4\ell$ channel do not provide sensitivity

for simultaneous constraints on the full set of these coefficients. To reduce the number of relevant parameters, a minimal flavour-violating scenario is assumed and only operators affecting the Higgs boson cross-section at tree level are considered. Operators affecting only double Higgs boson production and those affecting the Higgs boson couplings to down-type quarks and leptons are neglected due to limited sensitivity. The impact of these operators on the total Higgs boson decay width is also neglected.

The remaining ten operators (see Table 1) comprise five CP-even and five CP-odd ones. The CP-even operators describing interactions between the Higgs boson and gluons and the top-Yukawa interactions are associated with the Wilson coefficients c_{HG} and c_{tH} from Ref. [29], respectively. Similarly, the CP-even Higgs boson interactions with vector bosons are related to c_{HW} , c_{HB} , and c_{HWB} that impact the VBF and VH production and the Higgs boson decay into Z bosons. The Wilson coefficients for the corresponding CP-odd operators are $c_{\tilde{u}H}$, $c_{H\tilde{G}}$, $c_{H\tilde{W}}$, $c_{H\tilde{B}}$ and $c_{H\tilde{W}B}$.

The constraints on the Wilson coefficients can be derived by comparing the expected with the measured simplified template cross-sections. For that purpose, the corresponding expected signal production cross-sections, the branching ratio and the signal acceptances are parameterised in terms of the Wilson coefficients. The dependence of signal production cross-sections on the EFT parameters can be obtained from its separation into three components:

$$\begin{aligned} \sigma \propto |\mathcal{M}_{\text{SMEFT}}|^2 &= \left| \mathcal{M}_{\text{SM}} + \sum_i \frac{C_i}{\Lambda^2} \mathcal{M}_i \right|^2 \\ &= |\mathcal{M}_{\text{SM}}|^2 + \sum_i 2\text{Re}(\mathcal{M}_{\text{SM}}^* \mathcal{M}_i) \frac{C_i}{\Lambda^2} \\ &\quad + \sum_{ij} 2\text{Re}(\mathcal{M}_i^* \mathcal{M}_j) \frac{C_i C_j}{\Lambda^4}, \end{aligned}$$

where the first term on the right-hand side is the squared matrix element for the SM, the second term represents the interference between the SM and dimension-six EFT amplitudes and the third term comprises the pure BSM contribution from dimension-six EFT operators alone. Following this expression, the dependence of the Higgs boson cross-section $\sigma^p(\vec{c})$ in a given production bin p on a set of Wilson coefficients \vec{c} is parameterised relative to the SM prediction σ_{SM}^p as

$$\frac{\sigma^p(\vec{c})}{\sigma_{\text{SM}}^p} = 1 + \sum_i A_i^p c_i + \sum_{ij} B_{ij}^p c_i c_j, \quad (1)$$

where the coefficients A_i^p and B_{ij}^p are independent of \vec{c} and are determined from simulation. A similar procedure is applied to obtain from simulation the EFT parameterisation of the branching ratio $\mathcal{B}^{4\ell}$ for the $H \rightarrow ZZ^* \rightarrow 4\ell$ decay from the partial ($\Gamma^{4\ell}$) and total decay width (Γ^{tot}) param-

Table 1 Summary of EFT operators in the SMEFT formalism that are probed in the $H \rightarrow ZZ^* \rightarrow 4\ell$ channel. The corresponding tensor structure in terms of the SM fields from Ref. [29] is shown together with the associated Wilson coefficients, the affected production vertices and the impact on the $H \rightarrow ZZ^*$ decay vertex. The Higgs doublet field and its complex conjugate are denoted as H and \tilde{H} , respectively. The left-handed quark doublets of flavour p (the right-handed up-type

quarks) are denoted $q_p (u_r)$. $V_{\mu\nu}$ ($\tilde{V}_{\mu\nu} = \epsilon^{\mu\nu\rho\sigma} V_{\rho\sigma}$) is the (dual) field strength tensor for a given gauge field $V = G, W, B$. The bosonic operators with (without) a dual field strength tensor are CP-odd (CP-even). For the remaining operator with fermions (\mathcal{O}_{uH}), the CP-odd contribution is introduced through the non-vanishing imaginary part of the corresponding Wilson coefficient, denoted as $c_{\tilde{u}H}$

CP-even			CP-odd			Impact on	
Operator	Structure	Coeff.	Operator	Structure	Coeff.	production	decay
\mathcal{O}_{uH}	$HH^\dagger \bar{q}_p u_r \tilde{H}$	c_{uH}	\mathcal{O}_{uH}	$HH^\dagger \bar{q}_p u_r \tilde{H}$	$c_{\tilde{u}H}$	$t\bar{t}H$	-
\mathcal{O}_{HG}	$HH^\dagger G_{\mu\nu}^A G^{\mu\nu A}$	c_{HG}	$\mathcal{O}_{H\tilde{G}}$	$HH^\dagger \tilde{G}_{\mu\nu}^A G^{\mu\nu A}$	$c_{H\tilde{G}}$	ggF	Yes
\mathcal{O}_{HW}	$HH^\dagger W_{\mu\nu}^I W^{\mu\nu I}$	c_{HW}	$\mathcal{O}_{H\tilde{W}}$	$HH^\dagger \tilde{W}_{\mu\nu}^I W^{\mu\nu I}$	$c_{H\tilde{W}}$	VBF, VH	Yes
\mathcal{O}_{HB}	$HH^\dagger B_{\mu\nu} B^{\mu\nu}$	c_{HB}	$\mathcal{O}_{H\tilde{B}}$	$HH^\dagger \tilde{B}_{\mu\nu} B^{\mu\nu}$	$c_{H\tilde{B}}$	VBF, VH	Yes
\mathcal{O}_{HWB}	$HH^\dagger \tau^I W_{\mu\nu}^I B^{\mu\nu}$	c_{HWB}	$\mathcal{O}_{H\tilde{W}B}$	$HH^\dagger \tau^I \tilde{W}_{\mu\nu}^I B^{\mu\nu}$	$c_{H\tilde{W}B}$	VBF, VH	Yes

terisations,

$$\begin{aligned}
 \mathcal{B}^{4\ell}(\vec{c}) &= \frac{\Gamma^{4\ell}(\vec{c})}{\Gamma^{\text{tot}}(\vec{c})} \\
 &= \mathcal{B}_{\text{SM}}^{4\ell} \cdot \frac{1 + \sum_i A_i^{4\ell} c_i + \sum_{ij} B_{ij}^{4\ell} c_i c_j}{1 + \sum_f \left(\sum_i A_i^f c_i + \sum_{ij} B_{ij}^f c_i c_j \right)}, \quad (2)
 \end{aligned}$$

where the total decay width is the sum of all partial decay widths Γ^f related to the decay mode f . The procedure for the parameterisation of the cross-sections and the branching ratios is described in more detail in Ref. [31]. The criteria employed in the selection of four-lepton candidates introduce an additional dependence of the signal acceptance on the EFT parameters. This is taken into account in the interpretation, as discussed in Sect. 10.

2 ATLAS detector

The ATLAS detector [32–34] at the LHC is a multipurpose particle detector with a forward–backward symmetric cylindrical geometry¹ and a nearly 4π coverage in solid angle. It consists of an inner tracking detector (ID) surrounded by a thin superconducting solenoid, which provides a 2 T axial magnetic field, electromagnetic (EM) and hadron calorimeters, and a muon spectrometer (MS). The inner tracking detector covers the pseudorapidity range $|\eta| < 2.5$. It consists of silicon pixel, silicon microstrip, and transition radiation tracking detectors. A lead/liquid-argon (LAr) sampling

¹ ATLAS uses a right-handed coordinate system with its origin at the nominal interaction point (IP) in the centre of the detector and the z -axis along the beam pipe. The x -axis points from the IP to the centre of the LHC ring, and the y -axis points upwards. Cylindrical coordinates (r, ϕ) are used in the transverse plane, ϕ being the azimuthal angle around the z -axis. The pseudorapidity is defined in terms of the polar angle θ as $\eta = -\ln \tan(\theta/2)$. Angular distance is measured in units of $\Delta R \equiv \sqrt{(\Delta\eta)^2 + (\Delta\phi)^2}$.

calorimeter provides electromagnetic energy measurements in the pseudorapidity range $|\eta| < 3.2$ with high granularity. A steel/scintillator-tile hadron calorimeter covers the central pseudorapidity range ($|\eta| < 1.7$). The endcap and forward regions are instrumented up to $|\eta| = 4.9$ with LAr calorimeters for both the EM and hadronic energy measurements. The calorimeters are surrounded by the MS and three large air-core toroidal superconducting magnets with eight coils each. The field integral of the toroid magnets ranges between 2.0 and 6.0 Tm across most of the detector. The MS includes a system of precision tracking chambers and fast detectors for triggering, covering the region $|\eta| < 2.7$. Events are selected using a first-level trigger implemented in custom electronics, which reduces the event rate to a maximum of 100 kHz using a subset of detector information. Software algorithms with access to the full detector information are then used in the high-level trigger to yield a recorded event rate of about 1 kHz [35].

3 Data set and event simulation

The full ATLAS Run 2 data set, consisting of pp collision data at $\sqrt{s} = 13$ TeV taken between 2015 and 2018, is used for this analysis. The total integrated luminosity after imposing data quality requirements [36] is 139 fb^{-1} .

The production of the SM Higgs boson via gluon–gluon fusion, via vector-boson fusion, with an associated vector boson and with a top quark pair was modelled with the POWHEG-BOX v2 Monte Carlo (MC) event generator [37–39]. For ggF, the PDF4LHC next-to-next-to-leading-order (NNLO) set of parton distribution functions (PDF) was used, while for all other production modes, the PDF4LHC next-to-leading-order (NLO) set was used [40].

The simulation of ggF Higgs boson production used the POWHEG method for merging the NLO Higgs boson + jet

cross-section with the parton shower and the multi-scale improved NLO (MINLO) method [41–44] to simultaneously achieve NLO accuracy for the inclusive Higgs boson production. In a second step, a reweighting procedure (NNLOPS) [45,46], exploiting the Higgs boson rapidity distribution, was applied using the HNNLO program [47,48] to achieve NNLO accuracy in the strong coupling constant α_s . The transverse momentum spectrum of the Higgs boson obtained with this sample is compatible with the fixed-order calculation from HNNLO and the resummed calculation at next-to-next-to-leading-logarithm accuracy matched to NNLO fixed-order with HRES2.3 [49,50].

The matrix elements of the VBF, $qq \rightarrow VH$, and ttH production mechanisms were calculated up to NLO in QCD. For VH production, the MINLO method was used to merge 0-jet and 1-jet events [41,43,51–54]. The $gg \rightarrow ZH$ contribution was modelled at leading order (LO) in QCD.

The production of a Higgs boson in association with a bottom quark pair (bbH) was simulated at NLO with MADGRAPH5_aMC@NLO v2.3.3 [55,56], using the CT10 NLO PDF [57]. The production in association with a single top quark ($tH+X$ where X is either jb or W , defined in the following as tH) [58,59] was simulated at NLO with MADGRAPH5_aMC@NLO v2.6.0 using the NNPDF3.0nlo PDF set [60].

For all production mechanisms, the PYTHIA 8 [61] generator was used for the $H \rightarrow ZZ^* \rightarrow 4\ell$ decay with $\ell = (e, \mu)$ as well as for parton showering, hadronisation and the underlying event. The contribution of the $Z \rightarrow \tau\tau$ decays is shown to have a negligible impact on the final result. The event generator was interfaced to EVTGEN v1.2.0 [62] for simulation of the bottom and charm hadron decays. For the ggF, VBF and VH processes, the AZNLO [63] set of tuned parameters was used, while the A14 [64] set was used for ttH , bbH and tH processes. All signal samples were simulated for a Higgs boson mass $m_H = 125$ GeV.

For additional cross-checks, the ggF sample was also generated with MADGRAPH5_aMC@NLO. This simulation is accurate at NLO QCD accuracy for zero, one and two additional partons merged with the FxFX merging scheme [55,65]. The events were showered using the PYTHIA 8 generator with the A14 set of tuned parameters.

The Higgs boson production cross-sections and decay branching ratios, as well as their uncertainties, are taken from Refs. [21,24,60,66–71]. The ggF production is calculated with next-to-next-to-next-to-leading order (N^3 LO) accuracy in QCD and has NLO electroweak (EW) corrections applied [72–82]. For VBF production, full NLO QCD and EW calculations are used with approximate NNLO QCD corrections [83–85]. The qq - and qg -initiated VH production is calculated at NNLO in QCD and NLO EW corrections are applied [86–94], while gg -initiated VH production is calculated at NLO in QCD. The ttH [95–98], bbH [99–101]

Table 2 The predicted SM Higgs boson production cross-sections (σ) for ggF, VBF and five associated production modes in pp collisions for $m_H = 125$ GeV at $\sqrt{s} = 13$ TeV [21,24,58–60,66–105]. The quoted uncertainties correspond to the total theoretical systematic uncertainties calculated by adding in quadrature the uncertainties due to missing higher-order corrections and PDF+ α_s . The decay branching ratios (\mathcal{B}) with the associated uncertainty for $H \rightarrow ZZ^*$ and $H \rightarrow ZZ^* \rightarrow 4\ell$, with $\ell = e, \mu$, are also given

Production process	σ [pb]
ggF ($gg \rightarrow H$)	48.6 ± 2.4
VBF ($qq' \rightarrow Hqq'$)	3.78 ± 0.08
VH ($qq' \rightarrow VH$)	1.373 ± 0.028
ZH ($qq/gg \rightarrow ZH$)	0.88 ± 0.04
ttH ($qq/gg \rightarrow ttH$)	0.51 ± 0.05
bbH ($qq/gg \rightarrow bbH$)	0.49 ± 0.12
tH ($qq/gg \rightarrow tH$)	0.09 ± 0.01
Decay process	\mathcal{B} [$\cdot 10^{-4}$]
$H \rightarrow ZZ^*$	262 ± 6
$H \rightarrow ZZ^* \rightarrow 4\ell$	1.240 ± 0.027

and tH [58,59] processes are calculated to NLO accuracy in QCD. The total branching ratio is calculated in the SM for the $H \rightarrow ZZ^* \rightarrow 4\ell$ decay with $m_H = 125$ GeV and $\ell = (e, \mu)$ using PROPHECY4F [102,103], which includes the complete NLO EW corrections, and the interference effects between identical final-state fermions. Due to the latter, the expected branching ratios of the $4e$ and 4μ final states are about 10% higher than the branching ratios to $2e2\mu$ and $2\mu2e$ final states. Table 2 summarises the predicted SM production cross-sections and branching ratios for the $H \rightarrow ZZ^* \rightarrow 4\ell$ decay for $m_H = 125$ GeV.

For the study of the tensor structure of Higgs boson couplings within an effective field theory approach, several samples with different values of EFT parameters were simulated at LO in QCD separately for the ggF + bbH , VBF + $V(\rightarrow qq)H$, $qq \rightarrow Z(\rightarrow \ell\ell)H$, $qq \rightarrow W(\rightarrow \ell\nu)H$, ttH , tHW and $tHjb$ production modes using MADGRAPH5_aMC@NLO and the NNPDF23lo PDF. The BSM signal is defined by the flavour symmetric SMEFT-SIM_A_U35_MWScheme_UFO_v2.1 model [29,106], which incorporates the SMEFT dimension-six operators in the standard Universal FeynRules Output format created using the FeynRules framework [107,108]. The light quarks (u, d, s and c) and leptons are assumed to be massless in the model. The generated events were showered with PYTHIA 8, using the CKKW-L matching scheme to match matrix element and parton shower computations with different jet multiplicities [61]. The A14 set of tuned parameters was used. All processes were simulated in the four-flavour scheme, apart from the tHW production, for which the five-flavour scheme was used [55].

The ZZ^* continuum background from quark–antiquark annihilation was modelled using SHERPA v2.2.2 [109–112], which provides a matrix element calculation accurate to NLO in α_S for 0-jet and 1-jet final states and LO accuracy for 2-jets and 3-jets final states. The merging with the SHERPA parton shower [113] was performed using the ME+PS@NLO prescription [114]. The NLO EW corrections were applied as a function of the invariant mass m_{ZZ^*} of the ZZ^* system [115, 116].

The gluon-induced ZZ^* production was modelled by SHERPA v2.2.2 [109–111] at LO in QCD for 0-jet and 1-jet final states. The higher-order QCD effects for the $gg \rightarrow ZZ^*$ continuum production cross-section were calculated for massless quark loops [117–119] in the heavy top-quark approximation [120], including the interference with $gg \rightarrow H^* \rightarrow ZZ$ processes [121, 122]. The $gg \rightarrow ZZ$ simulation was scaled by a K -factor of 1.7 ± 1.0 , which is defined as the ratio of the higher-order to the leading-order cross-section predictions.

Production of ZZ^* via vector-boson scattering was simulated with the SHERPA v2.2.2 [112] generator. The LO-accurate matrix elements were matched to a parton shower using the MEPS@LO prescription.

For all ZZ^* processes modelled using SHERPA, the NNPDF3.0nnlo PDF set [60] was used, along with a dedicated set of tuned parton-shower parameters.

For additional checks, the $q\bar{q}$ -initiated ZZ^* continuum background was also modelled using POWHEG-BOX v2 and MADGRAPH5_aMC@NLO, using the CT10 [57] and the PDF4LHC NLO PDF set, respectively. For the former, the matrix element was generated at NLO accuracy in QCD and effects of singly resonant amplitudes and interference effects due to Z/γ^* were included. For the latter, the simulations are accurate to NLO in QCD for zero and one additional parton merged with the FxFx merging scheme. For both, the PYTHIA 8 generator was used for the modelling of parton showering, hadronisation, and the underlying event. The AZNLO and A14 sets of tuned parameters were used for the simulations performed with POWHEG-BOX v2 and MADGRAPH5_aMC@NLO generators, respectively.

The WZ background [123] was modelled at NLO accuracy in QCD using POWHEG-BOX v2 with the CT10 PDF set and was interfaced to PYTHIA 8, using the AZNLO set of tuned parameters for modelling of parton showering, hadronisation, and the underlying event and to EVTGEN v1.2.0 for the simulation of bottom and charm hadron decays. The triboson backgrounds ZZZ , WZZ , and WWZ with four or more prompt leptons (VVV) were modelled at NLO accuracy for the inclusive process and at LO for up to two additional parton emissions using SHERPA v2.2.2.

The simulation of ttZ events with both top quarks decaying semileptonically and the Z boson decaying leptonically was performed with MADGRAPH5_aMC@NLO using

the NNPDF3.0nlo [60] PDF set interfaced to PYTHIA 8 using the A14 set of tuned parameters, and the total cross-section was normalised to a prediction computed at NLO in the QCD and EW couplings [98]. For modelling comparisons, SHERPA v2.2.1 was used to simulate ttZ events at LO. The tWZ , $ttWW$, $ttWZ$, $ttZ\gamma$, $ttZZ$, ttt , $tttt$ and tZ background processes were simulated with MADGRAPH5_aMC@NLO interfaced to PYTHIA 8, using the A14 set of tuned parameters. These processes are collectively referred to as the tXX process.

The modelling of events containing Z bosons with associated jets (Z +jets) was performed using the SHERPA v2.2.1 generator. Matrix elements were calculated for up to two partons at NLO and four partons at LO using COMIX [110] and OPENLOOPS [111], and merged with the SHERPA parton shower [113] using the ME+PS@NLO prescription [114]. The NNPDF3.0nnlo PDF set is used in conjunction with dedicated set of tuned parton-shower parameters.

The tt background was modelled using POWHEG-BOX v2 with the NNPDF3.0nlo PDF set. This simulation was interfaced to PYTHIA 8, using the A14 set of tuned parameters, for parton showering, hadronisation, and the underlying event, and to EVTGEN v1.2.0 for heavy-flavour hadron decays. Simulated Z +jets and tt background samples were normalised to the data-driven estimates described in Sect. 6.

Generated events were processed through the ATLAS detector simulation [124] within the GEANT4 framework [125] and reconstructed in the same way as collision data. Additional pp interactions in the same and nearby bunch crossings were included in the simulation. Pile-up events were generated using PYTHIA 8 with the A2 set of tuned parameters [126] and the MSTW2008LO PDF set [127]. The simulation samples were weighted to reproduce the distribution of the number of interactions per bunch crossing observed in data.

4 Event selection

4.1 Event reconstruction

The selection and categorisation of the Higgs boson candidate events rely on the reconstruction and identification of electrons, muons, and jets, closely following the analyses reported in Refs. [17, 128].

Proton–proton collision vertices are constructed from reconstructed trajectories of charged particles in the ID with transverse momentum $p_T > 500$ MeV. Events are required to have at least one collision vertex with at least two associated tracks. The vertex with the highest $\sum p_T^2$ of reconstructed tracks is selected as the primary vertex of the hard interaction. The data are subjected to quality requirements to reject

events in which detector components were not operating correctly.

Electron candidates are reconstructed from energy clusters in the electromagnetic calorimeter that are matched to ID tracks [129]. A Gaussian-sum filter algorithm [130] is used to compensate for radiative energy losses in the ID for the track reconstruction, while a dynamical, topological cell-based approach for cluster building is used to improve the energy resolution relative to the previous measurements in Refs. [17, 128], in particular for the case of bremsstrahlung photons. Electron identification is based on a likelihood discriminant combining the measured track properties, transition radiation response, electromagnetic shower shapes and the quality of the track–cluster matching. The ‘loose’ likelihood criteria, applied in combination with track hit requirements, provide an electron reconstruction and identification efficiency of at least 90% for isolated electrons with $p_T > 30$ GeV and 85%–90% below [129]. Electrons are required to have $E_T > 7$ GeV and pseudorapidity $|\eta| < 2.47$, with their energy calibrated as described in Ref. [129].

Muon candidate reconstruction [131] within the range $|\eta| < 2.5$ is primarily performed by a global fit to fully reconstructed tracks in the ID and the MS, with a ‘loose’ [131] identification criterion applied. This criterion has an efficiency of at least 98% for isolated muons with $p_T = 5$ GeV and rises to 99.5% at higher p_T . At the centre of the detector ($|\eta| < 0.1$), which has a reduced MS geometrical coverage, muons are also identified by matching a fully reconstructed ID track to either an MS track segment or a calorimeter energy deposit consistent with a minimum-ionising particle (calorimeter-tagged muons). For these two cases, the muon momentum is measured from the ID track alone. In the forward MS region ($2.5 < |\eta| < 2.7$), outside the full ID coverage, MS tracks with hits in the three MS layers are accepted and combined with forward ID tracklets, if they exist (stand-alone muons). Calorimeter-tagged muons are required to have $p_T > 15$ GeV. For all other muon candidates, the transverse momentum is required to be greater than 5 GeV. The muon momentum is calibrated using the procedure described in Ref. [131]. Muons with transverse impact parameter greater than 1 mm are rejected.² Additionally, muons and electrons are required to have a longitudinal impact parameter ($|z_0 \sin \theta|$) less than 0.5 mm.

Jets are reconstructed using a particle flow algorithm [22] from noise-suppressed positive-energy topological clusters [132] in the calorimeter using the anti- k_t algorithm [26, 27] with a radius parameter $R = 0.4$. Energy deposited in the

calorimeter by charged particles is subtracted and replaced by the momenta of tracks that are matched to those topological clusters. Compared to only using topological clusters, jets reconstructed with the particle flow algorithm with $p_T > 30$ GeV have approximately 10% better transverse momentum resolution. The two different algorithms have similar resolution for p_T above 100 GeV. The jet four-momentum is corrected for the calorimeter’s non-compensating response, signal losses due to noise threshold effects, energy lost in non-instrumented regions, and contributions from pile-up [22, 133, 134]. Jets are required to have $p_T > 30$ GeV and $|\eta| < 4.5$. Jets from pile-up with $|\eta| < 2.5$ are suppressed using a jet-vertex-tagger multivariate discriminant [135, 136]. Jets with $|\eta| < 2.5$ containing b -hadrons are identified using the MV2c10 b -tagging algorithm [137, 138], and its 60%, 70%, 77% and 85% efficiency working points are combined into a pseudo-continuous b -tagging weight [139] that is assigned to each jet.

Ambiguities are resolved if electron, muon, or jet candidates overlap in geometry or share the same detector information. If the two calorimeter energy clusters from the two electron candidates overlap, the electron with the higher E_T is retained. If a reconstructed electron and muon share the same ID track, the muon is rejected if it is calorimeter-tagged; otherwise the electron is rejected. Reconstructed jets geometrically overlapping in a cone of radial size $\Delta R = 0.1$ (0.2) with a muon (an electron) are also removed.

The missing transverse momentum vector, \vec{E}_T^{miss} , is defined as the negative vector sum of the transverse momenta of all the identified and calibrated leptons, photons and jets and the remaining unclustered energy, where the latter is estimated from low- p_T tracks associated with the primary vertex but not assigned to any lepton, photon, hadronically decaying τ -lepton or jet candidate [140, 141]. The missing transverse momentum (E_T^{miss}) is defined as the magnitude of \vec{E}_T^{miss} .

4.2 Selection of the Higgs boson candidates

A summary of the event selection criteria is given in Table 3. Events were triggered by a combination of single-lepton, dilepton and trilepton triggers with different transverse momentum thresholds. Single-lepton triggers with the lowest thresholds had strict identification and isolation requirements. Both the high-threshold single-lepton triggers and the multilepton triggers had looser selection criteria. Due to an increasing peak luminosity, these thresholds increased slightly during the data-taking periods [142, 143]. For single-muon triggers, the p_T threshold ranged from between 20 and 26 GeV, while for single-electron triggers, the p_T threshold ranged from 24 to 26 GeV. The global trigger efficiency for signal events passing the final selection is about 98%.

In the analysis, at least two same-flavour and opposite-charge lepton pairs (hereafter referred to as lepton pairs) are

² The transverse impact parameter d_0 of a charged-particle track is defined in the transverse plane as the distance from the primary vertex to the track’s point of closest approach. The longitudinal impact parameter z_0 is the distance in the z direction between this track point and the primary vertex.

Table 3 Summary of the criteria applied to the selected Higgs boson candidate in each event. The mass threshold m_{\min} is defined in Sect. 4.1

TRIGGER	
Combination of single-lepton, dilepton and trilepton triggers	
LEPTONS AND JETS	
ELECTRONS	$E_T > 7 \text{ GeV}$ and $ \eta < 2.47$
MUONS	$p_T > 5 \text{ GeV}$ and $ \eta < 2.7$, calorimeter-tagged: $p_T > 15 \text{ GeV}$
JETS	$p_T > 30 \text{ GeV}$ and $ \eta < 4.5$
QUADRUPLETS	
All combinations of two same-flavour and opposite-charge lepton pairs	
– Leading lepton pair: lepton pair with invariant mass m_{12} closest to the Z boson mass m_Z	
– Subleading lepton pair: lepton pair with invariant mass m_{34} second closest to the Z boson mass m_Z	
Classification according to the decay final state: $4\mu, 2e2\mu, 2\mu2e, 4e$	
REQUIREMENTS ON EACH QUADRUPLET	
LEPTON RECONSTRUCTION	– Three highest- p_T leptons must have p_T greater than 20, 15 and 10 GeV
LEPTON PAIRS	– At most one calorimeter-tagged or stand-alone muon
	– Leading lepton pair: $50 < m_{12} < 106 \text{ GeV}$
	– Subleading lepton pair: $m_{\min} < m_{34} < 115 \text{ GeV}$
	– Alternative same-flavour opposite-charge lepton pair: $m_{\ell\ell} > 5 \text{ GeV}$
	– $\Delta R(\ell, \ell') > 0.10$ for all lepton pairs
LEPTON ISOLATION	– The amount of isolation E_T after summing the track-based and 40% of the calorimeter-based contribution must be smaller than 16% of the lepton p_T
IMPACT PARAMETER SIGNIFICANCE	– Electrons: $ d_0 /\sigma(d_0) < 5$
	– Muons: $ d_0 /\sigma(d_0) < 3$
COMMON VERTEX	– χ^2 -requirement on the fit of the four lepton tracks to their common vertex
SELECTION OF THE BEST QUADRUPLET	
– Select quadruplet with m_{12} closest to m_Z from one decay final state in decreasing order of priority: $4\mu, 2e2\mu, 2\mu2e$ and $4e$	
– If at least one additional (fifth) lepton with $p_T > 12 \text{ GeV}$ meets the isolation, impact parameter and angular separation criteria, select the quadruplet with the highest matrix-element value	
HIGGS BOSON MASS WINDOW	
– Correction of the four-lepton invariant mass due to the FSR photons in Z boson decays	
– Four-lepton invariant mass window in the signal region: $115 < m_{4\ell} < 130 \text{ GeV}$	
– Four-lepton invariant mass window in the sideband region: $105 < m_{4\ell} < 115 \text{ GeV}$ or $130 < m_{4\ell} < 160 (350) \text{ GeV}$	

required in the final state, resulting in one or more possible lepton quadruplets in each event. The three highest- p_T leptons in each quadruplet are required to have transverse momenta above 20 GeV, 15 GeV and 10 GeV, respectively. To minimise the background contribution from non-prompt muons, at most one calorimeter-tagged or stand-alone muon is allowed per quadruplet.

The lepton pair with the invariant mass m_{12} (m_{34}) closest (second closest) to the Z boson mass [144] in each quadruplet is referred to as the leading (subleading) lepton pair. Based on the lepton flavour, each quadruplet is classified into one of the following decay final states: $4\mu, 2e2\mu, 2\mu2e$ and $4e$, with the first two leptons always representing the leading lepton

pair. In each of these final states, the quadruplet with m_{12} closest to the Z boson mass has priority to be considered for the selection of the final Higgs boson candidate. In case additional prompt leptons are present in the event, the priority may change due to the matrix-element based pairing as described later on. All quadruplets are therefore required to pass the following selection criteria.

To ensure that the leading lepton pair from the signal originates from a Z boson decay, the leading lepton pair is required to satisfy $50 \text{ GeV} < m_{12} < 106 \text{ GeV}$. The subleading lepton pair is required to have a mass $m_{\min} < m_{34} < 115 \text{ GeV}$, where m_{\min} is 12 GeV for the four-lepton invariant mass $m_{4\ell}$ below 140 GeV, rising linearly to 50 GeV at $m_{4\ell} = 190 \text{ GeV}$

and then remaining at 50 GeV for all higher $m_{4\ell}$ values. This criterion suppresses the contributions from processes in which an on-shell Z boson is produced in association with a leptonically decaying meson or virtual photon. In the $4e$ and 4μ final states, the two alternative opposite-charge lepton pairings within a quadruplet are required to have a dilepton mass above 5 GeV to suppress the J/ψ background. All leptons in the quadruplet are required to have an angular separation of $\Delta R > 0.1$.

Each electron (muon) track is required to have a transverse impact parameter significance $|d_0/\sigma(d_0)| < 5$ (3), to suppress the background from heavy-flavour hadrons. Reducible background from the Z +jets and tt processes is further suppressed by imposing track-based and calorimeter-based isolation criteria on each lepton [131, 145]. A scalar p_T sum (track isolation) is made from the tracks with $p_T > 500$ MeV which either originate from the primary vertex or have $|z_0 \sin \theta| < 3$ mm if not associated with any vertex and lie within a cone of $\Delta R = 0.3$ around the muon or electron. Above a lepton p_T of 33 GeV, this cone size falls linearly with p_T to a minimum cone size of 0.2 at 50 GeV. Similarly, the scalar E_T sum (calorimeter isolation) is calculated from the positive-energy topological clusters that are not associated with a lepton track in a cone of $\Delta R = 0.2$ around the muon or electron. The sum of the track isolation and 40% of the calorimeter isolation is required to be less than 16% of the lepton p_T . The calorimeter isolation is corrected for electron shower leakage, pile-up and underlying-event contributions. Both isolations are corrected for track and topological cluster contributions from the remaining three leptons. The pile-up dependence of this isolation selection is improved compared with that of the previous measurements [17, 128, 146] by optimising the criteria used for exclusion of tracks associated with a vertex other than the primary vertex and by the removal of topological clusters associated with tracks. The signal efficiency of the isolation criteria is greater than 80%, improving the efficiency by about 5% compared with the previous analysis for the same background rejection.

The four quadruplet leptons are required to originate from a common vertex point. A requirement corresponding to a signal efficiency of better than 99.5% is imposed on the χ^2 value from the fit of the four lepton tracks to their common vertex.

If there is more than one decay final state per event with the priority quadruplet (m_{12} closest to m_Z) satisfying the selection criteria, the quadruplet from the final state with highest selection efficiency, i.e. ordered 4μ , $2e2\mu$, $2\mu2e$ and $4e$, is chosen as the Higgs boson candidate.

In the case of VH or ttH production, there may be additional prompt leptons present in the event, together with the selected quadruplet. Therefore, there is a possibility that one or more of the leptons selected in the quadruplet do not originate from a Higgs boson decay, but rather from

the V boson leptonic decay or the top quark semileptonic decay. To improve the lepton pairing in such cases, a matrix-element-based pairing method assuming the SM tensor structure is used for all events containing at least one additional lepton with $p_T > 12$ GeV and satisfying the same identification, isolation and angular separation criteria as the four quadruplet leptons [17, 128]. For all possible quadruplet combinations that satisfy the selection, a matrix element for the Higgs boson decay is computed at LO using the MADGRAPH5_aMC@NLO [55] generator, with the reconstructed lepton momentum vectors as inputs to the calculation. The quadruplet with the largest matrix-element value is selected as the Higgs boson candidate. This method leads to a 50% improvement in correctly identifying the leptons in the quadruplet as those originating from a Higgs boson decay if an extra lepton is identified. The impact of the matrix element on the expected invariant mass distribution is shown in Fig. 2a.

To improve the four-lepton invariant mass reconstruction, the reconstructed final-state radiation (FSR) photons in Z boson decays are accounted for using the same strategy as the previous publications [17, 128]. Collinear FSR candidates are defined as candidates with $\Delta R < 0.15$ to the nearest lepton in the quadruplet. Collinear FSR candidates are considered only for muons from the leading lepton pair, while non-collinear FSR candidates are considered for both muons and electrons from leading and subleading Z bosons.

Collinear FSR candidates are selected from reconstructed photon candidates and from electron candidates that share an ID track with the muon. Further criteria are applied to each candidate, based on the following discriminants: the fraction, f_1 , of cluster energy in the front segment of the EM calorimeter divided by the total cluster energy to reduce backgrounds from muon ionisation; the angular distance, $\Delta R_{\text{cluster},\mu}$, between the candidate EM cluster and the muon; and the candidate p_T , which must be at least 1 GeV. For all selected electron candidates and for photon candidates with $p_T < 3.5$ GeV, a requirement of $f_1 > 0.2$ and $\Delta R_{\text{cluster},\mu} < 0.08$ is imposed. The collinear photon candidates with $p_T > 3.5$ GeV are selected if $f_1 > 0.1$ and $\Delta R_{\text{cluster},\mu} < 0.15$. Non-collinear FSR candidates are selected only from reconstructed isolated photons meeting the ‘tight’ criteria [129, 147] and satisfying $p_T > 10$ GeV and $\Delta R_{\text{cluster},\ell} > 0.15$.

Only one FSR candidate is included in the quadruplet, with preference given to collinear FSR and to the candidate with the highest p_T . An FSR candidate is added to the lepton pair if the invariant mass of the lepton pair is between 66 and 89 GeV and if the invariant mass of the lepton pair and the photon is below 100 GeV. Approximately 3% of reconstructed Higgs boson candidates have an FSR candidate and its impact on the expected invariant mass distribution is shown in Fig. 2b.

The Higgs boson candidates within a mass window of $115 \text{ GeV} < m_{4\ell} < 130 \text{ GeV}$ are selected as the signal region. Events failing this requirement but that are within a mass window of $105 \text{ GeV} < m_{4\ell} < 115 \text{ GeV}$ or $130 \text{ GeV} < m_{4\ell} < 160$ (350) GeV are assigned to the sideband regions used to estimate the leading backgrounds as described in Sect. 6.

The selection efficiencies of the simulated signal in the fiducial region $|y_H| < 2.5$, where y_H is the Higgs boson rapidity, are about 33%, 25%, 19% and 16%, in the 4μ , $2e2\mu$, $2\mu2e$ and $4e$ final states, respectively.

5 Event categorisation and production mode discrimination

In order to be sensitive to different production bins in the framework of simplified template cross-sections, the selected Higgs boson candidates in the mass window $115 \text{ GeV} < m_{4\ell} < 130 \text{ GeV}$ are classified into several dedicated reconstructed event categories. In addition, the events in the mass sidebands are also categorised for purposes of background estimation described in Sect. 6. In general, more than one production mode contributes to each reconstructed event category, as well as various background processes. For this reason, multivariate discriminants are introduced in most of the mutually exclusive reconstructed event categories to distinguish between these contributions.

5.1 Event categorisation

For signal events, the classification is performed in the order shown in the middle-right panel of Fig. 1 (from bottom to top) and as described below. First, those events classified as enriched in the ttH process are split according to the decay mode of the two W bosons from the top quark decays. For semileptonic and dileptonic decays (ttH -Lep-enriched), at least one additional lepton with $p_T > 12 \text{ GeV}$ ³ together with at least two b -tagged jets (with 85% b -tagging efficiency), or at least five jets among which at least one b -tagged jet (with 85% b -tagging efficiency) or at least two jets among which at least one b -tagged jet (with 60% b -tagging efficiency) is required. For the fully hadronic decay (ttH -Had-enriched), there must be either at least five jets among which at least two b -tagged jets (with 85% b -tagging efficiency) or at least four jets among which at least one b -tagged jet (with 60% b -tagging efficiency). Events with additional leptons but not satisfying the jet requirements define the next category enriched in VH production events with leptonic vector-boson decay (VH -Lep-enriched).

The remaining events are classified according to their reconstructed jet multiplicity into events with no jets, exactly one jet or at least two jets. Events with at least two reconstructed jets are divided into two categories: one is a ‘BSM-like’ category ($2j$ -BSM-like) and the other ($2j$) contains the bulk of events with significant contributions from the VBF and VH production modes in addition to ggF. The $2j$ -BSM-like category requires the invariant mass m_{jj} of the two leading jets to be larger than 120 GeV and the four-lepton transverse momentum, $p_T^{4\ell}$, to be larger than 200 GeV; the remaining events are placed in the $2j$ category.

Events with zero or one jet in the final state are expected to be mostly from the ggF process. Following the particle-level definition of production bins in Sect. 1.1, the 1-jet category is further split into four categories with $p_T^{4\ell}$ smaller than 60 GeV ($1j$ - $p_T^{4\ell}$ -Low), between 60 and 120 GeV ($1j$ - $p_T^{4\ell}$ -Med), between 120 and 200 GeV ($1j$ - $p_T^{4\ell}$ -High), and larger than 200 GeV ($1j$ - $p_T^{4\ell}$ -BSM-like).

The largest number of ggF events and the highest ggF purity are expected in the zero-jet category. The zero-jet category is split into three categories with $p_T^{4\ell}$ smaller than 10 GeV ($0j$ - $p_T^{4\ell}$ -Low), between 10 and 100 GeV ($0j$ - $p_T^{4\ell}$ -Med) and above 100 GeV ($0j$ - $p_T^{4\ell}$ -High). The first two categories follow the production bin splitting, and the last category improves the discrimination between VH ($V \rightarrow \ell\nu/\nu\nu$) and ggF.

As illustrated in Fig. 1, there is a dedicated reconstructed event category for each production bin except for gg2H- $2j$, qq2Hqq- VH and qq2Hqq-VBF. These production bins are largely measured from the 2-jet reconstruction category, and to a lesser extent from the 1-jet categories, using multivariate discriminants (see Sect. 5.2). The gg2H- p_T^H -High production bin is measured simultaneously in all reconstructed event categories with high transverse momentum of the four-lepton system, independent of the reconstructed jet multiplicity.

The rightmost panel of Fig. 1 shows the background event classification. For estimating the tXX process from the mass sideband, a tXX -enriched sideband category (SB- tXX -enriched) is defined, which includes events with at least two jets including at least one tagged as a b -jet with 60% efficiency and $E_T^{\text{miss}} > 100 \text{ GeV}$ in the $m_{4\ell}$ mass range 105–115 GeV or 130–350 GeV. This region is dominated by ttZ (87%) and has small contributions from tt , $tttt$, tWZ , ttW , $ttWW$, $ttWZ$, $ttZ\gamma$, $ttZZ$ and tZ . The tXX process is expected to give the largest contribution in ‘ ttH -like’ categories. The large mass range for this category, larger than for the non-resonant ZZ as discussed next, allows better statistical precision for the estimate of this background.

For the estimation of non-resonant ZZ^* production, events not meeting the criteria for the SB- tXX -enriched category and in the $m_{4\ell}$ mass range 105–115 GeV or 130–160 GeV are split according to the number of reconstructed jets: exactly zero jets (SB- $0j$), exactly one jet (SB- $1j$) or at

³ The additional lepton is a lepton candidate as defined in Sect. 4.1. It is also required to satisfy the same isolation, impact parameter and angular separation requirements as the leptons in the quadruplet.

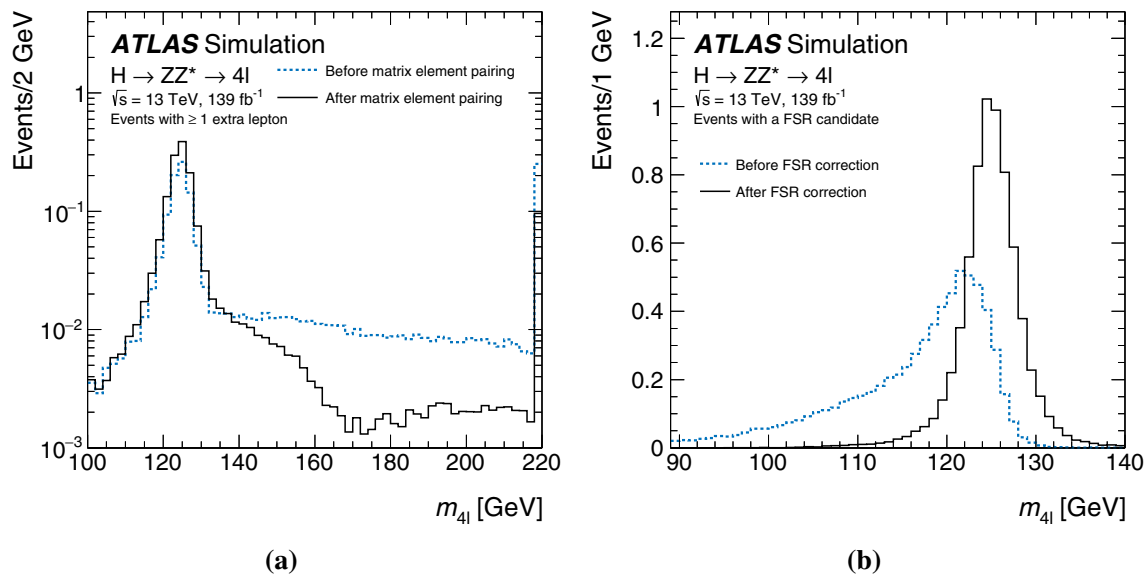


Fig. 2 Impact on the expected invariant mass distribution of the selected Higgs boson candidates due to (a) matrix-element-based pairing for candidates with at least one extra lepton and (b) accounting for

final-state radiation for candidates with an FSR candidate. For (a), the overflow events are included in the last bin

least two jets (SB-2 j). This mass range limits the contribution from the single-resonance process, $Z \rightarrow 4\ell$, and from the on-shell ZZ process. Similarly, events in the same mass range with an extra reconstructed lepton separately form the SB- VH -Lep-enriched category, which is enriched with signal events containing leptons from the associated V leptonic decay or the top quark semileptonic decay. This category is mainly designed to improve the expected sensitivity for VH -Lep by about 5%, having a VH purity of about 19%.

The expected number of signal events is shown in Table 4 for each reconstructed event category separately for each production mode. The ggF and bbH contributions are shown separately to compare their relative contributions, but both belong in the same (ggF) production bin. The highest bbH event yield is expected in the $0j$ categories since the jets tend to be more forward than in the ttH process, thus escaping the acceptance of the ttH selection criteria. The sources of uncertainty in these expectations are detailed in Sect. 7. The signal composition in terms of the Reduced Stage-1.1 production bins is shown in Fig. 3.

The separation of the contributions from different production bins, such as the gg2H-2 j , qq2Hqq- VH and qq2Hqq-VBF components contributing in categories with two or more jets, is improved by means of discriminants obtained using multivariate data analysis, as described in the following section.

5.2 Multivariate production mode discriminants

To further increase the sensitivity of the cross-section measurements in the production bins (Sect. 1.1), multivariate

discriminants using neural networks (NNs) [148] are introduced in many of the reconstructed signal event categories as observables used in the statistical fit, described in Sect. 8.2. The NN architecture and training procedure are defined using Keras with TensorFlow [149, 150]. These networks are trained using several discriminating observables, as defined in Table 5, on simulated SM Higgs boson signals with $m_H = 125$ GeV or non-Higgs-boson background. Due to the low number of signal events expected in the $0j$ - $p_T^{4\ell}$ -High, $1j$ - $p_T^{4\ell}$ -BSM-like and ttH -Lep-enriched categories, only the observed yield is used as the discriminant in these categories.

Two types of NNs are used: feed-forward multilayer perceptron (MLP) and recurrent (RNN) [148–152]. Each NN discriminant combines two RNNs, one for the p_T -ordered variables related to the four leptons in the quadruplet and one for variables related to jets, and an MLP with additional variables related to the full event. The jet RNN accepts inputs from up to three jets. The outputs of the MLP and the two RNNs are chained into another MLP to complete an NN discriminant, which is trained to approximate the posterior probability for an event to originate from a given process. This is used in each reconstructed event category to discriminate between two or three processes, e.g. ggF, VBF and ZZ background in the $1j$ - $p_T^{4\ell}$ -Low category. The variables used to train the MLP and RNNs for each category along with the processes being separated are summarised in Table 5.

The NN training variables not previously defined are listed as follows. The kinematic discriminant D_{ZZ^*} [153], defined as the difference between the logarithms of the squared matrix elements for the signal decay (same as in Sect. 4) and squared matrix elements for the background process, is used

Table 4 The expected number of SM Higgs boson events with $m_H = 125$ GeV for an integrated luminosity of 139 fb^{-1} at $\sqrt{s} = 13$ TeV in each reconstructed event signal ($115 < m_{4\ell} < 130$ GeV) and sideband ($m_{4\ell}$ in $105\text{--}115$ GeV or $130\text{--}160$ GeV for ZZ^* , $130\text{--}350$ GeV for $\tau\tau$) category, shown separately for each production bin of the Production Mode Stage. The ggF and bbH yields are shown separately but both contribute to the same (ggF) production bin, and ZH and WH are reported separately but are merged together for the final result. Statistical and systematic uncertainties, including those for total SM cross-section predictions, are added in quadrature. Contributions that are below 0.2% of the total signal in each reconstructed event category are not shown and are replaced by ‘—’,

Reconstructed event category	SM Higgs boson production mode					
	ggF	VBF	WH	ZH	$t\bar{t}H + \tau H$	bbH
Signal	115 < $m_{4\ell}$ < 130 GeV					
$0j\text{-}p_T^{4\ell}\text{-Low}$	23.9 ± 3.5	0.073 ± 0.006	0.0173 ± 0.0031	0.0131 ± 0.0023	—	0.17 ± 0.09
$0j\text{-}p_T^{4\ell}\text{-Med}$	74 ± 8	1.03 ± 0.15	0.37 ± 0.05	0.40 ± 0.05	—	0.8 ± 0.4
$0j\text{-}p_T^{4\ell}\text{-High}$	0.109 ± 0.026	0.0157 ± 0.0024	0.056 ± 0.005	0.173 ± 0.016	0.00065 ± 0.00023	—
$1j\text{-}p_T^{4\ell}\text{-Low}$	31 ± 4	1.99 ± 0.11	0.52 ± 0.05	0.35 ± 0.04	—	0.41 ± 0.21
$1j\text{-}p_T^{4\ell}\text{-Med}$	17.3 ± 2.8	2.50 ± 0.18	0.52 ± 0.06	0.40 ± 0.04	0.0078 ± 0.0013	0.09 ± 0.04
$1j\text{-}p_T^{4\ell}\text{-High}$	3.6 ± 0.8	0.84 ± 0.07	0.158 ± 0.015	0.166 ± 0.016	0.0044 ± 0.0006	0.011 ± 0.006
$1j\text{-}p_T^{4\ell}\text{-BSM-like}$	0.87 ± 0.23	0.246 ± 0.020	0.060 ± 0.007	0.054 ± 0.006	0.00156 ± 0.00032	0.0009 ± 0.0005
$2j$	25 ± 5	8.5 ± 0.6	1.94 ± 0.15	1.69 ± 0.13	0.46 ± 0.04	0.30 ± 0.15
$2j\text{-BSM-like}$	1.9 ± 0.6	1.08 ± 0.05	0.120 ± 0.016	0.122 ± 0.016	0.075 ± 0.007	0.0021 ± 0.0010
$VH\text{-Lep-enriched}$	0.050 ± 0.011	0.019 ± 0.004	0.80 ± 0.07	0.245 ± 0.021	0.166 ± 0.013	0.0027 ± 0.0014
$t\bar{t}H\text{-Had-enriched}$	0.15 ± 0.16	0.021 ± 0.004	0.020 ± 0.005	0.055 ± 0.013	0.75 ± 0.07	0.020 ± 0.011
$t\bar{t}H\text{-Lep-enriched}$	0.0019 ± 0.0022	0.00019 ± 0.00008	0.0046 ± 0.0026	0.0032 ± 0.0018	0.41 ± 0.04	—
Sideband	105 < $m_{4\ell}$ < 115 GeV or 130 < $m_{4\ell}$ < 160 GeV					
SB-0j	4.2 ± 0.5	0.050 ± 0.010	0.096 ± 0.011	0.042 ± 0.005	—	0.044 ± 0.022
SB-1j	2.37 ± 0.29	0.241 ± 0.024	0.100 ± 0.013	0.063 ± 0.008	0.0049 ± 0.0009	0.023 ± 0.012
SB-2j	1.25 ± 0.26	0.43 ± 0.05	0.119 ± 0.014	0.103 ± 0.012	0.109 ± 0.010	0.016 ± 0.008
SB-VH-Lep-enriched	0.015 ± 0.005	0.0029 ± 0.0011	0.084 ± 0.008	0.104 ± 0.010	0.065 ± 0.006	0.0013 ± 0.0007
SB-rXX-enriched	0.001 ± 0.010	0.00012 ± 0.00009	0.0006 ± 0.0004	0.0008 ± 0.0004	0.068 ± 0.008	—
Total	186 ± 14	17.0 ± 0.8	5.0 ± 0.4	3.97 ± 0.29	2.13 ± 0.18	1.9 ± 1.0

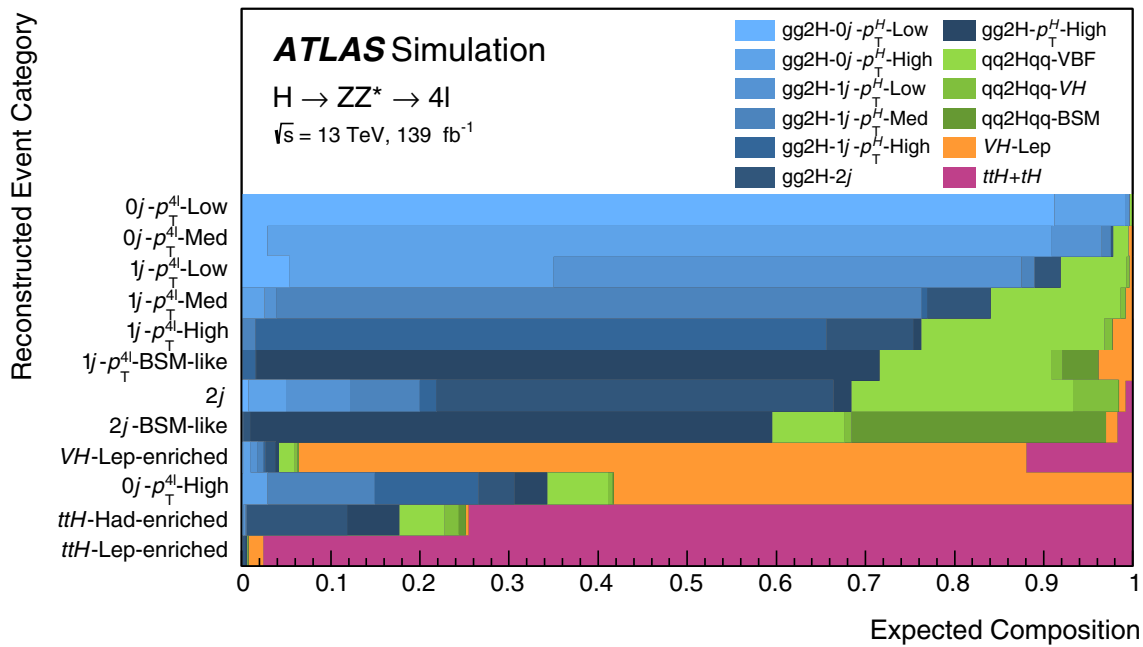


Fig. 3 Standard Model signal composition in terms of the Reduced Stage-1.1 production bins in each reconstructed event category. The bbH contributions are included in the ggF production bins

Table 5 The input variables used to train the MLP, and the two RNNs for the four leptons and the jets (up to three). For each category, the processes which are classified by an NN, their corresponding input variables and the observable used are shown. For example, there are

eight input variables for the Lepton RNN being trained if p_T^ℓ and η_ℓ are listed. Leptons and jets are denoted by ‘ ℓ ’ and ‘ j ’. See the text for the definitions of the variables

Category	Processes	MLP	Lepton RNN	Jet RNN	Discriminant
0j- $p_T^{4\ell}$ -Low 0j- $p_T^{4\ell}$ -Med	ggF, ZZ*	$p_T^{4\ell}, D_{ZZ^*}, m_{12}, m_{34}, \cos \theta^* , \cos \theta_1, \phi_{ZZ}$	p_T^ℓ, η_ℓ	–	NN _{ggF}
1j- $p_T^{4\ell}$ -Low	ggF, VBF, ZZ*	$p_T^{4\ell}, p_T^j, \eta_j, \Delta R_{4\ell j}, D_{ZZ^*}$	p_T^ℓ, η_ℓ	–	NN _{VBF} for NN _{ZZ} < 0.25 NN _{ZZ} for NN _{ZZ} > 0.25
1j- $p_T^{4\ell}$ -Med	ggF, VBF, ZZ*	$p_T^{4\ell}, p_T^j, \eta_j, E_T^{\text{miss}}, \Delta R_{4\ell j}, D_{ZZ^*}, \eta_{4\ell}$	p_T^ℓ, η_ℓ	–	NN _{VBF} for NN _{ZZ} < 0.25 NN _{ZZ} for NN _{ZZ} > 0.25
1j- $p_T^{4\ell}$ -High	ggF, VBF	$p_T^{4\ell}, p_T^j, \eta_j, E_T^{\text{miss}}, \Delta R_{4\ell j}, \eta_{4\ell}$	p_T^ℓ, η_ℓ	–	NN _{VBF}
2j	ggF, VBF, VH	$m_{jj}, p_T^{4\ell jj}$	p_T^ℓ, η_ℓ	p_T^j, η_j	NN _{VBF} for NN _{VH} < 0.2 NN _{VH} for NN _{VH} > 0.2
2j-BSM-like	ggF, VBF	$\eta_{ZZ}^{\text{Zepp}}, p_T^{4\ell jj}$	p_T^ℓ, η_ℓ	p_T^j, η_j	NN _{VBF}
VH-Lep-enriched	VH, ttH	$N_{\text{jets}}, N_{b\text{-jets},70\%}, E_T^{\text{miss}}, H_T$	p_T^ℓ	–	NN _{ttH}
ttH-Had-enriched	ggF, ttH, tXX	$p_T^{4\ell}, m_{jj}, \Delta R_{4\ell j}, N_{b\text{-jets},70\%},$	p_T^ℓ, η_ℓ	p_T^j, η_j	NN _{ttH} for NN _{tXX} < 0.4 NN _{tXX} for NN _{tXX} > 0.4

to distinguish ggF from the non-resonant ZZ background. Three angles [7] are used to further distinguish these processes: the cosine of the leading Z boson’s production angle θ^* in the four-lepton rest frame; the cosine of θ_1 defined as the

angle between the negatively charged lepton of the leading Z in the leading Z rest frame and the direction of flight of the leading Z in the four-lepton rest frame; and the angle ϕ_{ZZ} , between the two Z decay planes in the four-lepton rest frame.

The angular separation of the leading jet from the 4ℓ system, $\Delta R_{4\ell j}$, is used to distinguish VBF or ttH from ggF. For categories with two or more jets, kinematic variables that also include the information from the two leading jets are used: the invariant mass, m_{jj} ; the transverse momentum of the 4ℓ and the 2-jet system, $p_T^{4\ell jj}$; and the Zeppenfeld variable, $\eta_{ZZ}^{\text{Zepp}} = \left| \eta_{4\ell} - \frac{\eta_{j1} + \eta_{j2}}{2} \right|$ [154]. The number of reconstructed jets, N_{jets} , the number of b -tagged jets at 70% tagging efficiency, $N_{b\text{-jets},70\%}$, and the scalar sum of the p_T of all reconstructed jets, H_T , are used to identify the ttH process.

Depending on the category and the number of processes being targeted, the NN has two or three output nodes. The value computed at each node represents the probability, with an integral of one, for the event to originate from the given process. For example, for the 0-jet category, two probabilities are evaluated, NN_{ggF} and NN_{ZZ} . As these two values are a linear transformation of each other, only one output, NN_{ggF} , is used as a discriminant in the fit model. In categories with three targeted processes, only two of the three corresponding output probabilities are independent. In a given category, a selection is applied on one of the three output probabilities to split the events in two subcategories. This output probability is then used as the discriminant for the subcategory of events passing the selection, while for the other subcategory one of the two remaining output probabilities is used. The selection criterion is chosen so as to provide the largest purity of the targeted process for events passing the selection. For example, in the 1-jet category, NN_{VBF} and NN_{ZZ} are used. The subcategory of events with NN_{ZZ} larger than 0.25 uses NN_{ZZ} as the discriminant in the fit model, while NN_{VBF} is used in the remaining subcategory. The subcategory definitions and observables used in all reconstructed event categories are summarised in Table 5.

6 Background contributions

6.1 Background processes with prompt leptons

Non-resonant SM ZZ^* production via qq annihilation, gluon–gluon fusion and vector-boson scattering can result in four prompt leptons in the final state and constitutes the largest background for the analysis. While for the previous analyses [17, 128], simulation was exclusively used to estimate both the shape and normalisation, in this analysis the normalisation is constrained by a data-driven technique. This allows the systematic uncertainty to be reduced by removing both the theoretical and luminosity uncertainties contributing to the normalisation uncertainty.

As outlined in Sect. 5.1, to estimate the normalisation, sideband categories in the $m_{4\ell}$ mass region 105–115 GeV and 130–160 GeV are defined according to the jet multiplicity

(SB-0j, SB-1j, SB-2j). The normalisation of the ZZ^* background is simultaneously fitted with a common normalisation factor for signal region and sideband categories with the same jet multiplicity. For example, the ZZ^* background is scaled by a common factor for 2j, 2j-BSM-like and SB-2j categories. The background shape templates for NN discriminants and the expected fraction of events in relevant reconstructed signal-region event categories are obtained from simulation. As shown in Fig. 4a, good agreement is found between data and simulation for the shape of the NN observable. All expected distributions are shown after the final fit to the data for the Production Mode measurement (see Sect. 8) and are referred to as post-fit distributions in the following. The simulated distributions of the observables $p_T^{4\ell}$ and m_{jj} employed for the prediction of event fractions in each event category also agree with data, as seen in Figs. 4b, c respectively. The estimation of the ZZ^* process in the jet multiplicity bins removes one of the leading theoretical uncertainties [155]. Due to the limited sensitivity and the low expected yield, the normalisation of ZZ^* in ttH -like categories is estimated from simulation.

Similarly, backgrounds affecting the ttH -like categories are estimated simultaneously from an enriched sample selected in a dedicated sideband region (SB- tXX -enriched), with the mass cut extended up to 350 GeV to improve the statistical precision of the estimate. The normalisation of the tXX process is simultaneously fitted across the ttH -Lep-enriched, ttH -Had-enriched and SB- tXX -enriched categories. The N_{jets} observable distribution, which is used to predict the event fractions in each category, is shown in Fig. 4d and agrees with data. In all other categories, the sensitivity of the tXX measurement is limited due to a small number of expected tXX events and its normalisation is estimated from simulation.

The contribution from VVV processes is estimated for all categories using the simulated samples presented in Sect. 3.

6.2 Background processes with non-prompt leptons

Other processes, such as $Z + \text{jets}$, tt , and WZ , containing at least one jet, photon or lepton from a hadron decay that is misidentified as a prompt lepton, also contribute to the background. These ‘reducible’ backgrounds are significantly smaller than the non-resonant ZZ^* background and are estimated from data using different approaches for the $\ell\ell + \mu\mu$ and $\ell\ell + ee$ final states [17, 128].

In the $\ell\ell + \mu\mu$ final states, the normalisation of the $Z + \text{jets}$ and tt backgrounds are determined by performing fits to the invariant mass of the leading lepton pair in dedicated independent control regions. The shape of the invariant mass distribution for each region is parameterised using simulated samples. In contrast to the previous analyses [17, 128], this fit is performed independently for each reconstructed event

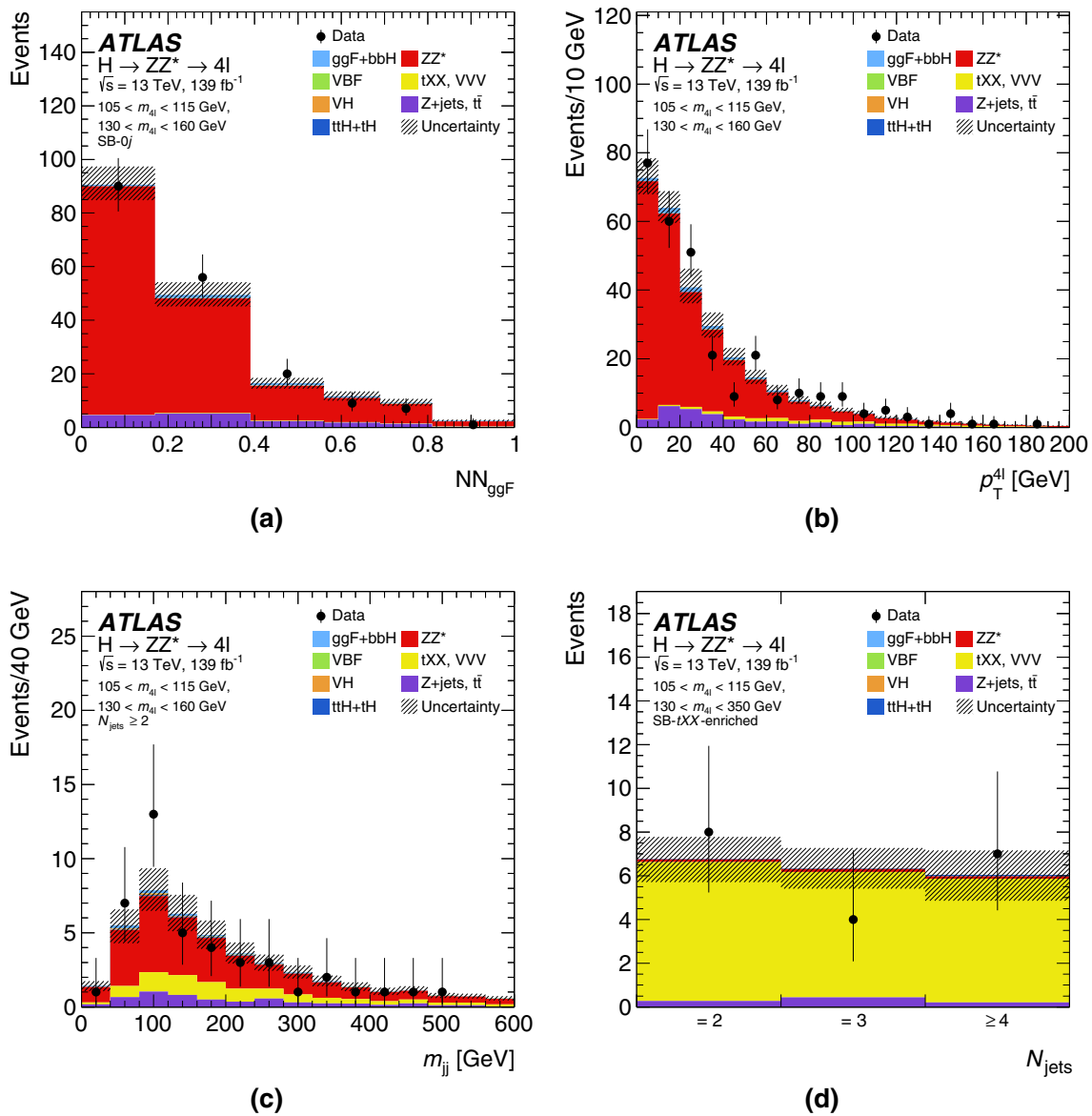


Fig. 4 The observed and expected (post-fit) distributions for an integrated luminosity of 139 fb^{-1} at $\sqrt{s} = 13 \text{ TeV}$ in the different background enriched regions: (a) NN_{ggF} in the SB-0j sideband region, (b) $p_T^{4\ell}$ in the sideband region combining the SB-0j, SB-1j and SB-2j categories, (c) m_{jj} in the SB-2j category, and (d) N_{jets} in the SB-tXX-

enriched region. The SM Higgs boson signal is assumed to have a mass of $m_H = 125 \text{ GeV}$. The uncertainty in the prediction is shown by the hatched band, calculated as described in Sect. 7. For comparison only, the hatched band includes the theoretical uncertainties in the SM cross-section for the signal and the background processes

category, which removes the use of simulation to estimate the event fractions in these categories.

The control regions used to estimate this background are defined by closely following the requirements outlined in Sect. 4.2. The definition and modified requirements for each of the four control regions are:

1. an enhanced heavy-flavour control region with inverted impact-parameter and relaxed isolation requirements on the subleading lepton pair and relaxed vertex χ^2 requirements,

2. an enhanced $tt e\mu + \mu\mu$ control region with an opposite-flavour leading lepton pair $e\mu$ and relaxed impact-parameter, isolation, and opposite-sign charge requirements on the subleading lepton pair $\mu\mu$, as well as relaxed vertex χ^2 requirements,
3. an enhanced light-flavour control region with inverted isolation requirements for at least one lepton in the sub-leading lepton pair, and
4. a same-sign $\ell\ell + \mu^\pm\mu^\pm$ control region with relaxed impact-parameter and isolation requirements.

The first two are the primary control regions used to estimate $Z + \text{jets}$ and tt , and the latter two improve the estimate by reducing the statistical error of the fitted normalisation.

The background normalisations are obtained separately for the $Z + \text{jets}$ and tt background processes using the simultaneous fit in the four control regions. The normalisation n_i^{CR} in each control region CR for the background process i is expressed as a fraction, $n_i^{CR} = t_i^{CR} \times N_i^{VR}$, of the normalisation N_i^{VR} in a dedicated relaxed validation region (VR). N_i^{VR} is used as the common parameter when fitting the normalisations in the different CRs. The transfer factor t_i^{CR} is the ratio of the background contribution in the relaxed validation region and the given control regions. The relaxed validation region is defined by following the requirements outlined in Sect. 4.2 but by relaxing the impact-parameter and isolation requirements on the subleading lepton pair. This region contains a substantially larger number of events compared with the other four control regions, allowing a more reliable prediction of the shapes of the NN distributions. The shapes of the background NN distribution are then extrapolated together with the corresponding background normalisation from the relaxed validation to the signal region by means of additional transfer factors T_i . Transfer factors t_i^{CR} and T_i to extrapolate the background contributions from the control regions to the relaxed validation region and from there to the signal region are estimated from simulation and validated in several additional data control regions

The $\ell\ell + ee$ control-region selection requires the electrons in the subleading lepton pair to have the same charge, and relaxes the identification, impact parameter and isolation requirements on the electron candidate with the lowest transverse energy. This fake electron candidate, denoted by X , can be a light-flavour jet, an electron from photon conversion or an electron from heavy-flavour hadron decay. The heavy-flavour background is determined from simulation. Good agreement is observed between simulation and data in a heavy-flavour enriched control region.

The remaining background is separated into light-flavour and photon conversion background components using the sPlot method [156] which is performed on electron candidates X , separately for each reconstructed category in bins of the jet multiplicity and the transverse momentum of the electron candidate. The size of the two background components is obtained from a fit to the number of hits from the electron candidate X in the innermost ID layer in the $\ell\ell + ee$ data control region, where a hit indicates either a hadron track or an early conversion. A hit in the next-to-innermost pixel layer is used when the electron falls in a region that was either not instrumented with an innermost pixel layer module or where the module was not operating. The templates of the final discriminants for the mentioned fit of the light-flavour and photon conversion background components are obtained from simulated $Z + X$ events with an on-shell Z boson decay

candidate accompanied by an electron X selected using the same criteria as in the $\ell\ell + ee$ control region. The simulated $Z + X$ events are also used to obtain the transfer factor for the X candidate for the extrapolation of the light-flavour and photon conversion background contributions from the $\ell\ell + ee$ control region to the signal region, after correcting the simulation to match the data in dedicated control samples of $Z + X$ events. The extrapolation to the signal region is also performed in bins of the electron transverse momentum and the jet multiplicity, separately for each reconstructed event category. A method similar to that for the $\ell\ell + \mu\mu$ final state is used to extract the NN shape, where the fractions of events from light-flavour jets and photon conversions are estimated from simulation and corrected transfer factors are used.

7 Systematic uncertainties

The systematic uncertainties are categorised into experimental and theoretical uncertainties. The first category includes uncertainties in lepton and jet reconstruction, identification, isolation and trigger efficiencies, energy resolution and scale, and uncertainty in the total integrated luminosity. Uncertainties from the procedure used to derive the data-driven background estimates are also included in this category. The second category includes uncertainties in theoretical modelling of the signal and background processes.

The uncertainties can affect the signal acceptance, selection efficiency and discriminant distributions as well as the background estimates. The dominant sources of uncertainty and their effect are described in the following subsections. The impact of these uncertainties on the measurements is summarised in Table 6.

7.1 Experimental uncertainties

The uncertainty in the combined 2015–2018 integrated luminosity is 1.7% [157], obtained using the LUCID-2 detector [158] for the primary luminosity measurements. This uncertainty affects the signal and the normalisation of the simulated background estimates when not constrained by the data sidebands.

The uncertainty in the predicted yields due to pile-up modelling ranges between 1% and 2% and is derived by varying the average number of pile-up events in the simulation to cover the uncertainty in the ratio of the predicted to measured inelastic cross-sections [159].

The electron (muon) reconstruction, isolation and identification efficiencies, and the energy (momentum) scale and resolution are derived from data using large samples of $J/\psi \rightarrow \ell\ell$ and $Z \rightarrow \ell\ell$ decays [129, 131]. Typical uncertainties in the predicted yields for the relevant decay channels

Table 6 The impact of the dominant systematic uncertainties (in percent) on the cross-sections in production bins of the Production Mode Stage and the Reduced Stage 1.1. Similar sources of systematic uncertainties are grouped together: luminosity (Lumi.), electron/muon reconstruction and identification efficiencies and pile-up modelling (e, μ , pile-up), jet energy scale/resolution and b -tagging efficiencies (Jets, flav. tag), uncertainties in reducible background (reducible bkg), theo-

retical uncertainties in ZZ^* background and tXX background, and theoretical uncertainties in the signal due to parton distribution function (PDF), QCD scale (QCD) and parton showering algorithm (Shower). The uncertainties are rounded to the nearest 0.5%, except for the luminosity uncertainty, which is measured to be 1.7% and increases for the VH signal processes due to the simulation-based normalisation of the VVV background

Measurement	Experimental uncertainties [%]				Theory uncertainties [%]				
	Lumi.	e, μ , pile-up	Jets, flav. tag	Reducible bkg	Background		Signal		
					ZZ^*	tXX	PDF	QCD	Shower
Inclusive cross-section									
	1.7	2.5	0.5	< 0.5	1	< 0.5	< 0.5	1	2
Production mode cross-sections									
ggF	1.7	2.5	1	< 0.5	1.5	< 0.5	0.5	1	2
VBF	1.7	2	4	< 0.5	1.5	< 0.5	1	5	7
VH	1.9	2	4	1	6	< 0.5	2	13.5	7.5
ttH	1.7	2	6	< 0.5	1	0.5	0.5	12.5	4
Reduced Stage-1.1 production bin cross-sections									
gg2H-0j- p_T^H -Low	1.7	3	1.5	0.5	6.5	< 0.5	< 0.5	1	1.5
gg2H-0j- p_T^H -High	1.7	3	5	< 0.5	3	< 0.5	< 0.5	0.5	5.5
gg2H-1j- p_T^H -Low	1.7	2.5	12	0.5	7	< 0.5	< 0.5	1	6
gg2H-1j- p_T^H -Med	1.7	3	7.5	< 0.5	1	< 0.5	< 0.5	1.5	5.5
gg2H-1j- p_T^H -High	1.7	3	11	0.5	2	< 0.5	< 0.5	2	7.5
gg2H-2j	1.7	2.5	16.5	1	12.5	0.5	< 0.5	2.5	10.5
gg2H- p_T^H -High	1.7	1.5	3	0.5	3.5	< 0.5	< 0.5	2	3.5
qq2Hqq- VH	1.8	4	17	1	4	1	0.5	5.5	8
qq2Hqq-VBF	1.7	2	3.5	< 0.5	5	< 0.5	< 0.5	6	10.5
qq2Hqq-BSM	1.7	2	4	< 0.5	2.5	< 0.5	< 0.5	3	8
VH -Lep	1.8	2.5	2	1	2	0.5	< 0.5	1.5	3
ttH	1.7	2.5	5	0.5	1	0.5	< 0.5	11	3

due to the identification and reconstruction efficiency uncertainties are below 1% for muons and 1%–2% for electrons. The uncertainty in the expected yields due to the muon and electron isolation efficiency is also taken into account, with the typical size being 1%. The uncertainties in the trigger efficiencies have a negligible impact. The uncertainties in the electron and muon energy and momentum scale and resolution are small and also have a negligible impact on the measurements.

The uncertainties in the jet energy scale and resolution are in the range 1%–3% [133]. The impact of these uncertainties is more relevant for the VH , VBF and ttH production mode cross-sections (3%–5%) and for all the Reduced Stage-1.1 cross-section measurements, including the ggF process split into the different N_{jets} exclusive production bins (5%–20%).

The uncertainty in the calibration of the b -tagging algorithm, which is derived from dileptonic tt events, amounts to a few percent over most of the jet p_T range [138]. This uncertainty is only relevant in the ttH category, with its expected

impact being approximately 1% in the ttH cross-section measurement. The uncertainties associated with the E_T^{miss} reconstruction have a negligible impact.

A shift in the simulated Higgs boson mass corresponding to the precision of the Higgs boson measurement, $m_H = 125.09 \pm 0.24$ GeV [160], is shown to have a negligible impact on the signal acceptance. A small dependency of the NN_{ggF} discriminant shape in the 0j- $p_T^{4\ell}$ -Low and 0j- $p_T^{4\ell}$ -Med categories on m_H is observed for the signal (below 2% in the highest NN score bins) and is included in the signal model. This uncertainty affects the measurement of ggF production, as well as the measurements in other production bins with large ggF contamination.

For the data-driven measurement of the reducible background, three sources of uncertainty are considered: statistical uncertainty, overall systematic uncertainty for each of $\ell\ell + \mu\mu$ and $\ell\ell + ee$, and a shape systematic uncertainty that varies with the reconstructed event category. Since the yields are estimated by using a statistical fit to a control data

region with large statistics, the inclusive background estimate has a relatively small (3%) statistical uncertainty. The systematic uncertainty for $\ell\ell + \mu\mu$ and the heavy-flavour component of $\ell\ell + ee$ is estimated by comparing the lepton identification, isolation and impact parameter significance efficiency between data and simulated events in a separate region, enriched with on-shell Z boson decays accompanied by an electron or a muon. For both the $\ell\ell + \mu\mu$ and $\ell\ell + ee$ estimates, the difference in efficiency is assigned as the uncertainty in the extrapolation of the yield estimate from the control region to the signal region. For the $\ell\ell + ee$ light-flavour component, the efficiency is derived from an enriched control region with a systematic uncertainty estimated by varying the assumed light- and heavy-flavour components. These inclusive uncertainties (6%) are treated as correlated across the reconstructed event categories. Finally, there are additional uncorrelated uncertainties (8%–70%) in the fraction of the reducible background in each event category due to the statistical precision of the simulated samples.

7.2 Theoretical uncertainties

The theoretical modelling of the signal and background processes is affected by uncertainties due to missing higher-order corrections, modelling of parton showers and the underlying event, and PDF+ α_S uncertainties.

The impact of the theory systematic uncertainties on the signal depends on the kind of measurement that is performed. For signal-strength measurements, defined as the measured cross-section divided by the SM prediction, or interpretation of cross-section using the EFT approach, each source of theory uncertainty affects both the acceptance and the predicted SM cross-section. For the cross-section measurements, only effects on the acceptance need to be considered.

The impact of the theory systematic uncertainties on the background depends on the method of estimating the normalisation. If simulation is used, the uncertainties in the acceptance and the predicted SM cross-section are included. If the normalisation is estimated from a data-driven method, only the impact on the relative event fractions between categories is considered.

One of the dominant sources of theoretical uncertainty is the prediction of the ggF process in the different N_{jets} categories. The ggF process gives a large contribution in categories with at least two jets. To estimate the variations due to the impact of higher-order contributions not included in the calculations and migration effects on the N_{jets} ggF cross-sections, the approach described in Refs. [24, 161] is used, which exploits the latest predictions for the inclusive jet cross-sections. In particular, the uncertainty from the choice of factorisation and renormalisation scales, the choice of resummation scales, and the migrations between the 0-jet and 1-jet phase-space bins or between the 1-jet and ≥ 2 -

jet bins are considered [24, 162–164]. The impact of QCD scale variations on the Higgs boson p_T distribution is taken into account as an additional uncertainty. The uncertainty in higher-order corrections to the Higgs boson p_T originating from the assumption of infinite top quark mass in the heavy-quark loop is also taken into account by comparing the p_T distribution predictions to finite-mass calculations. An additional uncertainty in the acceptance of the ggF process in VBF topologies [165] due to missing higher orders in QCD in the calculation is estimated by variations of the renormalisation and factorisation scales using fixed-order calculations with MCFM [166]. An additional uncertainty in the Higgs boson p_T distribution, derived by varying the renormalisation, factorisation and NNLOPS scale in the simulation, in the 0-jet topology is considered. This is particularly relevant when measuring the inclusive ggF cross-section using the $p_T^{4\ell}$ categories for events with no jet activity. To account for higher-order corrections to p_T^{Hjj} , which is used as an NN input variable, the uncertainty is derived by comparing the predicted distribution obtained using POWHEG NNLOPS and MADGRAPH5_aMC@NLO with the FxFx merging scheme.

For the VBF production mode, the uncertainty due to missing higher orders in QCD is parameterised using the scheme outlined in Ref. [23]. The migration effects due to the selection criteria imposed on the number of jets, transverse momentum of the Higgs boson, transverse momentum of the Higgs boson and the leading dijet system and the invariant mass of the two leading jets, used to define the full Stage 1.1 STXS production bins, are computed by varying the renormalisation and factorisation scales by a factor of two. The uncertainties are cross-checked with fixed-order calculations. Similarly, for the VH production mode with the associated V decaying leptonically, the scale variations are parameterised as migration effects due to the selection criteria imposed on the number of jets and the transverse momentum of the associated boson [167].

For the VH production mode with the associated V decaying hadronically and the ttH production mode, the uncertainty due to missing higher orders in QCD is obtained by varying the renormalisation and factorisation scales by a factor of two. The configuration with the largest impact, as quantified by the relative difference between the varied and the nominal configuration, is chosen to define the uncertainty in each experimental category. These uncertainties are treated as uncorrelated among the different production modes. Due to the limited accuracy of the simulated samples, the uncertainties evaluated using this method for the total cross-sections are larger than those described in Ref. [24].

The uncertainties in the acceptance due to the modelling of parton showers and the underlying event are estimated with AZNLO tune eigenvector variations and by comparing the acceptance using the parton showering algorithm from

PYTHIA 8 with that from HERWIG 7 [168] for all signal processes. The uncertainty due to each AZNLO tune variation is taken as correlated among the different production modes while the difference between the parton showering algorithms is treated as an uncorrelated uncertainty. The uncertainties due to higher-order corrections to the Higgs boson decay are modelled using the PROPHECY4F [102, 105] and HTO4L [104, 169] generators. These corrections are below 2% and have a negligible impact on the results. A 100% uncertainty is assigned to heavy-flavour quark production modelling for the ggF contribution entering in the ttH category. This has a negligible impact on the results.

The impact of the PDF uncertainty is estimated with the thirty eigenvector variations of the PDF4LHC_NLO_30 Hessian PDF set following the PDF4LHC recommendations [40]. The modification of the predictions originating from each eigenvector variation is added as a separate source of uncertainty in the model. The same procedure is applied for the ggF, VBF, VH and ttH processes, enabling correlations to be taken into account in the fit model.

The impacts of the theoretical uncertainties, as described above, on the shape of NN discriminants are also considered. For ggF production, a further cross-check is performed by comparing the NN shapes in the corresponding categories as predicted by POWHEG NNLOPS and MADGRAPH5_AMC@NLO with the FxFx merging scheme. All the NN shapes from the two generators agree within the scale variations and, therefore, no additional shape uncertainty is included.

For signal-strength measurements, an additional uncertainty related to the $H \rightarrow ZZ^*$ branching ratio prediction [102, 105] is included in the measurement.

Since the normalisation of the ZZ^* process in most reconstructed event categories is constrained by performing a simultaneous fit to sideband regions enriched in this contribution together with the signal regions, most of the theoretical uncertainty in the normalisation for this background vanishes. Nevertheless, uncertainties in the shapes of the discriminants for the ZZ^* background and in the relative contribution of this background between the sidebands and the signal regions are taken into account. The uncertainties due to missing higher-order effects in QCD are estimated by varying the factorisation and renormalisation QCD scales by a factor of two; the impact of the PDF uncertainty is estimated by using the MC replicas of the NNPDF3.0 PDF set. Uncertainties due to parton shower modelling for the ZZ^* process are considered as well. The impact of these uncertainties is below 2% for all production mode cross-sections measured. In addition, a comparison between SHERPA and POWHEG is also taken as an additional source of systematic uncertainty. This model uncertainty is treated as uncorrelated among the different sideband-to-signal region extrapolations (in 0-jet, 1-jet and 2-jet categories).

The uncertainty in the gluon-initiated and the vector-boson-initiated ZZ^* process is taken into account by changing the relative composition of the quark-initiated, the gluon-initiated and the vector-boson-scattered ZZ^* components according to the theoretical uncertainty in the predicted cross-sections and the respective K -factors. In addition, the event yield and NN discriminant shapes in each event category are compared with the data in an $m_{4\ell}$ sideband around the signal region ($105 \text{ GeV} < m_{4\ell} < 115 \text{ GeV}$ or $130 \text{ GeV} < m_{4\ell} < 160 \text{ GeV}$). Good agreement between the SHERPA predictions and the data is found.

For the tXX process, uncertainties due to PDF and QCD scale variations are considered in the relative fraction of events present in the ttH -like categories, in the SB- tXX -enriched control region and in the NN discriminant shape. Differences between MADGRAPH5_AMC@NLO and SHERPA are considered as an additional systematic uncertainty. For all other categories where this process is estimated from simulation, the impact of these uncertainties on the SM cross-section and acceptance are also considered.

Uncertainties in the PDF and in missing higher-order corrections in QCD are applied to the VVV background estimate, which is fully taken from MC simulation.

To probe the tensor structure of the Higgs boson coupling in the EFT approach, theoretical uncertainties due to PDF and QCD scale variations are assigned to the signal predictions based on the simulated highest-order SM signal samples. The same uncertainties are assigned to all corresponding BSM signal predictions, since it is shown using the MC signal samples simulated at LO accuracy that the uncertainties change negligibly as a function of the Wilson coefficients.

8 Measurement of the Higgs boson production mode cross-sections

8.1 Observed data

The expected and observed four-lepton invariant mass (post-fit) distributions of the selected Higgs boson candidates after the event selection are shown in Fig. 5.

The observed and expected (post-fit) distributions of the jet multiplicity, the dijet invariant mass, and the four-lepton transverse momenta in different N_{jets} bins, which are used for the categorisation of reconstructed events, are shown in Fig. 6 for different steps of the event categorisation.

The expected numbers of signal and background events in each reconstructed event category are shown in Table 7 together with the corresponding observed number of events. The expected event yields are in good agreement with the observed ones. The observed and expected (post-fit) distributions of the NN discriminants are shown in Fig. 7 and in Figure 8. In addition, Fig. 8g, h show the observed and expected yields in the categories where no NN discriminant

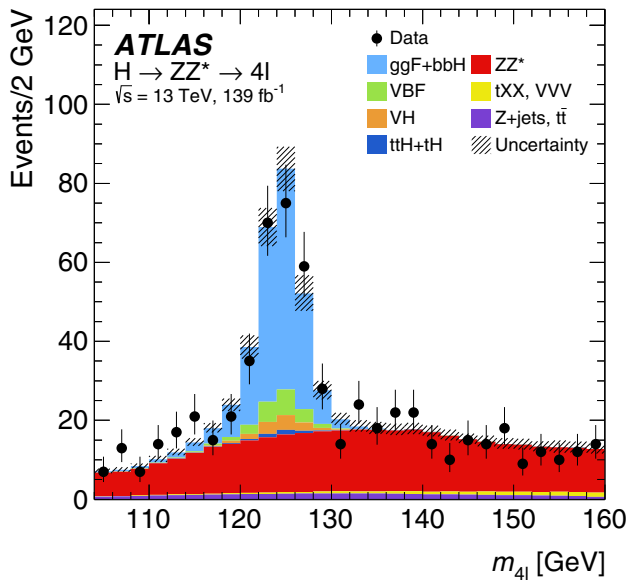


Fig. 5 The observed and expected (post-fit) four-lepton invariant mass distributions for the selected Higgs boson candidates, shown for an integrated luminosity of 139 fb^{-1} at $\sqrt{s} = 13 \text{ TeV}$. The SM Higgs boson signal is assumed to have a mass $m_H = 125 \text{ GeV}$. The uncertainty in the prediction is shown by the hatched band, calculated as described in Sect. 7. For comparison only, the hatched band includes the theoretical uncertainties in the SM cross-section for the signal and the background processes

is used and in the mass sidebands used to constrain the ZZ^* and tXX background, respectively. All distributions are in good agreement with the data.

The statistical interpretation of the results and compatibility with the SM are discussed in the following.

8.2 Measurement of simplified template cross-sections

To measure the product $\vec{\sigma} \cdot \mathcal{B}$ of the Higgs boson production cross-section and the branching ratio for $H \rightarrow ZZ^*$ decay for the production bins of the Production Mode Stage or the Reduced Stage 1.1, a fit to the discriminant observables introduced in Sect. 5.2 is performed using the likelihood function $\mathcal{L}(\vec{\sigma}, \vec{\theta})$ that depends on the Higgs boson production cross-section $\vec{\sigma} = \{\sigma_1, \sigma_2, \dots, \sigma_N\}$ where σ_p is the cross-section in each production bin p and the nuisance parameters $\vec{\theta}$ accounting for the systematic uncertainties. The likelihood function is defined as a product of conditional probabilities over binned distributions of the discriminating observables in each reconstructed signal and sideband event category j ,

$$\mathcal{L}(\vec{\sigma}, \vec{\theta}) = \prod_j^{N_{\text{categories}}} \prod_i^{N_{\text{bins}}} P(N_{i,j} | L \cdot \vec{\sigma} \cdot \mathcal{B} \cdot \vec{A}_{i,j}(\vec{\theta}) + B_{i,j}(\vec{\theta})) \times \prod_m^{N_{\text{nuisance}}} C_m(\vec{\theta}), \tag{3}$$

with Poisson distributions P corresponding to the observation of $N_{i,j}$ events in each histogram bin i of the discriminating observable given the expectations for each background process, $B_{i,j}(\vec{\theta})$, and for the signal, $S_{i,j}(\vec{\theta}) = L \cdot \vec{\sigma} \cdot \mathcal{B} \cdot \vec{A}_{i,j}(\vec{\theta})$, where L is the integrated luminosity and $\vec{A}_{i,j} = \{A_{i,j}^1, A_{i,j}^2, \dots, A_{i,j}^N\}$ is the set of signal acceptances from each production bin. The signal acceptance $A_{i,j}^p$ is defined as the fraction of generated signal events in the production bin p that satisfy the event reconstruction and selection criteria in the histogram bin i of the reconstructed event category j . For a given production bin p , the acceptance consists of $A_{i,j}^p = a^p \cdot \epsilon_{i,j}^p$, where a^p is the particle-level acceptance in the fiducial region defined from requirements listed in Sects. 4 and 5 and $\epsilon_{i,j}^p$ is the reconstruction efficiency of these particle-level events. Constraints on the nuisance parameters corresponding to systematic uncertainties described in Sect. 7 are represented by the functions $C_m(\vec{\theta})$. The cross-sections are treated as independent parameters for each production bin and correlated among the different reconstructed event categories. The test statistic used to perform the measurements is the ratio of profile likelihoods [170],

$$q(\vec{\sigma}) = -2 \ln \frac{\mathcal{L}(\vec{\sigma}, \hat{\vec{\theta}}(\vec{\sigma}))}{\mathcal{L}(\hat{\vec{\sigma}}, \hat{\vec{\theta}})},$$

where $\vec{\sigma}$ represents only the cross-section(s) considered as parameter(s) of interest in a given fit. The likelihood in the numerator is the estimator of a conditional fit, i.e. with parameter(s) of interest σ_i fixed to a given value, while the remaining cross-sections and nuisance parameters are free-floating parameters in the fit. The values of the nuisance parameters $\hat{\vec{\theta}}(\vec{\sigma})$ maximise the likelihood on the condition that the parameters of interest are held fixed to a given value. The likelihood in the denominator is the estimator of an unconditional fit in which all $\vec{\sigma}$ and $\vec{\theta}$ parameters are free parameters of the fit. The parameter of interest σ in each production bin is alternatively replaced by $\mu \cdot \sigma_{\text{SM}}(\vec{\theta})$, allowing an interpretation in terms of the signal strength μ relative to the SM prediction $\sigma_{\text{SM}}(\vec{\theta})$.

Assuming that the relative signal fractions in each production bin are given by the predictions for the SM Higgs boson, the inclusive $H \rightarrow ZZ^*$ production cross-section for $|y_H| < 2.5$ is measured to be:

$$\begin{aligned} \sigma \cdot \mathcal{B} &\equiv \sigma \cdot \mathcal{B}(H \rightarrow ZZ^*) \\ &= 1.34 \pm 0.11(\text{stat.}) \pm 0.04(\text{exp.}) \pm 0.04(\text{th.}) \text{ pb} \\ &= 1.34 \pm 0.12 \text{ pb}, \end{aligned}$$

where the uncertainties are either statistical (stat.) or of experimental (exp.) or theoretical (th.) systematic nature.

The SM prediction is $(\sigma \cdot \mathcal{B})_{\text{SM}} \equiv (\sigma \cdot \mathcal{B}(H \rightarrow ZZ^*))_{\text{SM}} = 1.33 \pm 0.08 \text{ pb}$. The data are also interpreted in terms of the global signal strength, yielding

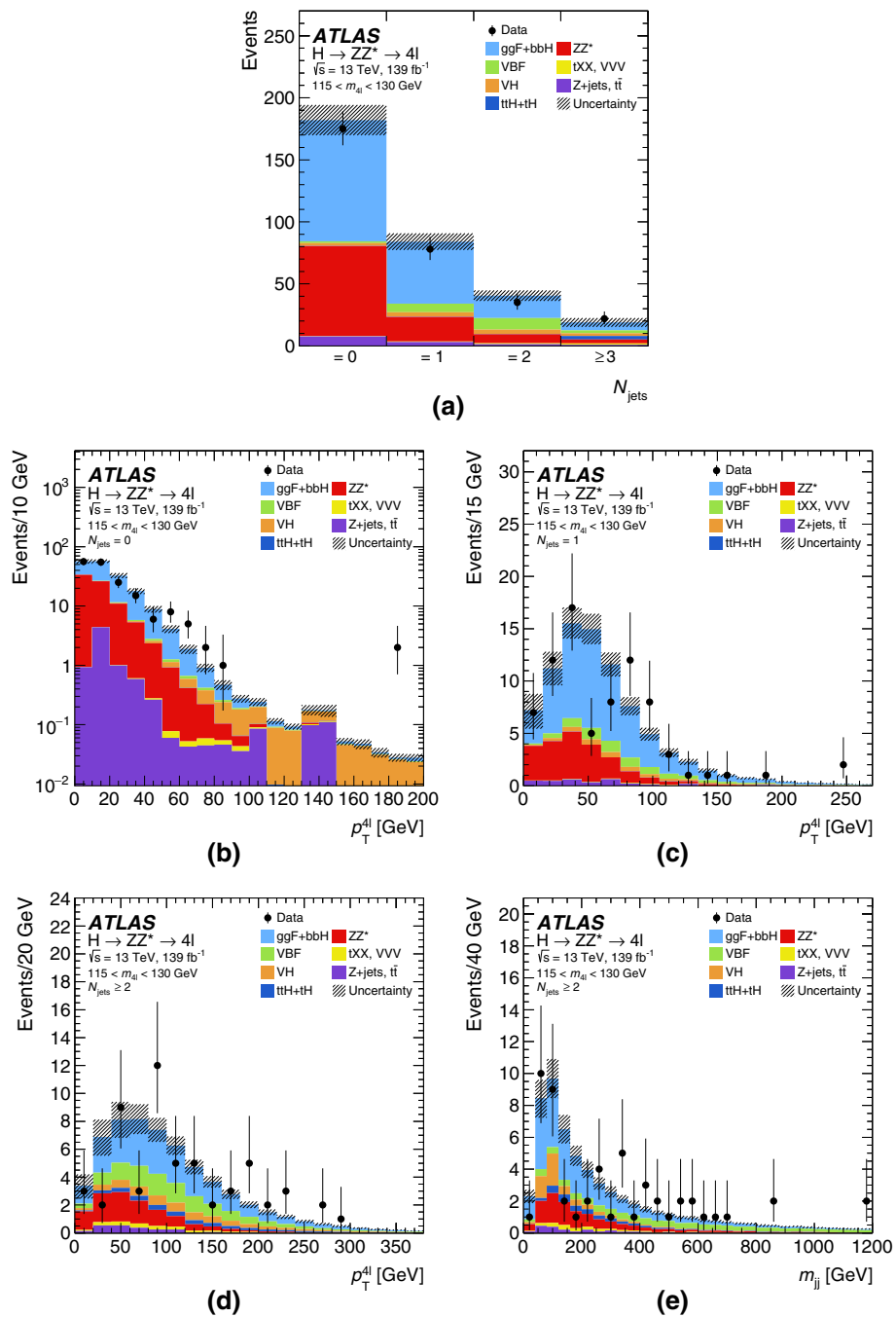


Fig. 6 The observed and expected distributions (post-fit) of (a) the jet multiplicity N_{jets} after the inclusive event selection, the four-lepton transverse momenta $p_T^{4\ell}$ for events with (b) exactly zero jets, (c) with exactly one jet and (d) with at least two jets and (e) the dijet invariant mass m_{jj} for events with at least two jets. The SM Higgs boson

signal is assumed to have a mass $m_H = 125$ GeV. The uncertainty in the prediction is shown by the hatched band, calculated as described in Sect. 7. For comparison only, the hatched band includes the theoretical uncertainties in the SM cross-section for the signal and the background processes

$$\begin{aligned} \mu &= 1.01 \pm 0.08(\text{stat.}) \pm 0.04(\text{exp.}) \pm 0.05(\text{th.}) \\ &= 1.01 \pm 0.11. \end{aligned}$$

The measured cross-section and signal strength are in an excellent agreement with the SM prediction, with a p -value of 98.6% for both compatibility tests.

The corresponding likelihood functions are shown in Fig. 9. The dominant systematic uncertainty in the cross-section measurement is the experimental uncertainty in the lepton efficiency and integrated luminosity measurements and theoretical uncertainties related to parton shower mod-

Table 7 The expected (pre-fit) and observed numbers of events for an integrated luminosity of 139 fb^{-1} at $\sqrt{s} = 13 \text{ TeV}$ in the signal region $115 < m_{4\ell} < 130 \text{ GeV}$ and sideband region $105 < m_{4\ell} < 115 \text{ GeV}$ or $130 < m_{4\ell} < 160 \text{ GeV}$ (350 GeV for tXX -enriched) in each reconstructed event category assuming the SM Higgs boson signal with a mass $m_H = 125 \text{ GeV}$. The sum of the expected number of SM Higgs

boson events and the estimated background yields is compared with the data. Combined statistical and systematic uncertainties are included for the predictions. Expected contributions that are below 0.2% of the total yield in each reconstructed event category are not shown and replaced by ‘-’

Reconstructed event category	Signal	ZZ^* background	tXX background	Other backgrounds	Total expected	Observed
Signal						
$115 < m_{4\ell} < 130 \text{ GeV}$						
$0j\text{-}p_T^{4\ell}\text{-Low}$	24.2 ± 3.5	30 ± 4	–	0.93 ± 0.13	55 ± 5	56
$0j\text{-}p_T^{4\ell}\text{-Med}$	76 ± 8	37 ± 4	–	6.5 ± 0.6	120 ± 9	117
$0j\text{-}p_T^{4\ell}\text{-High}$	0.355 ± 0.031	0.020 ± 0.012	0.0094 ± 0.0027	0.30 ± 0.05	0.69 ± 0.06	1
$1j\text{-}p_T^{4\ell}\text{-Low}$	34 ± 4	15.5 ± 2.7	–	1.91 ± 0.29	52 ± 5	41
$1j\text{-}p_T^{4\ell}\text{-Med}$	20.8 ± 2.8	4.0 ± 0.7	0.114 ± 0.013	1.02 ± 0.19	26.0 ± 2.9	31
$1j\text{-}p_T^{4\ell}\text{-High}$	4.7 ± 0.8	0.48 ± 0.10	0.043 ± 0.008	0.27 ± 0.04	5.5 ± 0.8	4
$1j\text{-}p_T^{4\ell}\text{-BSM-like}$	1.23 ± 0.23	0.069 ± 0.031	0.0067 ± 0.0031	0.062 ± 0.012	1.37 ± 0.23	2
$2j$	38 ± 5	9.1 ± 2.7	0.95 ± 0.08	2.13 ± 0.31	50 ± 6	48
$2j\text{-BSM-like}$	3.3 ± 0.6	0.18 ± 0.06	0.032 ± 0.005	0.091 ± 0.017	3.6 ± 0.6	6
$VH\text{-Lep-enriched}$	1.29 ± 0.07	0.156 ± 0.025	0.039 ± 0.009	0.0194 ± 0.0032	1.50 ± 0.08	1
$ttH\text{-Had-enriched}$	1.02 ± 0.18	0.058 ± 0.025	0.252 ± 0.032	0.119 ± 0.033	1.45 ± 0.18	2
$ttH\text{-Lep-enriched}$	0.42 ± 0.04	0.002 ± 0.005	0.0157 ± 0.0023	0.0028 ± 0.0029	0.44 ± 0.04	1
Sideband						
$105 < m_{4\ell} < 115 \text{ GeV}$ or $130 < m_{4\ell} < 160 \text{ GeV}$						
$SB\text{-}0j$	4.5 ± 0.5	150 ± 13	–	16.2 ± 2.2	171 ± 13	183
$SB\text{-}1j$	2.80 ± 0.30	51 ± 7	1.29 ± 0.16	8.4 ± 1.2	63 ± 7	64
$SB\text{-}2j$	2.02 ± 0.27	25 ± 7	4.4 ± 0.5	6.0 ± 0.9	38 ± 7	41
$SB\text{-}VH\text{-Lep-enriched}$	0.273 ± 0.015	0.48 ± 0.06	0.125 ± 0.018	0.126 ± 0.019	1.00 ± 0.07	3
$105 < m_{4\ell} < 115 \text{ GeV}$ or $130 < m_{4\ell} < 350 \text{ GeV}$						
$SB\text{-}tXX\text{-enriched}$	0.071 ± 0.012	0.32 ± 0.12	12.1 ± 1.3	0.84 ± 0.33	13.3 ± 1.4	19

elling affecting the acceptance. The signal-strength measurement is also affected by the theoretical uncertainty in the ggF cross-section due to missing higher-order corrections in QCD.

The expected SM cross-section, the observed values of $\sigma \cdot \mathcal{B}(H \rightarrow ZZ^*)$ and their ratio for the inclusive production and in each production bin of the Production Mode Stage and the Reduced Stage 1.1 are shown in Table 8.

The corresponding values are summarised in Fig. 10. In the ratio calculation, uncertainties in the SM expectation are not taken into account. The Production Mode Stage and Reduced Stage-1.1 measurements agree with the predictions for the SM Higgs boson. The p -values of the corresponding compatibility tests are 91% and 77%, respectively.

For the qq2Hqq-VBF bin, most of the sensitivity to the VBF production mode comes from the phase space with $m_{jj} > 350 \text{ GeV}$ and $p_T^H < 200 \text{ GeV}$. To probe the VBF contribution more directly, the cross-sections in this and in the remaining phase space region of the qq2Hqq-VBF

bin are fitted separately to the data, simultaneously with the other Reduced Stage 1.1 bins, using the reconstruction categories described in Sect. 5. The cross-section in the $m_{jj} > 350 \text{ GeV}$ and $p_T^H < 200 \text{ GeV}$ phase space is measured to be $0.060^{+0.025}_{-0.020}$ pb compared with the predicted cross-section of $0.0335^{+0.0007}_{-0.0011}$ pb. This measurement has a correlation of 20% with the measurement in the gg2H-2j bin, while correlations with other bins are up to 50%.

The dominant contribution to the measurement uncertainty in the ggF Production Mode Stage bin originates from the same sources as in the inclusive measurement. For the VBF production bin, the dominant systematic uncertainties are related to parton showering modelling and jet energy scale and resolution uncertainties. The VBF, VH and ttH production bins are also affected by the theoretical uncertainties related to the modelling of the ggF process. For the Reduced Stage-1.1 bins, the dominant cross-section uncertainties are the jet energy scale and resolution, and parton shower uncertainties.

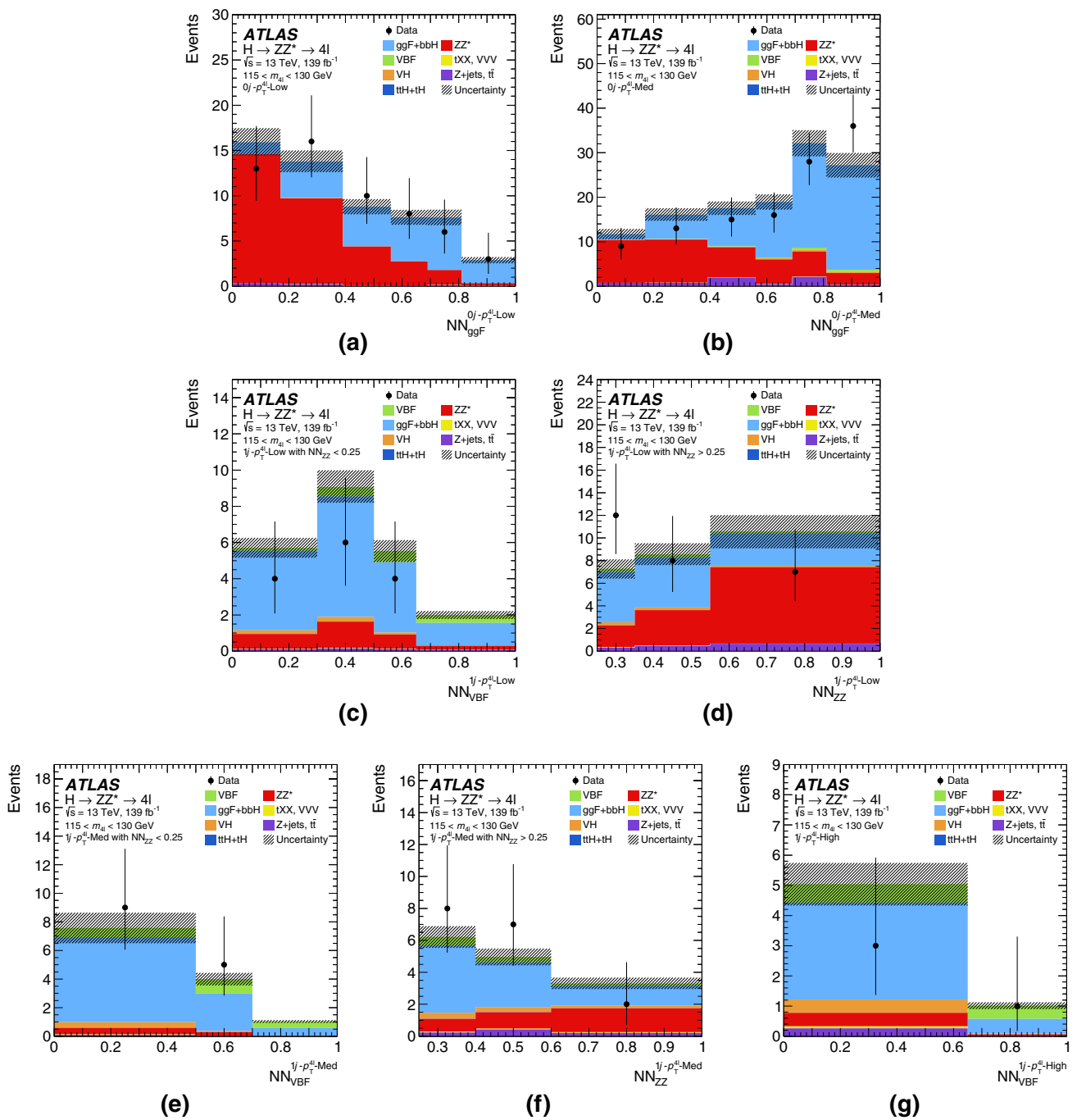


Fig. 7 The observed and expected NN output (post-fit) distributions for an integrated luminosity of 139 fb^{-1} at $\sqrt{s} = 13 \text{ TeV}$ in the different zero- and one-jet categories: (a) NN_{ggF} in $0j-p_T^{4\ell}$ -Low, (b) NN_{ggF} in $0j-p_T^{4\ell}$ -Med, (c) NN_{VBF} in $1j-p_T^{4\ell}$ -Low with $\text{NN}_{\text{ZZ}} < 0.25$, (d) NN_{ZZ} in $1j-p_T^{4\ell}$ -Low with $\text{NN}_{\text{ZZ}} > 0.25$, (e) NN_{VBF} in $1j-p_T^{4\ell}$ -Med with $\text{NN}_{\text{ZZ}} < 0.25$, (f) NN_{ZZ} in $1j-p_T^{4\ell}$ -Med with $\text{NN}_{\text{ZZ}} > 0.25$ and (g)

NN_{VBF} in $1j-p_T^{4\ell}$ -High. The SM Higgs boson signal is assumed to have a mass $m_H = 125 \text{ GeV}$. The uncertainty in the prediction is shown by the hatched band, calculated as described in Sect. 7. For comparison only, the hatched band includes the theoretical uncertainties in the SM cross-section for the signal and the background processes. The bin boundaries are chosen to maximise the significance of the targeted signal in each category

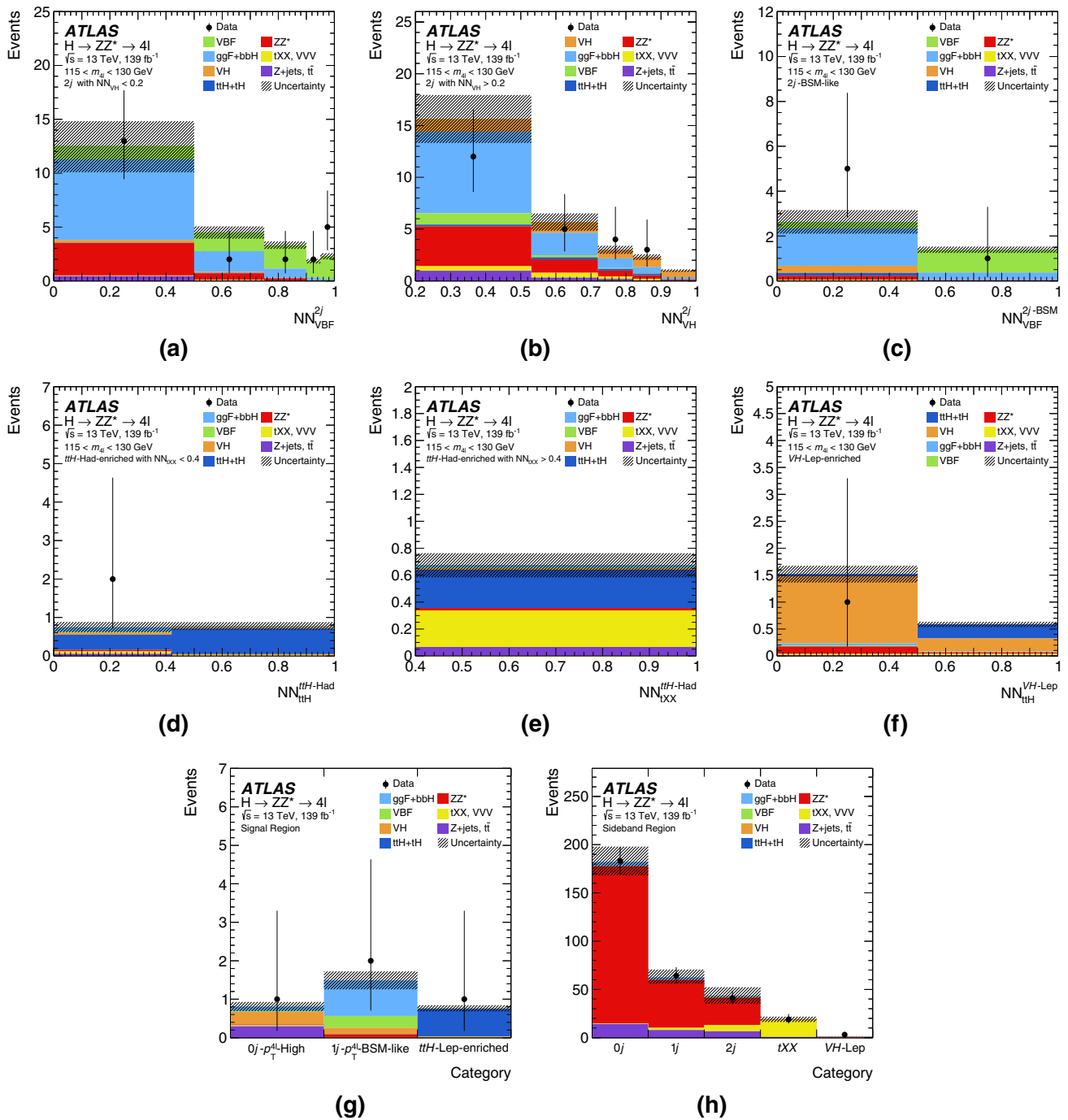


Fig. 8 The observed and expected NN output (post-fit) distributions for an integrated luminosity of 139 fb^{-1} at $\sqrt{s} = 13 \text{ TeV}$ in the different categories: (a) $\text{NN}_{\text{VBF}}^{2j}$ in $2j$ with $\text{NN}_{\text{VH}} < 0.2$, (b) $\text{NN}_{\text{VH}}^{2j}$ in $2j$ with $\text{NN}_{\text{VH}} > 0.2$, (c) $\text{NN}_{\text{VBF}}^{2j}$ in $2j$ -BSM-like, (d) NN_{ttH} in ttH -Had-enriched with $\text{NN}_{\text{tXX}} < 0.4$, (e) NN_{tXX} in ttH -Had-enriched with $\text{NN}_{\text{tXX}} > 0.4$ and (f) NN_{ttH} in VH -Lep-enriched. **g** Shows the categories where no NN discriminant is used while **h** shows the sidebands

used to constrain the ZZ^* and tXX backgrounds. The SM Higgs boson signal is assumed to have a mass $m_H = 125 \text{ GeV}$. The uncertainty in the prediction is shown by the hatched band, calculated as described in Sect. 7. For comparison only, the hatched band includes the theoretical uncertainties in the SM cross-section for the signal and the background processes. The bin boundaries are chosen to maximise the significance of the targeted signal in each category

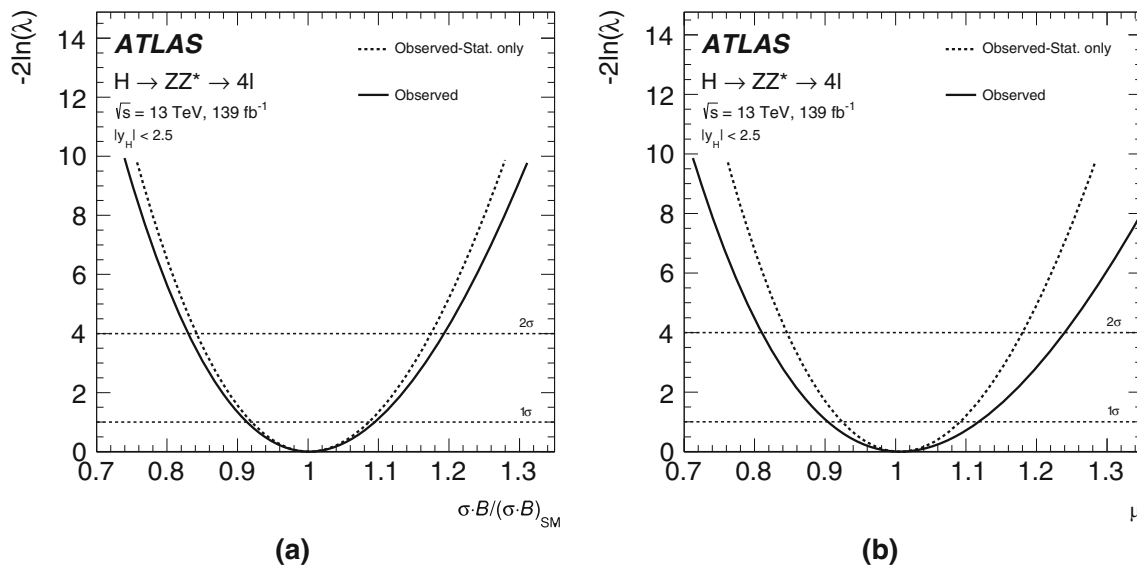


Fig. 9 Observed profile likelihood as a function of **(a)** $\sigma \cdot \mathcal{B}(H \rightarrow ZZ^*)$ normalised by the SM expectation and **(b)** the inclusive signal strength μ ; the scans are shown both with (solid line) and without (dashed line) systematic uncertainties

Table 8 The expected SM cross-section $(\sigma \cdot \mathcal{B})_{SM}$, the observed value of $\sigma \cdot \mathcal{B}$, and their ratio $(\sigma \cdot \mathcal{B})/(\sigma \cdot \mathcal{B})_{SM}$ for the inclusive production and for each Production Mode Stage and Reduced Stage-1.1 production bin for the $H \rightarrow ZZ^*$ decay for an integrated luminosity of 139 fb^{-1} at $\sqrt{s} = 13 \text{ TeV}$. The bbH (ttH) contribution is included in the ggF (ttH) production bins. The uncertainties are given as (stat.)+(exp.)+(th.)

for the inclusive cross-section and the Production Mode Stage, and as (stat.)+(syst.) for the Reduced Stage 1.1. The Reduced Stage-1.1 results are dominated by the statistical uncertainty and the impact of theory uncertainties is smaller than for the Production Mode Stage. The impact of the theory uncertainties for the Reduced Stage 1.1 is smaller than the least significant digit

Production bin	Cross-section ($\sigma \cdot \mathcal{B}$) [pb]		$(\sigma \cdot \mathcal{B})/(\sigma \cdot \mathcal{B})_{SM}$
	SM expected	Observed	Observed
Inclusive production, $ y_H < 2.5$			
	1.33 ± 0.08	$1.34 \pm 0.11 \pm 0.04 \pm 0.03$	$1.01 \pm 0.08 \pm 0.03 \pm 0.02$
Production Mode Stage bins, $ y_H < 2.5$			
ggF	1.17 ± 0.08	$1.12 \pm 0.12 \pm 0.04 \pm 0.03$	$0.96 \pm 0.10 \pm 0.03 \pm 0.03$
VBF	0.0920 ± 0.0020	$0.11 \pm 0.04 \pm 0.01 \pm 0.01$	$1.21 \pm 0.44^{+0.13}_{-0.08}^{+0.07}_{-0.05}$
VH	$0.0524^{+0.0027}_{-0.0049}$	$0.075^{+0.059}_{-0.047}^{+0.011}_{-0.007}^{+0.013}_{-0.009}$	$1.44^{+1.13}_{-0.90}^{+0.21}_{-0.14}^{+0.24}_{-0.17}$
ttH	$0.0154^{+0.0010}_{-0.0013}$	$0.026^{+0.026}_{-0.017} \pm 0.002 \pm 0.002$	$1.7^{+1.7}_{-1.2} \pm 0.2 \pm 0.2$
Reduced Stage-1.1 bins, $ y_H < 2.5$			
gg2H-0j- p_T^H -Low	0.176 ± 0.025	$0.17 \pm 0.05 \pm 0.02$	$0.96 \pm 0.30 \pm 0.09$
gg2H-0j- p_T^H -High	0.55 ± 0.04	$0.63 \pm 0.09 \pm 0.06$	$1.15 \pm 0.17 \pm 0.11$
gg2H-1j- p_T^H -Low	0.172 ± 0.025	$0.05 \pm 0.07^{+0.04}_{-0.06}$	$0.3 \pm 0.4^{+0.2}_{-0.3}$
gg2H-1j- p_T^H -Med	0.119 ± 0.018	$0.17 \pm 0.05^{+0.02}_{-0.01}$	$1.4 \pm 0.4 \pm 0.1$
gg2H-1j- p_T^H -High	0.020 ± 0.004	$0.009^{+0.016}_{-0.011} \pm 0.002$	$0.5^{+0.8}_{-0.6} \pm 0.1$
gg2H-2j	0.127 ± 0.027	$0.04 \pm 0.07 \pm 0.04$	$0.3 \pm 0.5 \pm 0.3$
gg2H- p_T^H -High	0.015 ± 0.004	$0.038^{+0.021}_{-0.016}^{+0.003}_{-0.002}$	$2.5^{+1.3}_{-1.0}^{+0.2}_{-0.1}$
qq2Hqq-VH	$0.0138^{+0.0004}_{-0.0006}$	$0.021^{+0.037}_{-0.029}^{+0.009}_{-0.006}$	$1.5^{+2.7}_{-2.1}^{+0.6}_{-0.4}$
qq2Hqq-VBF	$0.1076^{+0.0024}_{-0.0035}$	$0.15 \pm 0.05^{+0.02}_{-0.01}$	$1.4 \pm 0.5^{+0.2}_{-0.1}$
qq2Hqq-BSM	0.00420 ± 0.00018	$0.0005^{+0.0079}_{-0.0047} \pm 0.008$	$0.1^{+1.9}_{-1.1} \pm 0.2$
VH-Lep	0.0164 ± 0.0004	$0.022^{+0.028}_{-0.018}^{+0.003}_{-0.001}$	$1.3^{+1.7}_{-1.1}^{+0.2}_{-0.1}$
ttH	$0.0154^{+0.0010}_{-0.0013}$	$0.025^{+0.026}_{-0.017}^{+0.005}_{-0.003}$	$1.6^{+1.7}_{-1.1}^{+0.3}_{-0.2}$

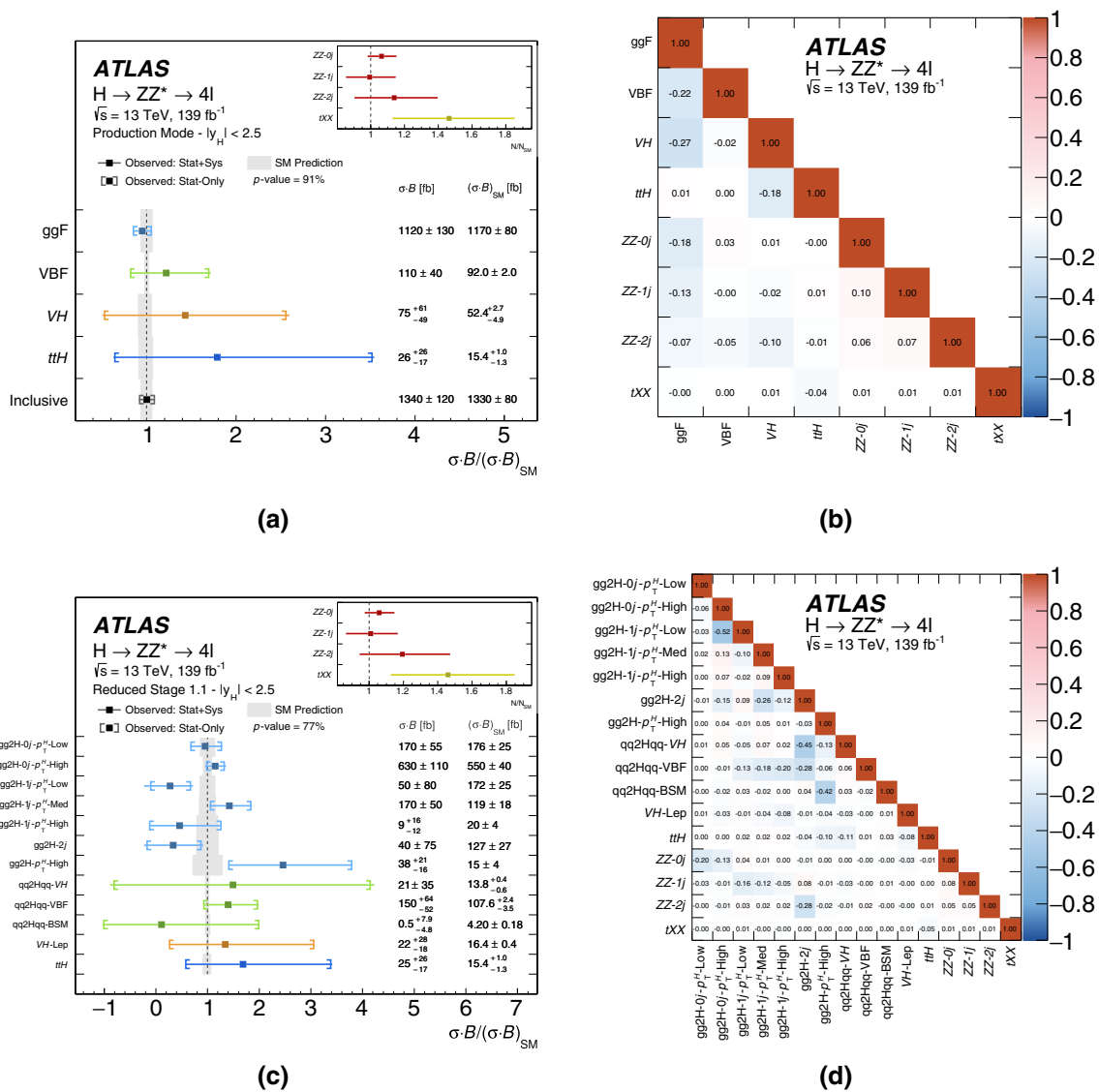


Fig. 10 The observed and expected SM values of the cross-sections $\sigma \cdot \mathcal{B}$ normalised by the SM expectation $(\sigma \cdot \mathcal{B})_{SM}$ for (a) the inclusive production and in the Production Mode Stage and (c) the Reduced Stage-1.1 production bins for an integrated luminosity of 139 fb^{-1} at $\sqrt{s} = 13 \text{ TeV}$. The fitted normalisation factors for the ZZ and tXX background are shown in the inserts. Different colours indicate dif-

ferent Higgs boson production modes (or background sources). The vertical band represents the theory uncertainty in the signal prediction. The correlation matrices between the measured cross-sections and the ZZ and tXX normalisation factors are shown for (b) the Production Mode Stage and (d) the Reduced Stage 1.1

Figure 11 shows the likelihood contours in the (ggF, VBF), (ggF, VH), (VBF, VH) and (gg2H-0j-p_T^H-Low, gg2H-0j-p_T^H-High) planes. The other cross-section parameters are left free in the fit, i.e. they are not treated as parameters of interest. The compatibility with the SM expectation is at the level of 0.22, 0.25, 0.19 and 0.33 standard deviations, respectively.

9 Constraints on the Higgs boson couplings in the κ -framework

The cross-sections measured at the Production Mode Stage are interpreted in the κ -framework described in Sect. 1.2. The relevant cross-sections and the branching ratio of Eq. (3) are parameterised in terms of the coupling-strength modifiers $\bar{\kappa}$. One interesting benchmark allows two different Higgs boson coupling-strength modifiers to fermions and bosons, reflecting the different structure of the interactions of the SM Higgs sector with gauge bosons and fermions. The universal coupling-strength modifiers κ_F for fermions and κ_V

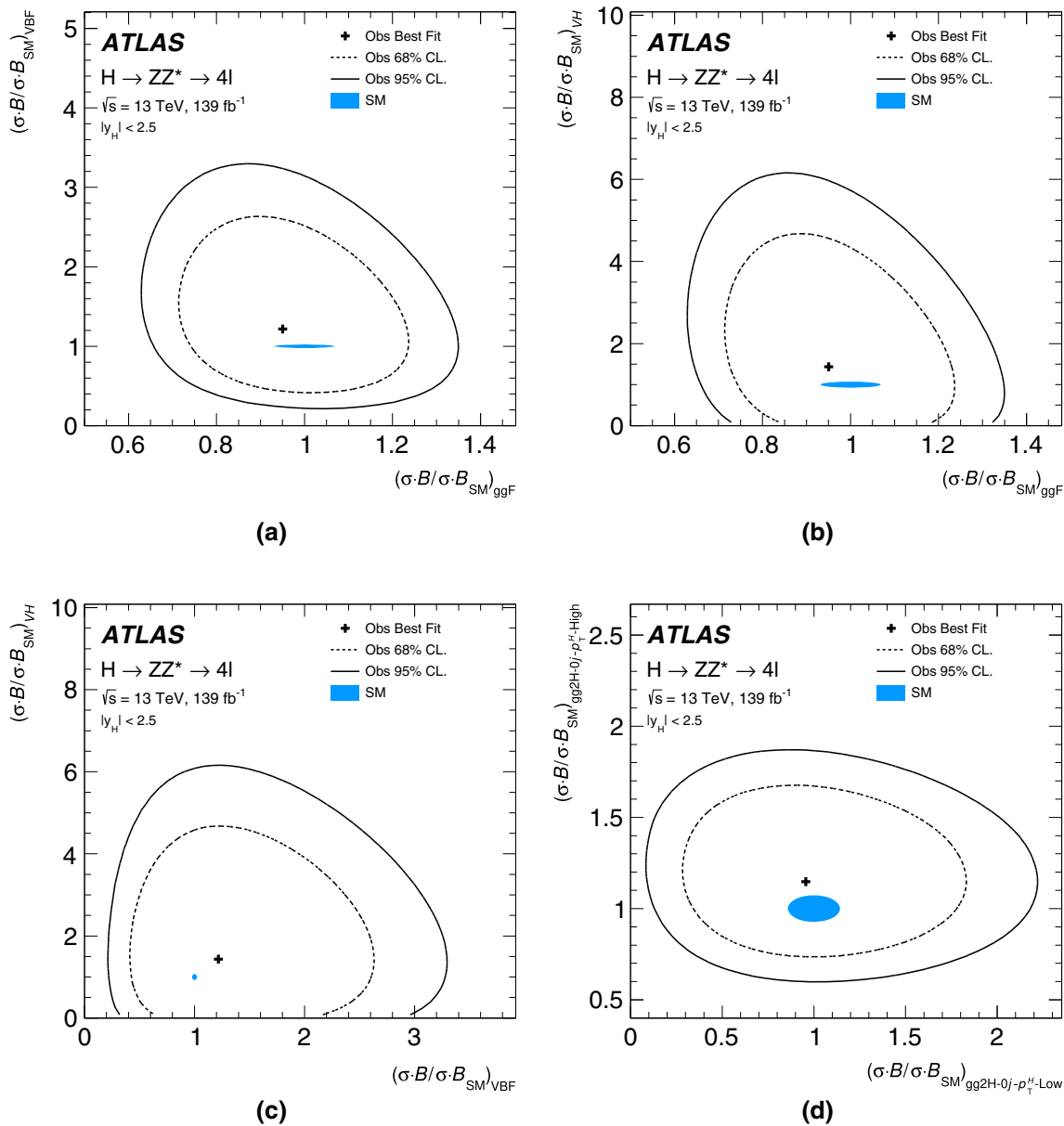


Fig. 11 Likelihood contours at 68% CL (dashed line) and 95% CL (solid line) in the (a) (ggF, VBF), (b) (ggF, VH), (c) (VBF, VH) and (d) (gg2H-0j- p_T^H -Low, gg2H-0j- p_T^H -High) plane. The SM prediction

is shown together with its theory uncertainty (filled ellipse). The VH parameter of interest is constrained to positive values

for vector bosons are defined as $\kappa_V = \kappa_W = \kappa_Z$ and $\kappa_F = \kappa_t = \kappa_b = \kappa_c = \kappa_\tau = \kappa_\mu$. It is assumed that there are no undetected or invisible Higgs boson decays. The observed likelihood contours in the κ_V - κ_F plane are shown in Fig. 12 (only the quadrant $\kappa_F > 0$ and $\kappa_V > 0$ is shown since this channel is not sensitive to the relative sign of the two coupling modifiers). The best-fit value is $\hat{\kappa}_V = 1.02 \pm 0.06$ and $\hat{\kappa}_F = 0.88 \pm 0.16$, with the correlation of -0.17 . The probability of compatibility with the Standard Model expectation is at the level of 75%.

10 Constraints on the tensor coupling structure in the EFT approach

To interpret the observed data in the framework of an effective field theory, an EFT signal model is built by parameterising the production cross-sections in each production bin of the Reduced Stage 1.1, as well as the branching ratio and the signal acceptances, as a function of the SMEFT Wilson coefficients introduced in Sect. 1.3. The constraints on the Wilson coefficients are then obtained from the simultaneous fit to the data in all reconstructed signal and sideband

event categories. Due to the statistical precision of the data sample, the constraints are always set on one or at most two of the Wilson coefficients at a time, while the values of the remaining coefficients are assumed to be equal to zero.

10.1 EFT signal model

The EFT parameterisation of the production cross-sections in each production bin of the Reduced Stage 1.1 is obtained from Eq. (1) using simulated BSM samples introduced in Sect. 3. The contribution from the $gg \rightarrow Z(\rightarrow \ell\ell)H$ process is taken from the SM simulation and assumed to scale with BSM parameters in the same way as the $qq \rightarrow Z(\rightarrow \ell\ell)H$ processes. As in the case of simplified template cross-section measurements, ttH and tH processes are combined into a single ttH production bin. The cut-off scale is set to $\Lambda = 1$ TeV. Only LO computation of QCD and SM electroweak processes is provided, with LO effective couplings for the SM Higgs boson to gluon and to photon vertices. An assumption is made that higher-order corrections, applied in a multiplicative way, are the same for both the SM and the BSM LO predictions and therefore no changes in the parameterisation are expected due to higher-order effects [171]. With the current amount of data, the constraints from the VBF, VH and ttH production modes on the relevant Wilson coefficients still allow a rather large range of parameter values in which the quadratic term (the last term in Eq. (1)) cannot be neglected even though its contribution is suppressed by Λ^4 . Such dimension-six quadratic terms are therefore included in the EFT parameterisation. Since the linear terms from dimension-eight operators are suppressed by the same factor, they could in general also give similar non-negligible contributions. Dimension-eight terms are currently not available in the SMEFT model and are thus not taken into account.

The branching ratio for the $H \rightarrow ZZ^* \rightarrow 4\ell$ decay is parameterised in terms of Wilson coefficients following Eq. (2). The partial and total decay widths are calculated in MADGRAPH5_aMC@NLO. The total decay width is calculated by taking into account the dominant Higgs boson decay modes: $\gamma\gamma$, $Z\gamma$, bb , gg , WW and ZZ . Other decay modes are not affected by the probed Wilson coefficients. Their contribution to the total decay width is therefore given by the corresponding SM predictions.

The selection criteria for the four-lepton Higgs boson candidates, in particular the requirements on the minimum invariant mass m_{34} of the subleading lepton pair, introduce an additional dependence of the signal acceptance on the BSM coupling parameters. The particle-level signal acceptance A , defined as the fraction of signal events satisfying the Higgs boson candidate selection criteria applied at particle-level, has therefore been simultaneously parameterised in terms of the three Wilson coefficients c_{HW} , c_{HB} and c_{HWB} ($c_{H\tilde{W}}$, $c_{H\tilde{B}}$ and $c_{H\tilde{W}\tilde{B}}$) assuming that the values of CP-odd (CP-

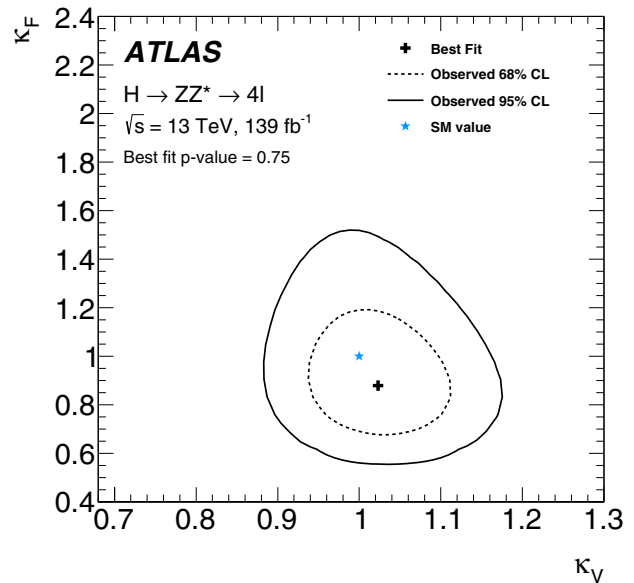


Fig. 12 Likelihood contours at 68% CL (dashed line) and 95% CL (solid line) in the κ_V - κ_F plane. The best fit to the data (solid cross) and the SM prediction (star) are also indicated

even) parameters vanish. The dependence of the acceptance on other EFT coupling parameters is shown to be negligible as these parameters have negligible or no impact on the $H \rightarrow ZZ^*$ decay. The acceptance correction relative to the SM prediction is described by a three-dimensional Lorentzian function with free acceptance parameters α_0 , α_1 , α_2 , β_i , δ_i , $\delta_{(i,j)}$ and $\delta_{(i,j,k)}$,

$$\frac{A(\vec{c})}{A_{SM}} = \alpha_0 + (\alpha_1)^2 \cdot \left[\alpha_2 + \sum_i \delta_i \cdot (c_i + \beta_i)^2 + \sum_{\substack{ij \\ i \neq j}} \delta_{(i,j)} \cdot c_i c_j + \sum_{\substack{i \neq j \neq k}} \delta_{(i,j,k)} \cdot c_i c_j c_k \right]^{-1}, \quad (4)$$

where indices i , j and k run over (HW, HB, HWB) in case of the acceptance correction for the set of CP-even parameters and over $(H\tilde{W}, H\tilde{B}, H\tilde{W}\tilde{B})$ in case of the CP-odd parameters. A common parameterisation is used for all production bins since the differences between production bins are shown to be negligible. In addition, the reconstructed event categorisation criteria imposed on the selected Higgs boson candidates and the classification in bins of multivariate NN discriminant values do not impact the acceptance parameterisation. The impact of reconstruction efficiencies on the parameterisation is also negligible, such that Eq. (4) also holds for the ratio $A(\vec{c})/A_{SM}$ of reconstruction-level acceptances defined in Sect. 8. The resulting acceptance parameterisation curves are shown in Fig. 13 for the cases in which all but one of the Wilson coefficients are set to zero. For all cases, the acceptance correction is equal to one at the SM point. In the case

of the c_{HW} and c_{HWB} Wilson coefficients, the acceptance corrections reach a maximum value slightly larger than one, leading to the shift of the maximum position from the SM point. This shift is compatible with the statistical accuracy of the fit and the impact of linear EFT terms which are not symmetric around the SM point.

The final parameterisation of signal yields relative to the SM prediction in each production bin of the Reduced Stage 1.1 is obtained as the product of the corresponding cross-section, branching ratio and acceptance parameterisations. The expected event yields normalised to the SM prediction are shown in Fig. 14 for each of the CP-even Wilson coefficients after setting all other coefficients to zero. Only production bins with the highest sensitivity to a given Wilson coefficient are shown. The impact of the quadratic terms in the EFT parameterisation can clearly be seen as a non-linear dependence on all but the c_{HG} Wilson coefficient. For comparison, the predictions without the acceptance corrections ($\sigma \cdot \mathcal{B}$), and without both the acceptance and branching ratio corrections (σ) are also shown. Both the acceptance and the branching ratio parameterisations have a strong impact on the sensitivity to different Wilson coefficients, especially for the c_{HW} , c_{HB} and c_{HWB} parameterisations in $gg2H$ production bins (Fig. 14a, b, c). Since these coefficients do not enter the ggF production vertex, the corresponding sensitivity is entirely driven by their impact on the decay and the acceptance of selected signal events. The acceptance corrections significantly degrade the sensitivity to the c_{HW} coefficient (see Fig. 14a). Additional sensitivity to this coefficient can be gained from the $qq2Hqq$ production bins as shown in Fig. 14d. The Wilson coefficients c_{HG} and c_{uH} , on the other hand, do not affect the acceptance since they are not present in the decay vertex (Fig. 14e, f). The coefficient c_{HG} still has a non-vanishing impact on the branching ratio through its contributions to the total decay width. Similar effects are also seen for the Wilson coefficients of CP-odd operators.

10.2 EFT interpretation results

The ratios of the expected signal yield for a chosen EFT parameter value to its SM prediction are shown in Fig. 15 in each production bin of the Reduced Stage 1.1, together with the corresponding measurement.

The EFT parameterisation of signal yields is implemented in the likelihood function of Eq. (3) using the BSM-dependent signal-strength parameters $\mu^p(\vec{c})$ for each given production bin p ,

$$\mu^p(\vec{c}) = \frac{\sigma^p(\vec{c})}{\sigma_{SM}} \cdot \frac{\mathcal{B}^{4\ell}(\vec{c})}{\mathcal{B}_{SM}^{4\ell}} \cdot \frac{A(\vec{c})}{A_{SM}}.$$

This is then fitted to the observed event yields. Default SM predictions at the highest available order are employed for

the cross-sections and branching ratios multiplying the signal strengths in the likelihood function. Modifications of background contributions due to EFT effects are not taken into account.

The fit results with only one Wilson coefficient fitted at a time are summarised in Fig. 16 and in Table 9. The results are in good agreement with the SM predictions. The measurements are dominated by the statistical uncertainty. In the case of the CP-odd coupling parameters, each fit gives two degenerate minima since the corresponding EFT parameterisation contains only quadratic terms which are not sensitive to the sign of the fitted parameter. The fit of the CP-even coupling parameter c_{uH} also results in two minima since the corresponding EFT parameterisation curve in the only sensitive ttH production bin crosses the expected SM cross-section value at two different values of the c_{uH} parameter (see Fig. 14f). The same is true also for the observed ttH cross-section. The small degeneracies for other CP-even coupling parameters are removed by the combination of several sensitive production bins.

The strongest constraint, driven mostly by the ggF reconstructed event categories, is obtained on the c_{HG} coefficient related to the CP-even Higgs boson interactions with gluons. The highest sensitivity to this parameter is reached by the measurements in the $gg2H-0j-p_T^H$ -Low and $gg2H-0j-p_T^H$ -High production bins due to the highest statistical precision. The sensitivity in the $gg2H-p_T^H$ -High production bin, which is designed to target the BSM physics effects, is limited due to the small number of events observed in the corresponding reconstructed event category. Additional sensitivity in this bin may be provided by the two-loop interactions which are not implemented in the current simulation of the ggH vertex. The constrained range is stringent enough for the linear approximation to hold, i.e. the quadratic terms in the signal parameterisation are small compared with the linear ones (see Fig. 14e). The constraint on the $c_{H\tilde{G}}$ parameter of the related CP-odd operator is worse by about a factor of three since the linear terms from CP-odd operators do not contribute to the total production cross-section. The constraints on the remaining EFT parameters are weaker, such that both the CP-even and CP-odd signals become dominated by the quadratic terms and are therefore comparable in size. The next-strongest constraints are obtained on the c_{HB} , c_{HWB} , c_{HW} , $c_{H\tilde{B}}$, $c_{H\tilde{W}B}$ and $c_{H\tilde{W}}$ coefficients that mostly affect the $H \rightarrow ZZ^*$ decays. Due to the larger number of events in the 0-jet reconstructed event categories, the corresponding $gg2H$ production bins provide the highest sensitivity to these decays. Additional smaller sensitivity is obtained from the production vertex of the VBF and VH production modes, with the dominant contribution from $qq2Hqq$ -VBF and $qq2Hqq$ -BSM bins. The latter one is designed to enhance the sensitivity to BSM physics. The $qq2Hqq$ production bins improve in particular the sensitivity to the c_{HW} and $c_{H\tilde{W}}$

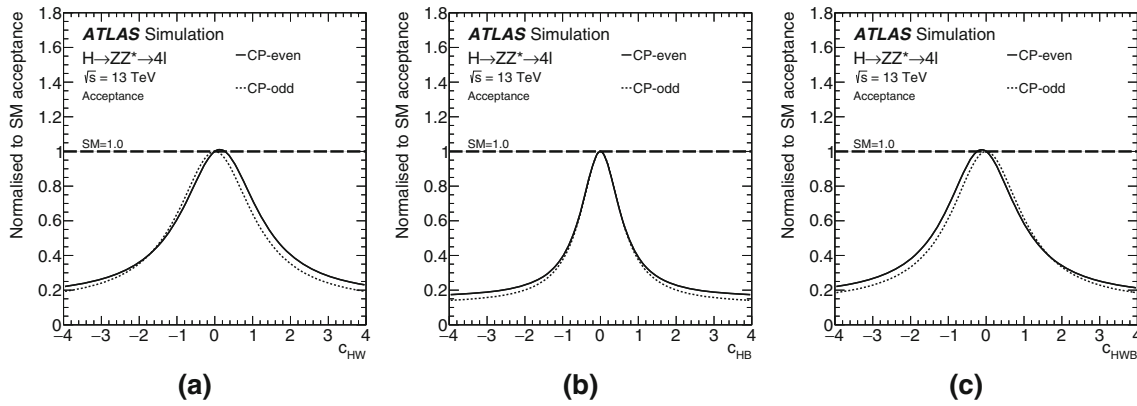


Fig. 13 The dependence of the signal acceptance normalised to the SM acceptance on the Wilson coefficients (a) c_{HW} and $c_{H\tilde{W}}$, (b) c_{HB} and $c_{H\tilde{B}}$, (c) c_{HWB} and $c_{H\tilde{W}B}$ after setting all other coefficients to zero

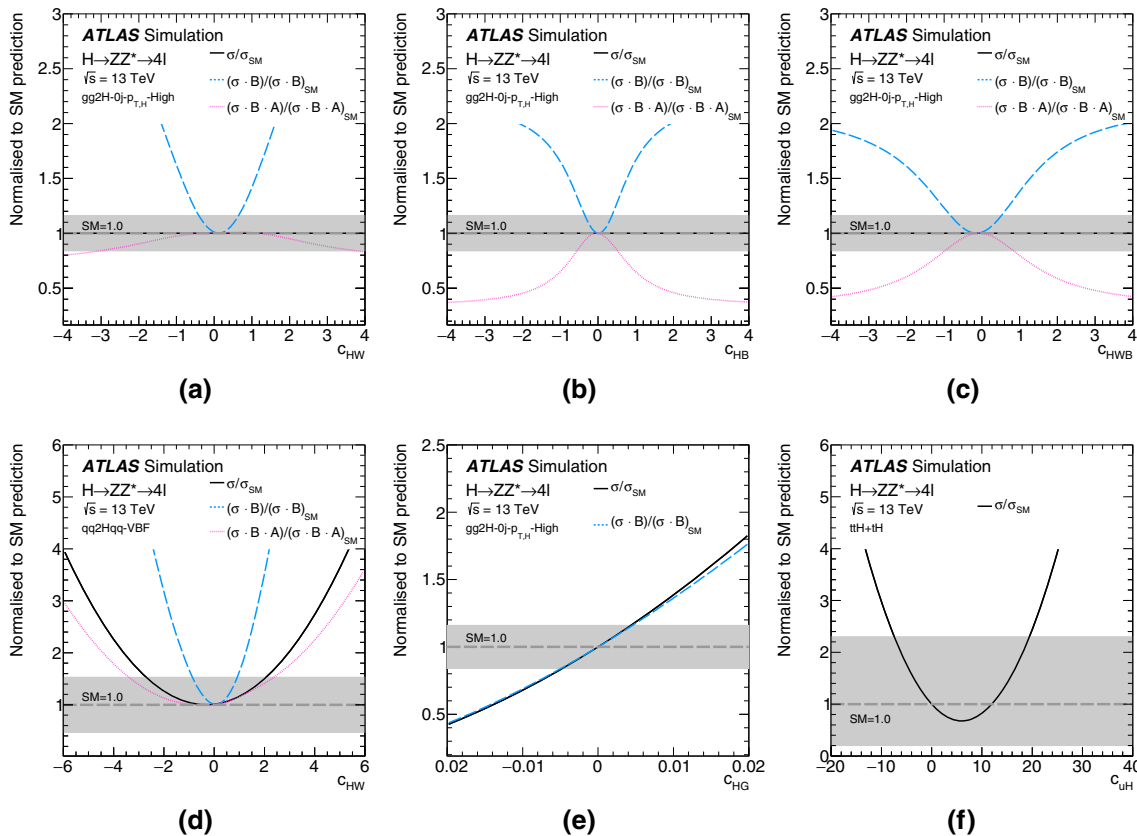


Fig. 14 The expected event yields ($\sigma \cdot B \cdot A$) relative to the SM prediction as a function of the Wilson coefficient (a) c_{HW} , (b) c_{HB} and (c) c_{HWB} in the $gg2H-0j-p_{T,H}^H$ -High production bin, (d) c_{HW} in the $qq2Hqq$ -VBF production bin, (e) c_{HG} in the $gg2H-0j-p_{T,H}^H$ -High production bin and (f) c_{uH} in the $t\bar{t}H$ production bin. The dependence on only one Wilson coefficient is shown on each plot while setting all others to zero. For comparison, the predictions are also shown for the parameterisation without the acceptance corrections ($\sigma \cdot B$) and for the production cross-section only (σ) without the acceptance and the

branching ratio corrections. The σ parameterisations in (a), (b) and (c) coincide with the SM expectation at 1 as the coefficients c_{HW} , c_{HB} and c_{HWB} are not present in the ggF production vertex. Since the acceptance does not depend on the c_{HG} and c_{uH} parameters, no corresponding ($\sigma \cdot B \cdot A$) expectation is shown in (e) and (f). Similarly, no ($\sigma \cdot B$) expectation is shown in (f), since the c_{uH} parameter has a negligible impact on the branching ratio. The bands indicate the expected precision of the cross-section measurement in a given production bin at the one standard deviation level

parameters that is otherwise significantly degraded by the acceptance corrections. Finally, looser constraints are set on

the top-Yukawa coupling parameters c_{uH} and $c_{\bar{u}H}$, driven by the measurements in the $t\bar{t}H$ production bin.

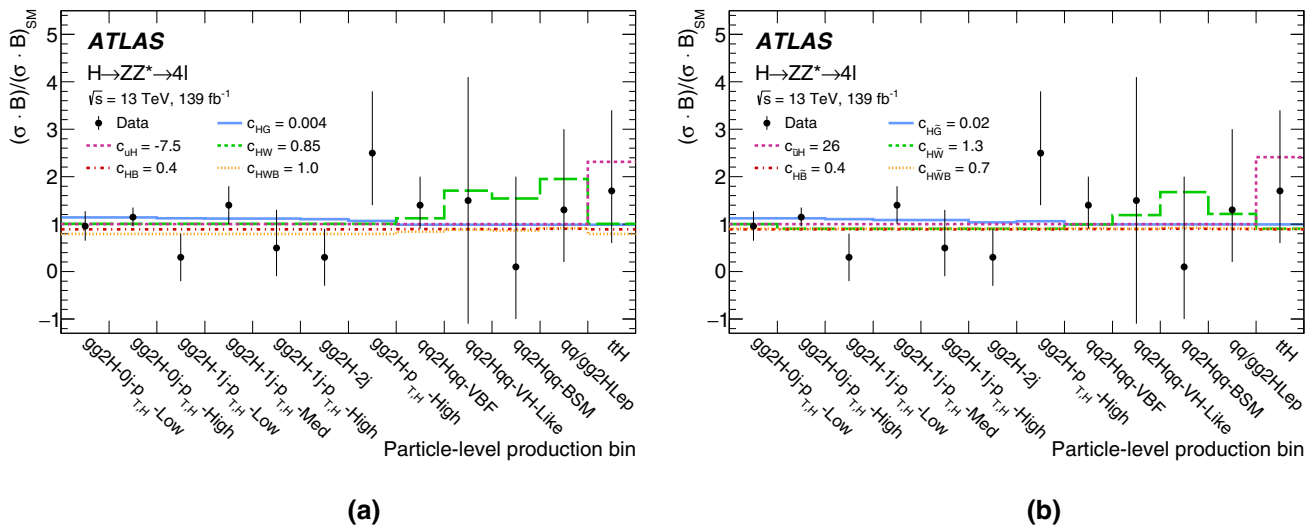


Fig. 15 The expected signal yield ratio for chosen (a) CP-even and (b) CP-odd EFT parameter values together with the corresponding cross-section measurement in each production bin of Reduced Stage 1.1. The

parameter values correspond approximately to the expected confidence intervals at the 68% CL obtained from the statistical interpretation of data

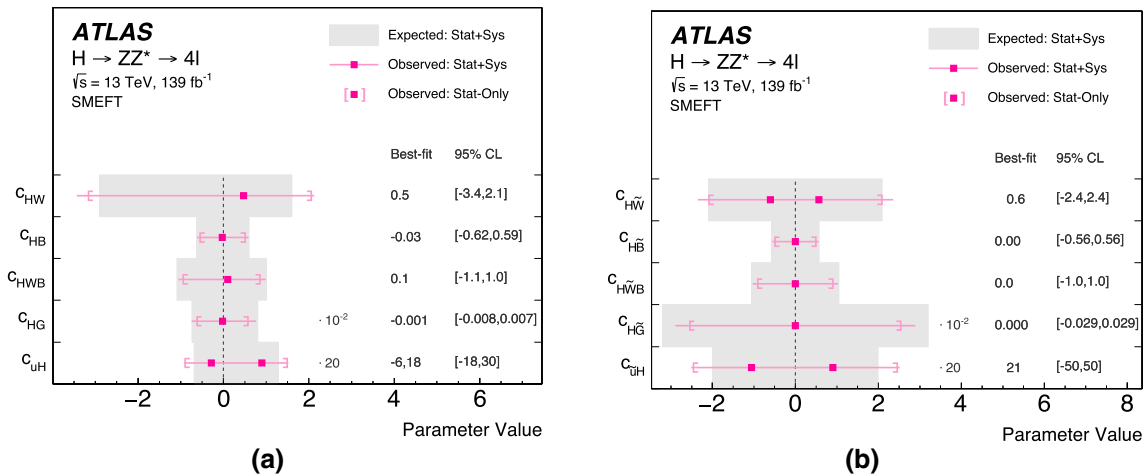


Fig. 16 The observed and expected values of SMEFT Wilson coefficients from (a) CP-even and (b) CP-odd operators obtained for an integrated luminosity of 139 fb^{-1} at $\sqrt{s} = 13 \text{ TeV}$. Only one Wilson coefficient is fitted at a time while all others are set to zero. The values

for the c_{HG} and $c_{H\tilde{G}}$ coefficients are scaled by a factor of 100, and for the c_{uH} and $c_{\tilde{u}H}$ coefficients by a factor of 0.05. The horizontal bands represent the expected measurement uncertainty

To explore possible correlations between different Wilson coefficients, the simultaneous fits are also performed on two Wilson coefficients at a time. The corresponding results are shown in Fig. 17 for several combinations of two CP-even EFT parameters and in Fig. 18 for the corresponding CP-odd operators. The best-fit values as well as the deviation from the SM prediction are shown in Table 10. Good agreement with the SM predictions is observed for all such possible combinations.

The anti-correlation between the c_{HW} and c_{HB} coefficients, as well as between $c_{H\tilde{W}}$ and $c_{H\tilde{B}}$, is driven by their impact on the signal acceptance. The non-ellipsoidal shape is caused by the acceptance correction, which degrades

the original branching ratio-driven sensitivity for increasing parameter values, in particular in the case of the c_{HW} ($c_{H\tilde{W}}$) coefficient. The sensitivity is, however, partially recouped by the VBF production vertex.

The ‘V’-shaped correlation between the c_{HG} and c_{HB} parameters is due to the interplay between the EFT parameterisation in the ggF production vertex and the parameterisation of the branching ratios and acceptances. The ggF production vertex provides the constraint on the c_{HG} parameter alone, independently of c_{HB} . Due to the decay vertex with its acceptance corrections, this constrained range is shifted upward with increasing values of c_{HB} . Close to the SM point, the constrained c_{HG} range remains approximately the same

Table 9 The expected and observed confidence intervals at 68% and 95% CL on the SMEFT Wilson coefficients for an integrated luminosity of 139 fb^{-1} at $\sqrt{s} = 13 \text{ TeV}$. Only one Wilson coefficient is fitted at a time while all others are set to zero

EFT coupling parameter	Expected		Observed		Best-fit value	Best-fit p -value
	68% CL	95% CL	68% CL	95% CL		
c_{HG}	$[-0.004, 0.004]$	$[-0.007, 0.008]$	$[-0.005, 0.003]$	$[-0.008, 0.007]$	-0.001	0.79
c_{uH}	$[-8, 20]$	$[-14, 26]$	$[-12, 6]$	$[-18, 30]$	$-6, 18$	0.50
c_{HW}	$[-1.6, 0.9]$	$[-2.9, 1.6]$	$[-1.5, 1.3]$	$[-3.4, 2.1]$	0.5	0.66
c_{HB}	$[-0.43, 0.38]$	$[-0.62, 0.60]$	$[-0.42, 0.37]$	$[-0.62, 0.59]$	-0.03	0.98
c_{HWB}	$[-0.75, 0.63]$	$[-1.09, 0.99]$	$[-0.71, 0.63]$	$[-1.06, 0.99]$	0.1	0.93
$c_{H\tilde{G}}$	$[-0.022, 0.022]$	$[-0.031, 0.031]$	$[-0.019, 0.019]$	$[-0.029, 0.029]$	0.000	1.00
$c_{\tilde{u}H}$	$[-26, 26]$	$[-40, 40]$	$[-37, 37]$	$[-50, 50]$	± 21	0.48
$c_{H\tilde{W}}$	$[-1.3, 1.3]$	$[-2.1, 2.1]$	$[-1.5, 1.5]$	$[-2.4, 2.4]$	± 0.6	0.84
$c_{H\tilde{B}}$	$[-0.39, 0.39]$	$[-0.57, 0.57]$	$[-0.37, 0.37]$	$[-0.56, 0.56]$	0.00	1.00
$c_{H\tilde{W}B}$	$[-0.71, 0.71]$	$[-1.05, 1.05]$	$[-0.69, 0.69]$	$[-1.03, 1.03]$	0.0	1.00

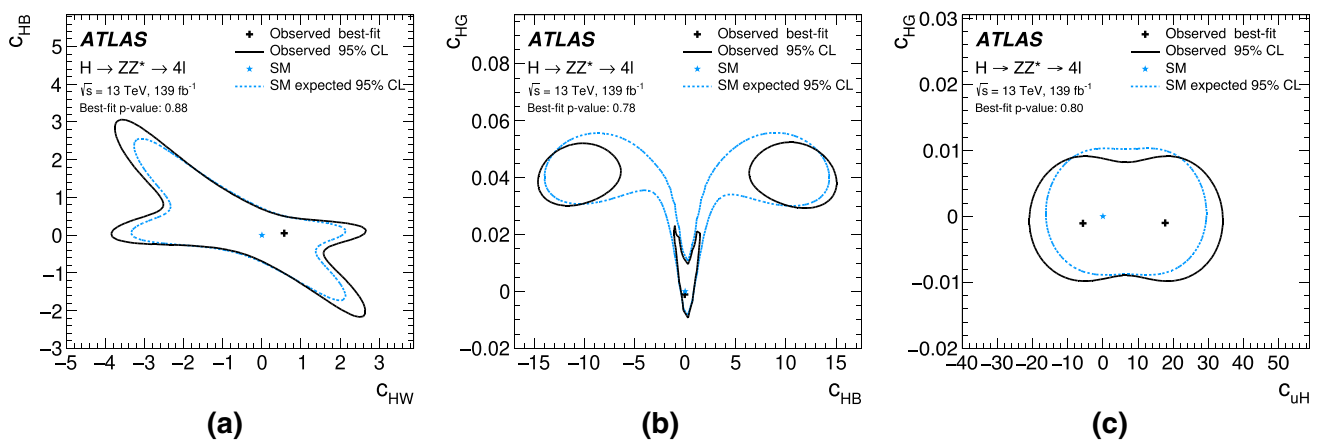


Fig. 17 Expected (dashed line) and observed (full line) 2D-fit likelihood curves at the 95% CL for the SMEFT Wilson coefficients of CP-even operators at an integrated luminosity of 139 fb^{-1} and

$\sqrt{s} = 13 \text{ TeV}$. The best fit to the data (solid cross) and the SM prediction (star) are also indicated. Except for the two fitted Wilson coefficients, all others are set to zero

as without the decay constraints. An additional constraint on c_{HB} is provided by the VBF production mode. Around the SM point, the c_{HB} constraints correspond approximately to those from the one-dimensional parameter fit. Additional sensitivity to intermediate values of the c_{HB} parameter is provided by the acceptance corrections, resulting in two additional allowed parameter regions that are disjoint from the region around the SM point. Similar arguments hold also for the CP-odd case with the $c_{H\tilde{G}}$ and $c_{H\tilde{B}}$ parameters. As opposed to the CP-even case, however, the likelihood contours are symmetric around the $c_{H\tilde{G}} = 0$ axis, since there are no linear terms contributing to the ggF production cross-section.

The correlation between the c_{HG} and c_{uH} ($c_{H\tilde{G}}$ and $c_{\tilde{u}H}$) parameters is introduced through the interference term in the ttH vertex. However, the impact of this term on the final result is negligible since the c_{HG} ($c_{H\tilde{G}}$) parameter is already constrained to very small values compared with c_{uH} ($c_{\tilde{u}H}$).

Therefore, the ttH production vertex mainly constrains the c_{uH} and $c_{\tilde{u}H}$ parameters, while the ggF vertex constrains only the other two. The acceptance correction has no impact on these results. The CP-odd parameter range is less constrained than the CP-even one due to the missing linear $c_{\tilde{u}H}$ terms in the cross-section parameterisation.

11 Conclusion

Higgs boson properties are studied in the four-lepton decay channel using 139 fb^{-1} of LHC proton–proton collision data at $\sqrt{s} = 13 \text{ TeV}$ collected by the ATLAS experiment. The Higgs boson candidate events are categorised into several topologies, providing sensitivity to different production modes in various regions of phase space. Additional multivariate discriminants are used to further improve the sensitivity in reconstructed event categories with a sufficiently

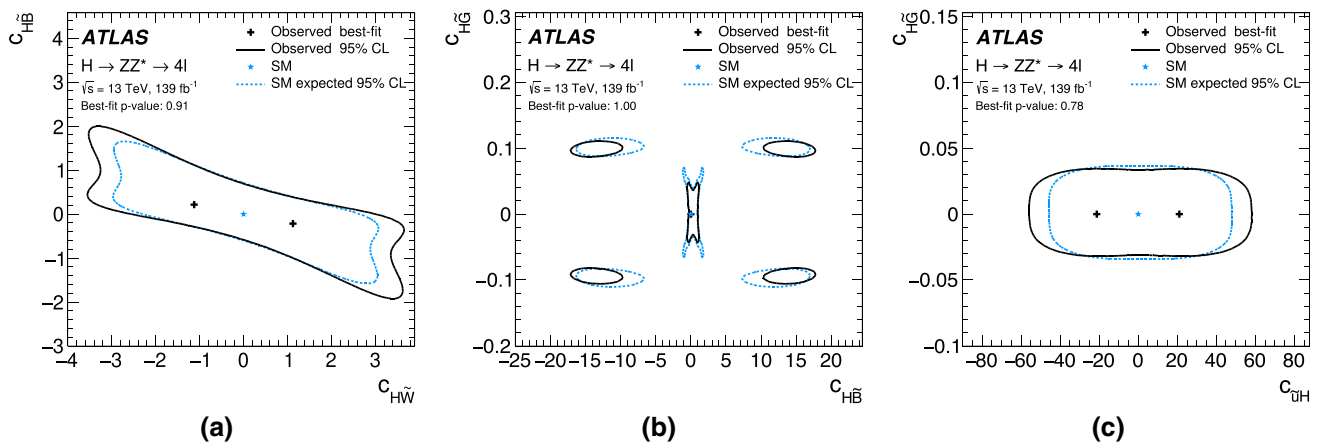


Fig. 18 Expected (dashed line) and observed (full line) 2D-fit likelihood curves at the 95% CL for the SMEFT Wilson coefficients of CP-odd operators at an integrated luminosity of 139 fb^{-1} and $\sqrt{s} = 13 \text{ TeV}$.

The best fit to the data (solid cross) and the SM prediction (star) are also indicated. Except for the two fitted Wilson coefficients, all others are set to zero

Table 10 The best-fit values and the corresponding deviation from the SM prediction obtained from the two-dimensional likelihood scans of the CP-odd BSM coupling parameters performed with 139 fb^{-1} of data

at a centre-of-mass energy of $\sqrt{s} = 13 \text{ TeV}$. The limits are computed using the confidence-level interval method. Except for the two fitted BSM coupling parameters, all others are set to zero

BSM coupling parameter	Observed best fit		Best-fit p-value
c_{HW}, c_{HB}	$\hat{c}_{HW} = 0.57$	$\hat{c}_{HB} = 0.05$	0.88
c_{HG}, c_{HB}	$\hat{c}_{HG} = -0.001$	$\hat{c}_{HB} = -0.04$	0.78
c_{HG}, c_{uH}	$\hat{c}_{HG} = -0.001$	$\hat{c}_{uH} = -5.7, 17.7$	0.80
$c_{H\tilde{W}}, c_{H\tilde{B}}$	$\hat{c}_{H\tilde{W}} = \pm 1.12$	$\hat{c}_{H\tilde{B}} = \mp 0.21$	0.91
$c_{H\tilde{G}}, c_{H\tilde{B}}$	$\hat{c}_{H\tilde{G}} = 0.00$	$\hat{c}_{H\tilde{B}} = 0.00$	1.00
$c_{H\tilde{G}}, c_{u\tilde{H}}$	$\hat{c}_{H\tilde{G}} = 0.000$	$\hat{c}_{u\tilde{H}} = \pm 21$	0.78

large number of events. The cross-section times branching ratio for $H \rightarrow ZZ^*$ decay measured in dedicated production bins are in good agreement with the SM predictions. The inclusive cross-section times branching ratio for $H \rightarrow ZZ^*$ decay in the Higgs boson rapidity range of $|y_H| < 2.5$ is measured to be $1.34 \pm 0.12 \text{ pb}$ compared with the SM prediction of $1.33 \pm 0.08 \text{ pb}$. Results are also interpreted within the κ -framework with coupling-strength modifiers κ_V and κ_F , showing compatibility with the SM. Based on the product of cross-section, branching ratio and acceptance measured in Reduced Stage-1.1 production bins of simplified template cross-sections, constraints are placed on possible CP-even and CP-odd BSM interactions of the Higgs boson to vector bosons, gluons and top quarks within an effective field theory framework in the $H \rightarrow ZZ^*$ decay. The data are found to be consistent with the SM hypothesis.

Acknowledgements We thank CERN for the very successful operation of the LHC, as well as the support staff from our institutions without whom ATLAS could not be operated efficiently.

We acknowledge the support of ANPCyT, Argentina; YerPhI, Armenia; ARC, Australia; BMWFW and FWF, Austria; ANAS, Azerbaijan; SSTC, Belarus; CNPq and FAPESP, Brazil; NSERC, NRC and CFI, Canada; CERN; CONICYT, Chile; CAS, MOST and NSFC, China; COLCIENCIAS, Colombia; MSMT CR, MPO CR and VSC CR, Czech Republic; DNRF and DNSRC, Denmark; IN2P3-CNRS and CEA-DRF/IRFU, France; SRNSFG, Georgia; BMBF, HGF and MPG, Germany; GSRT, Greece; RGC and Hong Kong SAR, China; ISF and Benozio Center, Israel; INFN, Italy; MEXT and JSPS, Japan; CNRST, Morocco; NWO, Netherlands; RCN, Norway; MNiSW and NCN, Poland; FCT, Portugal; MNE/IFA, Romania; MES of Russia and NRC KI, Russia Federation; JINR; MESTD, Serbia; MSSR, Slovakia; ARRS and MIZŠ, Slovenia; DST/NRF, South Africa; MINECO, Spain; SRC and Wallenberg Foundation, Sweden; SERI, SNSF and Cantons of Bern and Geneva, Switzerland; MOST, Taiwan; TAIEK, Turkey; STFC, United Kingdom; DOE and NSF, United States of America. In addition, individual groups and members have received support from BCKDF, CANARIE, Compute Canada and CRC, Canada; ERC, ERDF, Horizon 2020, Marie Skłodowska-Curie Actions and COST, European Union; Investissements d’Avenir Labex, Investissements d’Avenir Idex and ANR, France; DFG and AvH Foundation, Germany; Herakleitos, Thales and Aristeia programmes co-financed by EU-ESF and the Greek NSRF, Greece; BSF-NSF and GIF, Israel; CERCA Programme Generalitat de Catalunya and PROMETEO Programme Generalitat Valen-

ciana, Spain; Göran Gustafssons Stiftelse, Sweden; The Royal Society and Leverhulme Trust, United Kingdom.

The crucial computing support from all WLCG partners is acknowledged gratefully, in particular from CERN, the ATLAS Tier-1 facilities at TRIUMF (Canada), NDGF (Denmark, Norway, Sweden), CC-IN2P3 (France), KIT/GridKA (Germany), INFN-CNAF (Italy), NL-T1 (Netherlands), PIC (Spain), ASGC (Taiwan), RAL (UK) and BNL (USA), the Tier-2 facilities worldwide and large non-WLCG resource providers. Major contributors of computing resources are listed in Ref. [172].

Data Availability Statement This manuscript has no associated data or the data will not be deposited. [Authors' comment: All ATLAS scientific output is published in journals, and preliminary results are made available in Conference Notes. All are openly available, without restriction on use by external parties beyond copyright law and the standard conditions agreed by CERN. Data associated with journal publications are also made available: tables and data from plots (e.g. cross section values, likelihood profiles, selection efficiencies, cross section limits, ...) are stored in appropriate repositories such as HEPDATA (<http://hepdata.cedar.ac.uk/>). ATLAS also strives to make additional material related to the paper available that allows a reinterpretation of the data in the context of new theoretical models. For example, an extended encapsulation of the analysis is often provided for measurements in the framework of RIVET (<http://rivet.hepforge.org/>)". This information is taken from the ATLAS Data Access Policy, which is a public document that can be downloaded from <http://opendata.cern.ch/record/413> [opendata.cern.ch].]

Open Access This article is licensed under a Creative Commons Attribution 4.0 International License, which permits use, sharing, adaptation, distribution and reproduction in any medium or format, as long as you give appropriate credit to the original author(s) and the source, provide a link to the Creative Commons licence, and indicate if changes were made. The images or other third party material in this article are included in the article's Creative Commons licence, unless indicated otherwise in a credit line to the material. If material is not included in the article's Creative Commons licence and your intended use is not permitted by statutory regulation or exceeds the permitted use, you will need to obtain permission directly from the copyright holder. To view a copy of this licence, visit <http://creativecommons.org/licenses/by/4.0/>. Funded by SCOAP³.

References

1. ATLAS Collaboration, Observation of a new particle in the search for the Standard Model Higgs boson with the ATLAS detector at the LHC, Phys. Lett. B **716**, 1 (2012). <https://doi.org/10.1016/j.physletb.2012.08.020>. arXiv:1207.7214 [hep-ex]
2. CMS Collaboration, Observation of a new boson at a mass of 125 GeV with the CMS experiment at the LHC. Phys. Lett. B **716**, 30 (2012). <https://doi.org/10.1016/j.physletb.2012.08.021>. arXiv:1207.7235 [hep-ex]
3. F. Englert, R. Brout, Broken symmetry and the mass of gauge vector mesons. Phys. Rev. Lett. **13**, 321 (1964). <https://doi.org/10.1103/PhysRevLett.13.321>
4. P.W. Higgs, Broken symmetries and the masses of gauge bosons. Phys. Rev. Lett. **13**, 508 (1964). <https://doi.org/10.1103/PhysRevLett.13.508>
5. G. Guralnik, C. Hagen, T. Kibble, Global conservation laws and massless particles. Phys. Rev. Lett. **13**, 585 (1964). <https://doi.org/10.1103/PhysRevLett.13.585>
6. CMS Collaboration, Study of the Mass and Spin-Parity of the Higgs Boson Candidate Via Its Decays to Z Boson Pairs. Phys. Rev. Lett. **110**, 081803 (2013). <https://doi.org/10.1103/PhysRevLett.110.081803>. arXiv:1212.6639 [hep-ex]
7. ATLAS Collaboration, Evidence for the spin-0 nature of the Higgs boson using ATLAS data, Phys. Lett. B **726**, 120 (2013). <https://doi.org/10.1016/j.physletb.2013.08.026>. arXiv:1307.1432 [hep-ex]
8. ATLAS Collaboration, Study of the spin and parity of the Higgs boson in diboson decays with the ATLAS detector, Eur. Phys. J. C **75**, 476 (2015). <https://doi.org/10.1140/epjc/s10052-015-3685-1>. arXiv:1506.05669 [hep-ex], Erratum: Eur. Phys. J. C **76** (2016) 152
9. ATLAS Collaboration, Measurements of the Higgs boson inclusive and differential fiducial cross sections in the 4ℓ decay channel at $\sqrt{s} = 13$ TeV, CERN-EP-2020-035 (2020). <https://doi.org/10.1140/epjc/s10052-020-8223-0>
10. ATLAS and CMS Collaborations, Measurements of the Higgs boson production and decay rates and constraints on its couplings from a combined ATLAS and CMS analysis of the LHC pp collision data at $\sqrt{s} = 7$ and 8 TeV. JHEP **08**, 045 (2016). [https://doi.org/10.1007/JHEP08\(2016\)045](https://doi.org/10.1007/JHEP08(2016)045). arXiv:1606.02266 [hep-ex]
11. CMS Collaboration, Combined measurements of Higgs boson couplings in proton-proton collisions at $\sqrt{s} = 13$ TeV. Eur. Phys. J. C **79**, 421 (2019). <https://doi.org/10.1140/epjc/s10052-019-6909-y>. arXiv:1809.10733 [hep-ex]
12. ATLAS Collaboration, Combined measurements of Higgs boson production and decay using up to 80 fb⁻¹ of proton-proton collision data at $\sqrt{s} = 13$ TeV collected with the ATLAS experiment, Phys. Rev. D **101**, 012002 (2020). <https://doi.org/10.1103/PhysRevD.101.012002>. arXiv:1909.02845 [hep-ex]
13. CMS Collaboration, Constraints on the spin-parity and anomalous HVV couplings of the Higgs boson in proton collisions at 7 and 8 TeV. Phys. Rev. D **92**, 012004 (2015). <https://doi.org/10.1103/PhysRevD.92.012004>. arXiv:1411.3441 [hep-ex]
14. CMS Collaboration, Combined search for anomalous pseudoscalar HVV couplings in $VH(H \rightarrow b\bar{b})$ production and $H \rightarrow VV$ decay. Phys. Lett. B **759**, 672 (2016). <https://doi.org/10.1016/j.physletb.2016.06.004>. arXiv:1602.04305 [hep-ex]
15. ATLAS Collaboration, Test of CP invariance in vector-boson fusion production of the Higgs boson using the optimal observable method in the ditau decay channel with the ATLAS detector, Eur. Phys. J. C **76**, 658 (2016). <https://doi.org/10.1140/epjc/s10052-016-4499-5>. arXiv:1602.04516 [hep-ex]
16. CMS Collaboration, Constraints on anomalous Higgs boson couplings using production and decay information in the four-lepton final state. Phys. Lett. B **775**, 1 (2017). <https://doi.org/10.1016/j.physletb.2017.10.021>. arXiv:1707.00541 [hep-ex]
17. ATLAS Collaboration, Measurement of the Higgs boson coupling properties in the $H \rightarrow ZZ^* \rightarrow 4\ell$ decay channel at $\sqrt{s} = 13$ TeV with the ATLAS detector, JHEP **03**, 095 (2018), [https://doi.org/10.1007/JHEP03\(2018\)095](https://doi.org/10.1007/JHEP03(2018)095). arXiv:1712.02304 [hep-ex]
18. ATLAS Collaboration, Measurements of Higgs boson properties in the diphoton decay channel with 36 fb⁻¹ of pp collision data at $\sqrt{s} = 13$ TeV with the ATLAS detector, Phys. Rev. D **98**, 052005 (2018). <https://doi.org/10.1103/PhysRevD.98.052005>. arXiv:1802.04146 [hep-ex]
19. CMS Collaboration, Measurements of the Higgs boson width and anomalous HVV couplings from on-shell and off-shell production in the four-lepton final state. Phys. Rev. D **99**, 112003 (2019). <https://doi.org/10.1103/PhysRevD.99.112003>. arXiv:1901.00174 [hep-ex]
20. CMS Collaboration, Constraints on anomalous HVV couplings from the production of Higgs bosons decaying to τ lepton pairs. Phys. Rev. D **100**, 112002 (2019). <https://doi.org/10.1103/PhysRevD.100.112002>. arXiv:1903.06973 [hep-ex]

21. LHC Higgs Cross Section Working Group, S. Heinemeyer et al., Handbook of LHC higgs cross sections: 3. Higgs Properties, CERN-2013-004 (CERN, Geneva, 2013), 10.5170/CERN-2013-004. [arXiv:1307.1347](https://arxiv.org/abs/1307.1347) [hep-ph]
22. ATLAS Collaboration, Jet reconstruction and performance using particle flow with the ATLAS Detector, *Eur. Phys. J. C* **77**, 466 (2017). <https://doi.org/10.1140/epjc/s10052-017-5031-2>. [arXiv:1703.10485](https://arxiv.org/abs/1703.10485) [hep-ex]
23. J. Bendavid et al., Les Houches 2017: Physics at TeV colliders standard model working group report, (2018), [arXiv:1803.07977](https://arxiv.org/abs/1803.07977) [hep-ph]
24. LHC Higgs Cross Section Working Group, D. de Florian et al., Handbook of LHC Higgs Cross Sections: 4. Deciphering the nature of the Higgs sector, CERN-2017-002-M (CERN, Geneva, 2016), <https://doi.org/10.23731/CYRM-2017-002>. [arXiv:1610.07922](https://arxiv.org/abs/1610.07922) [hep-ph]
25. N. Berger et al., Simplified template cross sections - Stage 1.1 (2019). [arXiv:1906.02754](https://arxiv.org/abs/1906.02754) [hep-ph]
26. M. Cacciari, G.P. Salam, G. Soyez, The anti- k_r jet clustering algorithm. *JHEP* **04**, 063 (2008). <https://doi.org/10.1088/1126-6708/2008/04/063>. [arXiv:0802.1189](https://arxiv.org/abs/0802.1189) [hep-ph]
27. M. Cacciari, G.P. Salam, G. Soyez, FastJet user manual. *Eur. Phys. J. C* **72**, 1896 (2012). <https://doi.org/10.1140/epjc/s10052-012-1896-2>. [arXiv:1111.6097](https://arxiv.org/abs/1111.6097) [hep-ph]
28. C. Hays, A. Martin, V. Sanz, J. Setford, On the impact of dimension-eight SMEFT operators on Higgs measurements. *JHEP* **02**, 123 (2019). [https://doi.org/10.1007/JHEP02\(2019\)123](https://doi.org/10.1007/JHEP02(2019)123). [arXiv:1808.00442](https://arxiv.org/abs/1808.00442) [hep-ph]
29. I. Brivio, Y. Jiang, M. Trott, The SMEFTsim package, theory and tools. *JHEP* **12**, 070 (2017). [https://doi.org/10.1007/JHEP12\(2017\)070](https://doi.org/10.1007/JHEP12(2017)070). [arXiv:1709.06492](https://arxiv.org/abs/1709.06492) [hep-ph]
30. B. Grzadkowski, M. Iskrzynski, M. Misiak, J. Rosiek, Dimension-six terms in the Standard Model Lagrangian. *JHEP* **10**, 085 (2010). [https://doi.org/10.1007/JHEP10\(2010\)085](https://doi.org/10.1007/JHEP10(2010)085). [arXiv:1008.4884](https://arxiv.org/abs/1008.4884) [hep-ph]
31. C. Hays, V. Sanz Gonzalez and G. Zemaityte, Constraining EFT parameters using simplified template cross sections, (2019), <https://cds.cern.ch/record/2673969>
32. ATLAS Collaboration, The ATLAS Experiment at the CERN Large Hadron Collider. *JINST* **3**, S08003 (2008). <https://doi.org/10.1088/1748-0221/3/08/S08003>
33. ATLAS Collaboration, ATLAS Insertable B-Layer Technical Design Report, ATLAS-TDR-19, 2010, <https://cds.cern.ch/record/1291633>, Addendum: ATLAS-TDR-19-ADD-1, 2012, <https://cds.cern.ch/record/1451888>
34. B. Abbott et al., Production and integration of the ATLAS Insertable B-Layer. *JINST* **13**, T05008 (2018). <https://doi.org/10.1088/1748-0221/13/05/T05008>. [arXiv:1803.00844](https://arxiv.org/abs/1803.00844) [physics.ins-det]
35. ATLAS Collaboration, Performance of the ATLAS trigger system in. *Eur. Phys. J. C* **77**(2017), 317 (2015). <https://doi.org/10.1140/epjc/s10052-017-4852-3>. [arXiv:1611.09661](https://arxiv.org/abs/1611.09661) [hep-ex]
36. ATLAS Collaboration, ATLAS data quality operations and performance for 2015-2018 data-taking. *JINST* **15**, P04003 (2020), <https://doi.org/10.1088/1748-0221/15/04/P04003>. [arXiv:1911.04632](https://arxiv.org/abs/1911.04632) [physics.ins-det]
37. S. Alioli, P. Nason, C. Oleari, E. Re, A general framework for implementing NLO calculations in shower Monte Carlo programs: the POWHEG BOX. *JHEP* **06**, 043 (2010). [https://doi.org/10.1007/JHEP06\(2010\)043](https://doi.org/10.1007/JHEP06(2010)043). [arXiv:1002.2581](https://arxiv.org/abs/1002.2581) [hep-ph]
38. S. Frixione, P. Nason, C. Oleari, Matching NLO QCD computations with parton shower simulations: the POWHEG method. *JHEP* **11**, 070 (2007). <https://doi.org/10.1088/1126-6708/2007/11/070>. [arXiv:0709.2092](https://arxiv.org/abs/0709.2092) [hep-ph]
39. P. Nason, A new method for combining NLO QCD with shower Monte Carlo algorithms. *JHEP* **11**, 040 (2004). <https://doi.org/10.1088/1126-6708/2004/11/040>. [arXiv:hep-ph/0409146](https://arxiv.org/abs/hep-ph/0409146) [hep-ph]
40. J. Butterworth et al., PDF4LHC recommendations for LHC Run II. *J. Phys. G* **43**, 023001 (2016). <https://doi.org/10.1088/0954-3899/43/2/023001>. [arXiv:1510.03865](https://arxiv.org/abs/1510.03865) [hep-ph]
41. K. Hamilton, P. Nason, G. Zanderighi, MINLO: multi-scale improved NLO. *JHEP* **10**, 155 (2012). [https://doi.org/10.1007/JHEP10\(2012\)155](https://doi.org/10.1007/JHEP10(2012)155). [arXiv:1206.3572](https://arxiv.org/abs/1206.3572) [hep-ph]
42. J.M. Campbell et al., NLO Higgs boson production plus one and two jets using the POWHEG BOX, MadGraph4 and MCFM. *JHEP* **07**, 092 (2012). [https://doi.org/10.1007/JHEP07\(2012\)092](https://doi.org/10.1007/JHEP07(2012)092). [arXiv:1202.5475](https://arxiv.org/abs/1202.5475) [hep-ph]
43. K. Hamilton, P. Nason, C. Oleari, G. Zanderighi, Merging $H/W/Z + 0$ and 1 jet at NLO with no merging scale: a path to parton shower + NNLO matching. *JHEP* **05**, 082 (2013). [https://doi.org/10.1007/JHEP05\(2013\)082](https://doi.org/10.1007/JHEP05(2013)082). [arXiv:1212.4504](https://arxiv.org/abs/1212.4504) [hep-ph]
44. E. Bagnaschi, G. Degrandi, P. Slavich, A. Vicini, Higgs production via gluon fusion in the POWHEG approach in the SM and in the MSSM. *JHEP* **02**, 088 (2012). [https://doi.org/10.1007/JHEP02\(2012\)088](https://doi.org/10.1007/JHEP02(2012)088). [arXiv:1111.2854](https://arxiv.org/abs/1111.2854) [hep-ph]
45. K. Hamilton, P. Nason, E. Re, G. Zanderighi, NNLOPS simulation of Higgs boson production. *JHEP* **10**, 222 (2013). [https://doi.org/10.1007/JHEP10\(2013\)222](https://doi.org/10.1007/JHEP10(2013)222). [arXiv:1309.0017](https://arxiv.org/abs/1309.0017) [hep-ph]
46. K. Hamilton, P. Nason, G. Zanderighi, Finite quark-mass effects in the NNLOPS POWHEG + MiNLO Higgs generator. *JHEP* **05**, 140 (2015). [https://doi.org/10.1007/JHEP05\(2015\)140](https://doi.org/10.1007/JHEP05(2015)140). [arXiv:1501.04637](https://arxiv.org/abs/1501.04637) [hep-ph]
47. S. Catani, M. Grazzini, Next-to-next-to-leading-order subtraction formalism in Hadron collisions and its application to Higgs-Boson Production at the Large Hadron Collider. *Phys. Rev. Lett.* **98**, 222002 (2007). <https://doi.org/10.1103/PhysRevLett.98.222002>. [arXiv:hep-ph/0703012](https://arxiv.org/abs/hep-ph/0703012) [hep-ph]
48. M. Grazzini, NNLO predictions for the Higgs boson signal in the $H \rightarrow WW \rightarrow \ell\nu\ell\nu$ and $H \rightarrow ZZ \rightarrow 4\ell$ decay channels. *JHEP* **02**, 043 (2008). <https://doi.org/10.1088/1126-6708/2008/02/043>. [arXiv:0801.3232](https://arxiv.org/abs/0801.3232) [hep-ph]
49. G. Bozzi, S. Catani, D. de Florian, M. Grazzini, Transverse-momentum resummation and the spectrum of the Higgs boson at the LHC. *Nucl. Phys. B* **737**, 73 (2006). <https://doi.org/10.1016/j.nuclphysb.2005.12.022>. [arXiv:hep-ph/0508068](https://arxiv.org/abs/hep-ph/0508068) [hep-ph]
50. D. de Florian, G. Ferrera, M. Grazzini, D. Tommasini, Transverse-momentum resummation: Higgs boson production at the Tevatron and the LHC. *JHEP* **11**, 064 (2011). [https://doi.org/10.1007/JHEP11\(2011\)064](https://doi.org/10.1007/JHEP11(2011)064). [arXiv:1109.2109](https://arxiv.org/abs/1109.2109) [hep-ph]
51. P. Nason, C. Oleari, NLO Higgs boson production via vector-boson fusion matched with shower in POWHEG. *JHEP* **02**, 037 (2010). [https://doi.org/10.1007/JHEP02\(2010\)037](https://doi.org/10.1007/JHEP02(2010)037). [arXiv:0911.5299](https://arxiv.org/abs/0911.5299) [hep-ph]
52. G. Luisoni, P. Nason, C. Oleari, F. Tramontano, $HW^\pm/HZ + 0$ and 1 jet at NLO with the POWHEG BOX interfaced to GoSam and their merging within MiNLO. *JHEP* **10**, 083 (2013). [https://doi.org/10.1007/JHEP10\(2013\)083](https://doi.org/10.1007/JHEP10(2013)083). [arXiv:1306.2542](https://arxiv.org/abs/1306.2542) [hep-ph]
53. H.B. Hartanto, B. Jager, L. Reina, D. Wackerroth, Higgs boson production in association with top quarks in the POWHEG BOX. *Phys. Rev. D* **91**, 094003 (2015). <https://doi.org/10.1103/PhysRevD.91.094003>. [arXiv:1501.04498](https://arxiv.org/abs/1501.04498) [hep-ph]
54. G. Cullen et al., Automated one-loop calculations with GoSam. *Eur. Phys. J. C* **72**, 1889 (2012). <https://doi.org/10.1140/epjc/s10052-012-1889-1>. [arXiv:1111.2034](https://arxiv.org/abs/1111.2034) [hep-ph]
55. J. Alwall et al., The automated computation of tree-level and next-to-leading order differential cross sections, and their matching to parton shower simulations. *JHEP* **07**, 079 (2014). [https://doi.org/10.1007/JHEP07\(2014\)079](https://doi.org/10.1007/JHEP07(2014)079). [arXiv:1405.0301](https://arxiv.org/abs/1405.0301) [hep-ph]

56. M. Wiesemann et al., Higgs production in association with bottom quarks. *JHEP* **02**, 132 (2015). [https://doi.org/10.1007/JHEP02\(2015\)132](https://doi.org/10.1007/JHEP02(2015)132). arXiv:1409.5301 [hep-ph]
57. H.-L. Lai et al., New parton distributions for collider physics. *Phys. Rev. D* **82**, 074024 (2010). <https://doi.org/10.1103/PhysRevD.82.074024>. arXiv:1007.2241 [hep-ph]
58. F. Demartin, F. Maltoni, K. Mawatari, M. Zaro, Higgs production in association with a single top quark at the LHC. *Eur. Phys. J. C* **75**, 267 (2015). <https://doi.org/10.1140/epjc/s10052-015-3475-9>. arXiv:1504.00611 [hep-ph]
59. F. Demartin, B. Maier, F. Maltoni, K. Mawatari, M. Zaro, tWH associated production at the LHC. *Eur. Phys. J. C* **77**, 34 (2017). <https://doi.org/10.1140/epjc/s10052-017-4601-7>. arXiv:1607.05862 [hep-ph]
60. R.D. Ball et al., Parton distributions for the LHC run II. *JHEP* **04**, 040 (2015). [https://doi.org/10.1007/JHEP04\(2015\)040](https://doi.org/10.1007/JHEP04(2015)040). arXiv:1410.8849 [hep-ph]
61. T. Sjöstrand, S. Mrenna, P.Z. Skands, A brief introduction to PYTHIA 8.1. *Comput. Phys. Commun.* **178**, 852 (2008). <https://doi.org/10.1016/j.cpc.2008.01.036>. arXiv:0710.3820 [hep-ph]
62. D.J. Lange, The EvtGen particle decay simulation package. *Nucl. Instrum. Meth. A* **462**, 152 (2001). [https://doi.org/10.1016/S0168-9002\(01\)00089-4](https://doi.org/10.1016/S0168-9002(01)00089-4)
63. ATLAS Collaboration, Measurement of the Z/γ^* boson transverse momentum distribution in pp collisions at $\sqrt{s} = 7$ TeV with the ATLAS detector. *JHEP* **09**, 145 (2014). [https://doi.org/10.1007/JHEP09\(2014\)145](https://doi.org/10.1007/JHEP09(2014)145). arXiv:1406.3660 [hep-ex]
64. ATLAS Collaboration, ATLAS Pythia 8 tunes to 7 TeV data, ATL-PHYS-PUB-2014-021, (2014), <https://cds.cern.ch/record/1966419>
65. R. Frederix, S. Frixione, Merging meets matching in MC@NLO. *JHEP* **12**, 061 (2012). [https://doi.org/10.1007/JHEP12\(2012\)061](https://doi.org/10.1007/JHEP12(2012)061). arXiv:1209.6215 [hep-ph]
66. LHC Higgs Cross Section Working Group, S. Dittmaier et al., Handbook of LHC higgs cross sections: 1. Inclusive observables, CERN-2011-002 (CERN, Geneva, 2011), <https://doi.org/10.5170/CERN-2011-002>. arXiv:1101.0593 [hep-ph]
67. LHC Higgs Cross Section Working Group, S. Dittmaier et al., Handbook of LHC Higgs Cross Sections: 2. Differential Distributions, CERN-2012-002 (CERN, Geneva, 2012), <https://doi.org/10.5170/CERN-2012-002>. arXiv:1201.3084 [hep-ph]
68. A. Djouadi, J. Kalinowski, M. Spira, HDECAY: a program for Higgs boson decays in the Standard Model and its supersymmetric extension. *Comput. Phys. Commun.* **108**, 56 (1998). [https://doi.org/10.1016/S0010-4655\(97\)00123-9](https://doi.org/10.1016/S0010-4655(97)00123-9). arXiv:hep-ph/9704448
69. A. Djouadi, M.M. Mühlleitner, M. Spira, Decays of supersymmetric particles: the program SUSY-HIT (SUSpect-Sdecay-Interface). *Acta Phys. Polon. B* **38**, 635 (2007). arXiv:hep-ph/0609292
70. S. Dulat et al., New parton distribution functions from a global analysis of quantum chromodynamics. *Phys. Rev. D* **93**, 033006 (2016). <https://doi.org/10.1103/PhysRevD.93.033006>. arXiv:1506.07443 [hep-ph]
71. L.A. Harland-Lang, A.D. Martin, P. Motylinski, R.S. Thorne, Parton distributions in the LHC era: MMHT 2014 PDFs. *Eur. Phys. J. C* **75**, 204 (2015). <https://doi.org/10.1140/epjc/s10052-015-3397-6>. arXiv:1412.3989 [hep-ph]
72. U. Aglietti, R. Bonciani, G. Degrossi, A. Vicini, Two-loop light fermion contribution to Higgs production and decays. *Phys. Lett. B* **595**, 432 (2004). <https://doi.org/10.1016/j.physletb.2004.06.063>. arXiv:hep-ph/0404071 [hep-ph]
73. M. Bonetti, K. Melnikov and L. Tancredi, Higher order corrections to mixed QCD-EW contributions to Higgs boson production in gluon fusion, *Phys. Rev. D* **97**, 056017 (2018). <https://doi.org/10.1103/physrevd.97.056017>. arXiv:1801.10403 [hep-ph], [Erratum: *Phys. Rev. D* **97** (2018) 099906]
74. S. Actis, G. Passarino, C. Sturm, S. Uccirati, NNLO computational techniques: the cases $H \rightarrow \gamma\gamma$ and $H \rightarrow gg$. *Nucl. Phys. B* **811**, 182 (2009). <https://doi.org/10.1016/j.nuclphysb.2008.11.024>. arXiv:0809.3667 [hep-ph]
75. S. Actis, G. Passarino, C. Sturm, S. Uccirati, NLO electroweak corrections to Higgs boson production at hadron colliders. *Phys. Lett. B* **670**, 12 (2008). <https://doi.org/10.1016/j.physletb.2008.10.018>. arXiv:0809.1301 [hep-ph]
76. A. Pak, M. Rogal, M. Steinhauser, Finite top quark mass effects in NNLO Higgs boson production at LHC. *JHEP* **02**, 025 (2010). [https://doi.org/10.1007/JHEP02\(2010\)025](https://doi.org/10.1007/JHEP02(2010)025). arXiv:0911.4662 [hep-ph]
77. R.V. Harlander, H. Mantler, S. Marzani, K.J. Ozeren, Higgs production in gluon fusion at next-to-next-to-leading order QCD for finite top mass. *Eur. Phys. J. C* **66**, 359 (2010). <https://doi.org/10.1140/epjc/s10052-010-1258-x>. arXiv:0912.2104 [hep-ph]
78. R.V. Harlander, K.J. Ozeren, Top mass effects in Higgs production at next-to-next-to-leading order QCD: virtual corrections. *Phys. Lett. B* **679**, 467 (2009). <https://doi.org/10.1016/j.physletb.2009.08.012>. arXiv:0907.2997 [hep-ph]
79. R.V. Harlander, K.J. Ozeren, Finite top mass effects for hadronic Higgs production at next-to-next-to-leading order. *JHEP* **11**, 088 (2009). <https://doi.org/10.1088/1126-6708/2009/11/088>. arXiv:0909.3420 [hep-ph]
80. F. Dulat, A. Lazopoulos, B. Mistlberger, iHiggs 2 - Inclusive Higgs cross sections. *Comput. Phys. Commun.* **233**, 243 (2018). <https://doi.org/10.1016/j.cpc.2018.06.025>. arXiv:1802.00827 [hep-ph]
81. C. Anastasiou, C. Duhr, F. Dulat, F. Herzog, B. Mistlberger, Higgs Boson Gluon-Fusion production in QCD at three loops. *Phys. Rev. Lett.* **114**, 212001 (2015). <https://doi.org/10.1103/PhysRevLett.114.212001>. arXiv:1503.06056 [hep-ph]
82. C. Anastasiou et al., High precision determination of the gluon fusion Higgs boson cross-section at the LHC. *JHEP* **05**, 058 (2016). [https://doi.org/10.1007/JHEP05\(2016\)058](https://doi.org/10.1007/JHEP05(2016)058). arXiv:1602.00695 [hep-ph]
83. M. Ciccolini, A. Denner, S. Dittmaier, Strong and electroweak corrections to the production of a Higgs Boson +2 Jets via Weak Interactions at the Large Hadron Collider. *Phys. Rev. Lett.* **99**, 161803 (2007). <https://doi.org/10.1103/PhysRevLett.99.161803>. arXiv:0707.0381 [hep-ph]
84. M. Ciccolini, A. Denner, S. Dittmaier, Electroweak and QCD corrections to Higgs production via vector-boson fusion at the CERN LHC. *Phys. Rev. D* **77**, 013002 (2008). <https://doi.org/10.1103/PhysRevD.77.013002>. arXiv:0710.4749 [hep-ph]
85. P. Bolzoni, F. Maltoni, S.-O. Moch, M. Zaro, Higgs Boson production via Vector-Boson Fusion at next-to-next-to-leading order in QCD. *Phys. Rev. Lett.* **105**, 011801 (2010). <https://doi.org/10.1103/PhysRevLett.105.011801>. arXiv:1003.4451 [hep-ph]
86. O. Brein, R.V. Harlander, T.J.E. Zirke, vh@nnlo - Higgs Strahlung at hadron colliders. *Comput. Phys. Commun.* **184**, 998 (2013). <https://doi.org/10.1016/j.cpc.2012.11.002>. arXiv:1210.5347 [hep-ph]
87. R.V. Harlander, J. Klappert, S. Liebler, L. Simon, vh@nnlo-v2: new physics in Higgs Strahlung. *JHEP* **05**, 089 (2018). [https://doi.org/10.1007/JHEP05\(2018\)089](https://doi.org/10.1007/JHEP05(2018)089). arXiv:1802.04817 [hep-ph]
88. O. Brein, A. Djouadi, R.V. Harlander, NNLO QCD corrections to the Higgs-strahlung processes at hadron colliders. *Phys. Lett. B* **579**, 149 (2004). <https://doi.org/10.1016/j.physletb.2003.10.112>. arXiv:hep-ph/0307206
89. O. Brein, R.V. Harlander, M. Wiesemann, T. Zirke, Top-quark mediated effects in hadronic Higgs-Strahlung. *Eur. Phys. J. C* **72**, 1868 (2012). <https://doi.org/10.1140/epjc/s10052-012-1868-6>. arXiv:1111.0761 [hep-ph]
90. A. Denner, S. Dittmaier, S. Kallweit, A. Mück, Electroweak corrections to Higgs-strahlung off W/Z bosons at the Tevatron and

- the LHC with HAWK. JHEP **03**, 075 (2012). [https://doi.org/10.1007/JHEP03\(2012\)075](https://doi.org/10.1007/JHEP03(2012)075). arXiv:1112.5142 [hep-ph]
91. L. Altenkamp, S. Dittmaier, R.V. Harlander, H. Rzehak, T.J.E. Zirke, Gluon-induced Higgs-strahlung at next-to-leading order QCD. JHEP **02**, 078 (2013). [https://doi.org/10.1007/JHEP02\(2013\)078](https://doi.org/10.1007/JHEP02(2013)078). arXiv:1211.5015 [hep-ph]
 92. R.V. Harlander, A. Kulesza, V. Theeuwes, T. Zirke, Soft gluon resummation for gluon-induced Higgs Strahlung. JHEP **11**, 082 (2014). [https://doi.org/10.1007/JHEP11\(2014\)082](https://doi.org/10.1007/JHEP11(2014)082). arXiv:1410.0217 [hep-ph]
 93. A. Denner, S. Dittmaier, S. Kallweit, A. Mück, HAWK 2.0: A Monte Carlo program for Higgs production in vector-boson fusion and Higgs strahlung at hadron colliders. Comput. Phys. Commun. **195**, 161 (2015). <https://doi.org/10.1016/j.cpc.2015.04.021>. arXiv:1412.5390 [hep-ph]
 94. M. Ciccolini, S. Dittmaier, M. Krämer, Electroweak radiative corrections to associated WH and ZH production at hadron colliders. Phys. Rev. D **68**, 073003 (2003). <https://doi.org/10.1103/PhysRevD.68.073003>. arXiv:hep-ph/0306234 [hep-ph]
 95. W. Beenakker et al., NLO QCD corrections to $t\bar{t}H$ production in hadron collisions. Nucl. Phys. B **653**, 151 (2003). [https://doi.org/10.1016/S0550-3213\(03\)00044-0](https://doi.org/10.1016/S0550-3213(03)00044-0). arXiv:hep-ph/0211352
 96. S. Dawson, C. Jackson, L. Orr, L. Reina, D. Wackerth, Associated Higgs boson production with top quarks at the CERN Large Hadron Collider: NLO QCD corrections. Phys. Rev. D **68**, 034022 (2003). <https://doi.org/10.1103/PhysRevD.68.034022>. arXiv:hep-ph/0305087
 97. Y. Zhang, W.-G. Ma, R.-Y. Zhang, C. Chen, L. Guo, QCD NLO and EW NLO corrections to $t\bar{t}H$ production with top quark decays at hadron collider. Phys. Lett. B **738**, 1 (2014). <https://doi.org/10.1016/j.physletb.2014.09.022>. arXiv:1407.1110 [hep-ph]
 98. S. Frixione, V. Hirschi, D. Pagani, H.-S. Shao, M. Zaro, Electroweak and QCD corrections to top-pair hadroproduction in association with heavy bosons. JHEP **06**, 184 (2015). [https://doi.org/10.1007/JHEP06\(2015\)184](https://doi.org/10.1007/JHEP06(2015)184). arXiv:1504.03446 [hep-ph]
 99. S. Dawson, C. Jackson, L. Reina, D. Wackerth, Exclusive Higgs boson production with bottom quarks at hadron colliders. Phys. Rev. D **69**, 074027 (2004). <https://doi.org/10.1103/PhysRevD.69.074027>. arXiv:hep-ph/0311067
 100. S. Dittmaier, M. Krämer, M. Spira, Higgs radiation off bottom quarks at the Tevatron and the CERN LHC. Phys. Rev. D **70**, 074010 (2004). <https://doi.org/10.1103/PhysRevD.70.074010>. arXiv:hep-ph/0309204
 101. R. Harlander, M. Kramer, M. Schumacher, Bottom-quark associated Higgs-boson production: reconciling the four- and five-flavour scheme approach. (2011), arXiv:1112.3478 [hep-ph]
 102. A. Bredenstein, A. Denner, S. Dittmaier, M. Weber, Precise predictions for the Higgs-boson decay $H \rightarrow WW/ZZ \rightarrow 4$ leptons. Phys. Rev. D **74**, 013004 (2006). <https://doi.org/10.1103/PhysRevD.74.013004>. arXiv:hep-ph/0604011
 103. A. Bredenstein, A. Denner, S. Dittmaier, M.M. Weber, Precision calculations for the Higgs decays $H \rightarrow ZZ/WW \rightarrow 4$ leptons. Nucl. Phys. Proc. Suppl. **160**, 131 (2006). <https://doi.org/10.1016/j.nuclphysbps.2006.09.104>. arXiv:hep-ph/0607060 [hep-ph]
 104. S. Boselli, C.M. Carloni Calame, G. Montagna, O. Nicrosini, F. Piccinini, Higgs boson decay into four leptons at NLOPS electroweak accuracy. JHEP **06**, 023 (2015). [https://doi.org/10.1007/JHEP06\(2015\)023](https://doi.org/10.1007/JHEP06(2015)023). arXiv:1503.07394 [hep-ph]
 105. A. Bredenstein, A. Denner, S. Dittmaier, M. Weber, Radiative corrections to the semileptonic and hadronic Higgs-boson decays $H \rightarrow WW/ZZ \rightarrow 4$ fermions. JHEP **02**, 080 (2007). <https://doi.org/10.1088/1126-6708/2007/02/080>. arXiv:hep-ph/0611234
 106. J. Aebischer et al., WCxf: an exchange format for Wilson coefficients beyond the Standard model. Comput. Phys. Commun. **232**, 71 (2018). <https://doi.org/10.1016/j.cpc.2018.05.022>. issn: 0010-4655
 107. A. Alloul, N.D. Christensen, C. Degrande, C. Duhr, B. Fuks, FeynRules 2.0 - a complete toolbox for tree-level phenomenology. Comp. Phys. Commun. **185**, 2250 (2014). <https://doi.org/10.1016/j.cpc.2014.04.012>
 108. C. Degrande et al., UFO - The universal FeynRules output. Comp. Phys. Commun. **183**, 1201 (2012). <https://doi.org/10.1016/j.cpc.2012.01.022>
 109. T. Gleisberg et al., Event generation with SHERPA 1.1. JHEP **02**, 007 (2009). <https://doi.org/10.1088/1126-6708/2009/02/007>. arXiv:0811.4622 [hep-ph]
 110. T. Gleisberg, S. Höche, Comix, a new matrix element generator. JHEP **12**, 039 (2008). <https://doi.org/10.1088/1126-6708/2008/12/039>. arXiv:0808.3674 [hep-ph]
 111. F. Cascioli, P. Maierhofer, S. Pozzorini, Scattering amplitudes with Open Loops. Phys. Rev. Lett. **108**, 111601 (2012). <https://doi.org/10.1103/PhysRevLett.108.111601>. arXiv:1111.5206 [hep-ph]
 112. E. Bothmann et al., Event generation with Sherpa 2.2. SciPost Phys. **7**, 034 (2019). <https://doi.org/10.21468/SciPostPhys.7.3.034>. arXiv:1905.09127 [hep-ph]
 113. S. Schumann, F. Krauss, A parton shower algorithm based on Catani-Seymour dipole factorisation. JHEP **03**, 038 (2008). <https://doi.org/10.1088/1126-6708/2008/03/038>. arXiv:0709.1027 [hep-ph]
 114. S. Höche, F. Krauss, M. Schönherr, F. Siegert, QCD matrix elements + parton showers. The NLO case, JHEP **04**, 027 (2013). [https://doi.org/10.1007/JHEP04\(2013\)027](https://doi.org/10.1007/JHEP04(2013)027). arXiv:1207.5030 [hep-ph]
 115. B. Biedermann, A. Denner, S. Dittmaier, L. Hofer, B. Jäger, Electroweak corrections to $pp \rightarrow \mu^+\mu^-e^+e^- + X$ at the LHC: a Higgs Boson Background Study. Phys. Rev. Lett. **116**, 161803 (2016). <https://doi.org/10.1103/PhysRevLett.116.161803>. arXiv:1601.07787 [hep-ph]
 116. B. Biedermann, A. Denner, S. Dittmaier, L. Hofer, B. Jäger, Next-to-leading-order electroweak corrections to the production of four charged leptons at the LHC. JHEP **01**, 033 (2017). [https://doi.org/10.1007/JHEP01\(2017\)033](https://doi.org/10.1007/JHEP01(2017)033). arXiv:1611.05338 [hep-ph]
 117. F. Caola, K. Melnikov, R. Röntsch, L. Tancredi, QCD corrections to ZZ production in gluon fusion at the LHC. Phys. Rev. D **92**, 094028 (2015). <https://doi.org/10.1103/PhysRevD.92.094028>. arXiv:1509.06734 [hep-ph]
 118. F. Caola, K. Melnikov, R. Röntsch, L. Tancredi, QCD corrections to W^+W^- production through gluon fusion. Phys. Lett. B **754**, 275 (2016). <https://doi.org/10.1016/j.physletb.2016.01.046>. arXiv:1511.08617 [hep-ph]
 119. J.M. Campbell, R.K. Ellis, M. Czakon, S. Kirchner, Two loop correction to interference in $gg \rightarrow ZZ$. JHEP **08**, 011 (2016). [https://doi.org/10.1007/JHEP08\(2016\)011](https://doi.org/10.1007/JHEP08(2016)011). arXiv:1605.01380 [hep-ph]
 120. K. Melnikov, M. Dowling, Production of two Z-bosons in gluon fusion in the heavy top quark approximation. Phys. Lett. B **744**, 43 (2015). <https://doi.org/10.1016/j.physletb.2015.03.030>. arXiv:1503.01274 [hep-ph]
 121. M. Bonvini, F. Caola, S. Forte, K. Melnikov, G. Ridolfi, Signal-background interference effects for $gg \rightarrow H \rightarrow W^+W^-$ beyond leading order. Phys. Rev. D **88**, 034032 (2013). <https://doi.org/10.1103/PhysRevD.88.034032>. arXiv:1304.3053 [hep-ph]
 122. C.S. Li, H.T. Li, D.Y. Shao, J. Wang, Soft gluon resummation in the signal-background interference process of $gg(\rightarrow h^*) \rightarrow ZZ$. JHEP **08**, 065 (2015). [https://doi.org/10.1007/JHEP08\(2015\)065](https://doi.org/10.1007/JHEP08(2015)065). arXiv:1504.02388 [hep-ph]
 123. P. Nason, G. Zanderighi, W^+W^- , WZ and ZZ production in the POWHEG-BOX-V2. Eur. Phys. J. C **74**, 2702 (2014). <https://doi.org/10.1140/epjc/s10052-013-2702-5>. arXiv:1311.1365 [hep-ph]

124. ATLAS Collaboration, The ATLAS Simulation Infrastructure. *Eur. Phys. J. C* **70**, 823 (2010). <https://doi.org/10.1140/epjc/s10052-010-1429-9>. arXiv:1005.4568 [physics.ins-det]
125. S. Agostinelli et al., GEANT4 - a simulation toolkit. *Nucl. Instrum. Meth. A* **506**, 250 (2003). [https://doi.org/10.1016/S0168-9002\(03\)01368-8](https://doi.org/10.1016/S0168-9002(03)01368-8)
126. ATLAS Collaboration, Summary of ATLAS Pythia 8 tunes, ATL-PHYS-PUB-2012-003, (2012), <https://cds.cern.ch/record/1474107>
127. A. Martin, W. Stirling, R. Thorne, G. Watt, Parton distributions for the LHC. *Eur. Phys. J. C* **63**, 189 (2009). <https://doi.org/10.1140/epjc/s10052-009-1072-5>. arXiv:0901.0002 [hep-ph]
128. ATLAS Collaboration, Measurement of inclusive and differential cross sections in the $H \rightarrow ZZ^* \rightarrow 4\ell$ decay channel in pp collisions at $\sqrt{s} = 13$ TeV with the ATLAS detector, *JHEP* **10**, 132 (2017). [https://doi.org/10.1007/JHEP10\(2017\)132](https://doi.org/10.1007/JHEP10(2017)132). arXiv:1708.02810 [hep-ex]
129. ATLAS Collaboration, Electron and photon performance measurements with the ATLAS detector using the 2015–2017 LHC proton–proton collision data. *JINST* **14**, P12006 (2019). <https://doi.org/10.1088/1748-0221/14/12/P12006>. arXiv:1908.00005 [hep-ex]
130. ATLAS Collaboration, Improved electron reconstruction in ATLAS using the Gaussian Sum Filter-based model for bremsstrahlung, ATLAS-CONF-2012-047, (2012), <https://cds.cern.ch/record/1449796>
131. ATLAS Collaboration, Muon reconstruction performance of the ATLAS detector in proton–proton collision data at $\sqrt{s} = 13$ TeV. *Eur. Phys. J. C* **76**, 292 (2016), <https://doi.org/10.1140/epjc/s10052-016-4120-y>. arXiv:1603.05598 [hep-ex]
132. ATLAS Collaboration, Topological cell clustering in the ATLAS calorimeters and its performance in LHC Run 1. *Eur. Phys. J. C* **77**, 490 (2017). <https://doi.org/10.1140/epjc/s10052-017-5004-5>. arXiv:1603.02934 [hep-ex]
133. ATLAS Collaboration, Jet energy scale measurements and their systematic uncertainties in proton–proton collisions at $\sqrt{s} = 13$ TeV with the ATLAS detector. *Phys. Rev. D* **96**, 072002 (2017). <https://doi.org/10.1103/PhysRevD.96.072002>. arXiv:1703.09665 [hep-ex]
134. ATLAS Collaboration, Jet mass reconstruction with the ATLAS Detector in early Run 2 data, ATLAS-CONF-2016-035, (2016), <https://cds.cern.ch/record/2200211>
135. ATLAS Collaboration, Tagging and suppression of pileup jets with the ATLAS detector, ATLASCONF- 2014-018, (2014), <https://cds.cern.ch/record/1700870>
136. ATLAS Collaboration, Performance of pile-up mitigation techniques for jets in pp collisions at $\sqrt{s} = 8$ TeV using the ATLAS detector. *Eur. Phys. J. C* **76**, 581 (2016), <https://doi.org/10.1140/epjc/s10052-016-4395-z>. arXiv:1510.03823 [hep-ex]
137. ATLAS Collaboration, Optimisation and performance studies of the ATLAS b-tagging algorithms for the 2017–18 LHC run, ATL-PHYS-PUB-2017-013, (2017), <https://cds.cern.ch/record/2273281>
138. ATLAS Collaboration, Measurements of b-jet tagging efficiency with the ATLAS detector using $t\bar{t}$ events at $\sqrt{s} = 13$ TeV. *JHEP* **08**, 089 (2018). [https://doi.org/10.1007/JHEP08\(2018\)089](https://doi.org/10.1007/JHEP08(2018)089). arXiv:1805.01845 [hep-ex]
139. ATLAS Collaboration, ATLAS b-jet identification performance and efficiency measurement with $t\bar{t}$ events in pp collisions at $\sqrt{s} = 13$ TeV. *Eur. Phys. J. C* **79**, 970 (2019). <https://doi.org/10.1140/epjc/s10052-019-7450-8>. arXiv:1907.05120 [hep-ex]
140. ATLAS Collaboration, Performance of missing transverse momentum reconstruction with the ATLAS detector using proton–proton collisions at $\sqrt{s} = 13$ TeV. *Eur. Phys. J. C* **78**, 903 (2018). <https://doi.org/10.1140/epjc/s10052-018-6288-9>. arXiv:1802.08168 [hep-ex]
141. ATLAS Collaboration, E_T^{miss} performance in the ATLAS detector using 2015–2016 LHC pp collisions, ATLAS-CONF-2018-023, (2018), <https://cds.cern.ch/record/2625233>
142. ATLAS Collaboration, 2015 start-up trigger menu and initial performance assessment of the ATLAS trigger using Run-2 data, ATL-DAQ-PUB-2016-001, (2016), <https://cds.cern.ch/record/2136007>
143. ATLAS Collaboration, Trigger Menu in 2016, ATL-DAQ-PUB-2017-001, (2017), <https://cds.cern.ch/record/2242069>
144. M. Tanabashi et al., Review of Particle Physics. *Phys. Rev. D* **98**, 030001 (3 2018). <https://doi.org/10.1103/PhysRevD.98.030001>
145. ATLAS Collaboration, Electron and photon reconstruction and performance in ATLAS using a dynamical, topological cell clustering-based approach, ATL-PHYS-PUB-2017-022, (2017), <https://cds.cern.ch/record/2298955>
146. ATLAS Collaboration, Measurements of the Higgs boson production, fiducial and differential cross sections in the 4ℓ decay channel at $\sqrt{s} = 13$ TeV with the ATLAS detector, ATLAS-CONF-2018-018, (2018), <https://cds.cern.ch/record/2621479>
147. ATLAS Collaboration, Measurement of the photon identification efficiencies with the ATLAS detector using LHC Run 2 data collected in 2015 and 2016. *Eur. Phys. J. C* **79**, 205 (2019). <https://doi.org/10.1140/epjc/s10052-019-6650-6>. arXiv:1810.05087 [hep-ex]
148. D. Guest, K. Cranmer, D. Whiteson, Deep learning and its application to LHC physics. *Ann. Rev. Nucl. Part. Sci.* **68**, 161 (2018). <https://doi.org/10.1146/annurev-nucl-101917-021019>. arXiv:1806.11484 [hep-ex]
149. F. Chollet et al., Keras, (2015), <https://keras.io>
150. M. Abadi et al., TensorFlow: Large-scale machine learning on heterogeneous systems, (2015), <https://doi.org/10.1007/978-3-642-24797-2>. <https://www.tensorflow.org/>
151. A. Graves, Supervised sequence labelling with recurrent neural networks, studies in computational intelligence, Springer, (2012), isbn: 978-3-642-24796-5, <https://cds.cern.ch/record/1503877>
152. I. Goodfellow, Y. Bengio, A. Courville, Deep learning, <http://www.deeplearningbook.org>, MIT Press, (2016)
153. ATLAS Collaboration, Measurements of Higgs boson production and couplings in the four-lepton channel in pp collisions at center-of-mass energies of 7 and 8 TeV with the ATLAS detector. *Phys. Rev. D* **91**, 012006 (2015). <https://doi.org/10.1103/PhysRevD.91.012006>. arXiv:1408.5191 [hep-ex]
154. D. Rainwater, R. Szalapski, D. Zeppenfeld, Probing color-singlet exchange in $Z + 2$ -jet events at the CERN LHC. *Phys. Rev. D* **54**, 6680 (1996). <https://doi.org/10.1103/physrevd.54.6680>
155. ATLAS Collaboration, Multi-Boson simulation for 13 TeV ATLAS analyses, ATL-PHYS-PUB- 2017-005, (2017), <https://cds.cern.ch/record/2261933>
156. M. Pivk, F.R. Le Diberder, $sPlot$: a statistical tool to unfold data distributions. *Nucl. Instrum. Meth. A* **555**, 356 (2005). <https://doi.org/10.1016/j.nima.2005.08.106>. arXiv:physics/0402083
157. ATLAS Collaboration, Luminosity determination in pp collisions at $\sqrt{s} = 13$ TeV using the ATLAS detector at the LHC, ATLAS-CONF-2019-021, (2019), <https://cds.cern.ch/record/2677054>
158. G. Avoni et al., The new LUCID-2 detector for luminosity measurement and monitoring in ATLAS. *JINST* **13**, P07017 (2018). <https://doi.org/10.1088/1748-0221/13/07/P07017>
159. ATLAS Collaboration, Measurement of the inelastic proton–proton cross section at $\sqrt{s} = 13$ TeV with the ATLAS detector at the LHC. *Phys. Rev. Lett.* **117**, 182002 (2016). <https://doi.org/10.1103/PhysRevLett.117.182002>. arXiv:1606.02625 [hep-ex]
160. ATLAS and CMS Collaborations, Combined measurement of the Higgs Boson mass in pp collisions at $\sqrt{s} = 7$ and 8 TeV with the ATLAS and CMS experiments. *Phys. Rev. Lett.* **114**, 191803 (2015). <https://doi.org/10.1103/PhysRevLett.114.191803>. arXiv:1503.07589 [hep-ex]

161. I.W. Stewart, F.J. Tackmann, Theory uncertainties for Higgs mass and other searches using jet bins. *Phys. Rev. D* **85**, 034011 (2012). <https://doi.org/10.1103/PhysRevD.85.034011>. arXiv:1107.2117 [hep-ph]
162. I.W. Stewart, F.J. Tackmann, J.R. Walsh, S. Zuberi, Jet p_T resummation in Higgs production at $NNLL' + NNLO$. *Phys. Rev. D* **89**, 054001 (2014). <https://doi.org/10.1103/PhysRevD.89.054001>. arXiv:1307.1808 [hep-ph]
163. X. Liu, F. Petriello, Reducing theoretical uncertainties for exclusive Higgs-boson plus one-jet production at the LHC. *Phys. Rev. D* **87**, 094027 (2013). <https://doi.org/10.1103/PhysRevD.87.094027>. arXiv:1303.4405 [hep-ph]
164. R. Boughezal, X. Liu, F. Petriello, F.J. Tackmann, J.R. Walsh, Combining resummed Higgs predictions across jet bins. *Phys. Rev. D* **89**, 074044 (2014). <https://doi.org/10.1103/PhysRevD.89.074044>. arXiv:1312.4535 [hep-ph]
165. S. Gangal, F.J. Tackmann, Next-to-leading-order uncertainties in Higgs +2 jets from gluon fusion. *Phys. Rev. D* **87**, 093008 (2013). <https://doi.org/10.1103/PhysRevD.87.093008>. arXiv:1302.5437 [hep-ph]
166. J.M. Campbell, R.K. Ellis, C. Williams, Vector boson pair production at the LHC. *JHEP* **07**, 018 (2011). [https://doi.org/10.1007/JHEP07\(2011\)018](https://doi.org/10.1007/JHEP07(2011)018). arXiv:1105.0020 [hep-ph]
167. ATLAS Collaboration, Evaluation of theoretical uncertainties for simplified template cross section measurements of V-associated production of the Higgs boson, ATL-PHYS-PUB-2018-035, (2018), <https://cds.cern.ch/record/2649241>
168. J. Bellm et al., Herwig 7.0/Herwig ++ 3.0 release note. *Eur. Phys. J. C* **76**, 196 (2016). <https://doi.org/10.1140/epjc/s10052-016-4018-8>. arXiv:1512.01178 [hep-ph]
169. S. Boselli et al., Higgs decay into four charged leptons in the presence of dimension-six operators. *JHEP* **01**, 096 (2018). [https://doi.org/10.1007/JHEP01\(2018\)096](https://doi.org/10.1007/JHEP01(2018)096). arXiv:1703.06667 [hep-ph]
170. G. Cowan, K. Cranmer, E. Gross, O. Vitells, Asymptotic formulae for likelihood-based tests of new physics. *Eur. Phys. J. C* **71**, 1554 (2011). <https://doi.org/10.1140/epjc/s10052-011-1554-0>. arXiv:1007.1727 [hep-ex], Erratum: *Eur. Phys. J. C* **73** (2013) 2501
171. C. Degrande, B. Fuks, K. Mawatari, K. Mimasu, V. Sanz, Electroweak Higgs boson production in the standard model effective field theory beyond leading order in QCD. *The European Physical Journal C* **77** (2017), <https://doi.org/10.1140/epjc/s10052-017-4793-x>, issn: 1434-6052
172. ATLAS Collaboration, ATLAS computing acknowledgements, ATL-GEN-PUB-2016-002, <https://cds.cern.ch/record/2202407>

ATLAS Collaboration

G. Aad¹⁰², B. Abbott¹²⁸, D. C. Abbott¹⁰³, A. Abed Abud³⁶, K. Abeling⁵³, D. K. Abhayasinghe⁹⁴, S. H. Abidi¹⁶⁶, O. S. AbouZeid⁴⁰, N. L. Abraham¹⁵⁵, H. Abramowicz¹⁶⁰, H. Abreu¹⁵⁹, Y. Abulaiti⁶, B. S. Acharya^{67a,67b,n}, B. Achkar⁵³, L. Adam¹⁰⁰, C. Adam Bourdarios⁵, L. Adamczyk^{84a}, L. Adamek¹⁶⁶, J. Adelman¹²¹, M. Adersberger¹¹⁴, A. Adiguzel^{12c}, S. Adorni⁵⁴, T. Adye¹⁴³, A. A. Affolder¹⁴⁵, Y. Afik¹⁵⁹, C. Agapopoulou⁶⁵, M. N. Agaras³⁸, A. Aggarwal¹¹⁹, C. Agheorghiesei^{27c}, J. A. Aguilar-Saavedra^{139f,139a,ad}, A. Ahmad³⁶, F. Ahmadov⁸⁰, W. S. Ahmed¹⁰⁴, X. Ai¹⁸, G. Aielli^{74a,74b}, S. Akatsuka⁸⁶, T. P. A. Åkesson⁹⁷, E. Akilli⁵⁴, A. V. Akimov¹¹¹, K. Al Khoury⁶⁵, G. L. Alberghi^{23a,23b}, J. Albert¹⁷⁵, M. J. Alconada Verzini¹⁶⁰, S. Alderweireldt³⁶, M. Aleksa³⁶, I. N. Aleksandrov⁸⁰, C. Alexa^{27b}, T. Alexopoulos¹⁰, A. Alfonsi¹²⁰, F. Alfonsi^{23a,23b}, M. Alhroob¹²⁸, B. Ali¹⁴¹, S. Ali¹⁵⁷, M. Aliev¹⁶⁵, G. Alimonti^{69a}, C. Allaire³⁶, B. M. M. Allbrooke¹⁵⁵, B. W. Allen¹³¹, P. P. Allport²¹, A. Aloisio^{70a,70b}, F. Alonso⁸⁹, C. Alpigiani¹⁴⁷, E. Alunno Camelia^{74a,74b}, M. Alvarez Estevez⁹⁹, M. G. Alviggi^{70a,70b}, Y. Amaral Coutinho^{81b}, A. Ambler¹⁰⁴, L. Ambroz¹³⁴, C. Amelung²⁶, D. Amidei¹⁰⁶, S. P. Amor Dos Santos^{139a}, S. Amoroso⁴⁶, C. S. Amrouche⁵⁴, F. An⁷⁹, C. Anastopoulos¹⁴⁸, N. Andari¹⁴⁴, T. Andeen¹¹, J. K. Anders²⁰, S. Y. Andrean^{45a,45b}, A. Andreazza^{69a,69b}, V. Andrei^{61a}, C. R. Anelli¹⁷⁵, S. Angelidakis⁹, A. Angerami³⁹, A. V. Anisenkov^{122a,122b}, A. Annovi^{72a}, C. Antel⁵⁴, M. T. Anthony¹⁴⁸, E. Antipov¹²⁹, M. Antonelli⁵¹, D. J. A. Antrim¹⁷⁰, F. Anulli^{73a}, M. Aoki⁸², J. A. Aparisi Pozo¹⁷³, M. A. Aparo¹⁵⁵, L. Aperio Bella⁴⁶, N. Aranzabal Barrio³⁶, V. Araujo Ferraz^{81a}, R. Araujo Pereira^{81b}, C. Arcangeletti⁵¹, A. T. H. Arce⁴⁹, F. A. Arduh⁸⁹, J-F. Arguin¹¹⁰, S. Argyropoulos⁵², J.-H. Arling⁴⁶, A. J. Armbruster³⁶, A. Armstrong¹⁷⁰, O. Arnaez¹⁶⁶, H. Arnold¹²⁰, Z. P. Arrubarrena Tame¹¹⁴, G. Artoni¹³⁴, K. Asai¹²⁶, S. Asai¹⁶², T. Asawatavonvanich¹⁶⁴, N. Asbah⁵⁹, E. M. Asimakopoulou¹⁷¹, L. Asquith¹⁵⁵, J. Assahsah^{35d}, K. Assamagan²⁹, R. Astalos^{28a}, R. J. Atkin^{33a}, M. Atkinson¹⁷², N. B. Atlay¹⁹, H. Atmani⁶⁵, K. Augsten¹⁴¹, V. A. Austrup¹⁸¹, G. Avolio³⁶, M. K. Ayoub^{15a}, G. Azeul^{110,al}, H. Bachacou¹⁴⁴, K. Bachas¹⁶¹, M. Backes¹³⁴, F. Backman^{45a,45b}, P. Bagnaia^{73a,73b}, M. Bahmani⁸⁵, H. Bahrasemani¹⁵¹, A. J. Bailey¹⁷³, V. R. Bailey¹⁷², J. T. Baines¹⁴³, C. Bakalis¹⁰, O. K. Baker¹⁸², P. J. Bakker¹²⁰, E. Bakos¹⁶, D. Bakshi Gupta⁸, S. Balaji¹⁵⁶, E. M. Baldin^{122a,122b}, P. Balek¹⁷⁹, F. Balli¹⁴⁴, W. K. Balunas¹³⁴, J. Balz¹⁰⁰, E. Banas⁸⁵, M. Bandieramonte¹³⁸, A. Bandyopadhyay²⁴, Sw. Banerjee^{180,j}, L. Barak¹⁶⁰, W. M. Barbe³⁸, E. L. Barberio¹⁰⁵, D. Barberis^{55a,55b}, M. Barbero¹⁰², G. Barbour⁹⁵, T. Barillari¹¹⁵, M.-S. Barisits³⁶, J. Barkeloo¹³¹, T. Barklow¹⁵², R. Barnea¹⁵⁹, B. M. Barnett¹⁴³, R. M. Barnett¹⁸, Z. Barnovska-Blenessy^{60a}, A. Baroncelli^{60a}, G. Barone²⁹, A. J. Barr¹³⁴, L. Barranco Navarro^{45a,45b}, F. Barreiro⁹⁹, J. Barreiro Guimarães da Costa^{15a}, U. Barron¹⁶⁰, S. Barsov¹³⁷, F. Bartels^{61a}, R. Bartoldus¹⁵², G. Bartolini¹⁰², A. E. Barton⁹⁰, P. Bartos^{28a}, A. Basalae⁴⁶, A. Basan¹⁰⁰, A. Bassalat^{65,ai}, M. J. Basso¹⁶⁶

R. L. Bates⁵⁷, S. Batlamous^{35e}, J. R. Batley³², B. Batool¹⁵⁰, M. Battaglia¹⁴⁵, M. Bauce^{73a,73b}, F. Bauer¹⁴⁴, K. T. Bauer¹⁷⁰, H. S. Bawa³¹, A. Bayirli^{12c}, J. B. Beacham⁴⁹, T. Beau¹³⁵, P. H. Beauchemin¹⁶⁹, F. Becherer⁵², P. Bechtle²⁴, H. C. Beck⁵³, H. P. Beck^{20,p}, K. Becker¹⁷⁷, C. Becot⁴⁶, A. Beddall^{12d}, A. J. Beddall^{12a}, V. A. Bednyakov⁸⁰, M. Bedognetti¹²⁰, C. P. Bee¹⁵⁴, T. A. Beermann¹⁸¹, M. Begalli^{81b}, M. Begel²⁹, A. Behera¹⁵⁴, J. K. Behr⁴⁶, F. Beisiegel²⁴, M. Belfkir⁵, A. S. Bell⁹⁵, G. Bella¹⁶⁰, L. Bellagamba^{23b}, A. Bellerive³⁴, P. Bellos⁹, K. Beloborodov^{122a,122b}, K. Belotskiy¹¹², N. L. Belyaev¹¹², D. Benchebkroun^{35a}, N. Benekos¹⁰, Y. Benhammou¹⁶⁰, D. P. Benjamin⁶, M. Benoit⁵⁴, J. R. Bensinger²⁶, S. Bentvelsen¹²⁰, L. Beresford¹³⁴, M. Beretta⁵¹, D. Berge¹⁹, E. Bergeas Kuutmann¹⁷¹, N. Berger⁵, B. Bergmann¹⁴¹, L. J. Bergsten²⁶, J. Beringer¹⁸, S. Berlendis⁷, G. Bernardi¹³⁵, C. Bernius¹⁵², F. U. Bernlochner²⁴, T. Berry⁹⁴, P. Berta¹⁰⁰, C. Bertella^{15a}, A. Berthold⁴⁸, I. A. Bertram⁹⁰, O. Bessidskaia Bylund¹⁸¹, N. Besson¹⁴⁴, A. Bethani¹⁰¹, S. Bethke¹¹⁵, A. Betti⁴², A. J. Bevan⁹³, J. Beyer¹¹⁵, D. S. Bhattacharya¹⁷⁶, P. Bhattacharai²⁶, V. S. Bhopatkar⁶, R. Bi¹³⁸, R. M. Bianchi¹³⁸, O. Biebel¹¹⁴, D. Biedermann¹⁹, R. Bielski³⁶, K. Bierwagen¹⁰⁰, N. V. Biesuz^{72a,72b}, M. Biglietti^{75a}, T. R. V. Billoud¹¹⁰, M. Bindi⁵³, A. Bingul^{12d}, C. Bini^{73a,73b}, S. Biondi^{23a,23b}, C. J. Birch-sykes¹⁰¹, M. Birman¹⁷⁹, T. Bisanz⁵³, J. P. Biswal³, D. Biswas^{180,i}, A. Bitadze¹⁰¹, C. Bittrich⁴⁸, K. Björke¹³³, T. Blazek^{28a}, I. Bloch⁴⁶, C. Blocker²⁶, A. Blue⁵⁷, U. Blumenschein⁹³, G. J. Bobbink¹²⁰, V. S. Bobrovnikov^{122a,122b}, S. S. Bocchetta⁹⁷, D. Boerner⁴⁶, D. Bogavac¹⁴, A. G. Bogdanchikov^{122a,122b}, C. Bohm^{45a}, V. Boisvert⁹⁴, P. Bokan^{53,171}, T. Bold^{84a}, A. E. Bolz^{61b}, M. Bomben¹³⁵, M. Bona⁹³, J. S. Bonilla¹³¹, M. Boonekamp¹⁴⁴, C. D. Booth⁹⁴, H. M. Borecka-Bielska⁹¹, L. S. Borgna⁹⁵, A. Borisov¹²³, G. Borissov⁹⁰, J. Bortfeldt³⁶, D. Bortoletto¹³⁴, D. Boscherini^{23b}, M. Bosman¹⁴, J. D. Bossio Sola¹⁰⁴, K. Bouaouda^{35a}, J. Boudreau¹³⁸, E. V. Bouhova-Thacker⁹⁰, D. Boumediene³⁸, S. K. Boutle⁵⁷, A. Boveia¹²⁷, J. Boyd³⁶, D. Boye^{33c}, I. R. Boyko⁸⁰, A. J. Bozson⁹⁴, J. Bracinik²¹, N. Brahimi^{60d}, G. Brandt¹⁸¹, O. Brandt³², F. Braren⁴⁶, B. Brau¹⁰³, J. E. Brau¹³¹, W. D. Breaden Madden⁵⁷, K. Brendlinger⁴⁶, L. Brenner³⁶, R. Brenner¹⁷¹, S. Bressler¹⁷⁹, B. Brickwedde¹⁰⁰, D. L. Briglin²¹, D. Britton⁵⁷, D. Britzger¹¹⁵, I. Brock²⁴, R. Brock¹⁰⁷, G. Brooijmans³⁹, W. K. Brooks^{146d}, E. Brost²⁹, P. A. Bruckman de Renstrom⁸⁵, B. Brüers⁴⁶, D. Bruncko^{28b}, A. Bruni^{23b}, G. Bruni^{23b}, L. S. Bruni¹²⁰, S. Bruno^{74a,74b}, M. Bruschi^{23b}, N. Brusino^{73a,73b}, L. Bryngemark¹⁵², T. Buanes¹⁷, Q. Buat³⁶, P. Buchholz¹⁵⁰, A. G. Buckley⁵⁷, I. A. Budagov⁸⁰, M. K. Bugge¹³³, F. Bühner⁵², O. Bulekov¹¹², B. A. Bullard⁵⁹, T. J. Burch¹²¹, S. Burdin⁹¹, C. D. Burgard¹²⁰, A. M. Burger¹²⁹, B. Burghgrave⁸, J. T. P. Burr⁴⁶, C. D. Burton¹¹, J. C. Burzynski¹⁰³, V. Büscher¹⁰⁰, E. Buschmann⁵³, P. J. Bussey⁵⁷, J. M. Butler²⁵, C. M. Buttar⁵⁷, J. M. Butterworth⁹⁵, P. Butti³⁶, W. Buttinger³⁶, C. J. Buxo Vazquez¹⁰⁷, A. Buzatu¹⁵⁷, A. R. Buzykaev^{122a,122b}, G. Cabras^{23a,23b}, S. Cabrera Urbán¹⁷³, D. Caforio⁵⁶, H. Cai¹³⁸, V. M. M. Cairo¹⁵², O. Cakir^{4a}, N. Calace³⁶, P. Calafiura¹⁸, G. Calderini¹³⁵, P. Calfayan⁶⁶, G. Callea⁵⁷, L. P. Caloba^{81b}, A. Caltabiano^{74a,74b}, S. Calvente Lopez⁹⁹, D. Calvet³⁸, S. Calvet³⁸, T. P. Calvet¹⁰², M. Calvetti^{72a,72b}, R. Camacho Toro¹³⁵, S. Camarda³⁶, D. Camarero Munoz⁹⁹, P. Camarri^{74a,74b}, M. T. Camerlingo^{75a,75b}, D. Cameron¹³³, C. Camincher³⁶, S. Campana³⁶, M. Campanelli⁹⁵, A. Camplani⁴⁰, V. Canale^{70a,70b}, A. Canesse¹⁰⁴, M. Cano Bret⁷⁸, J. Cantero¹²⁹, T. Cao¹⁶⁰, Y. Cao¹⁷², M. D. M. Capeans Garrido³⁶, M. Capua^{41a,41b}, R. Cardarelli^{74a}, F. Cardillo¹⁴⁸, G. Carducci^{41a,41b}, I. Carli¹⁴², T. Carli³⁶, G. Carlino^{70a}, B. T. Carlson¹³⁸, E. M. Carlson^{175,167a}, L. Carminati^{69a,69b}, R. M. D. Carney¹⁵², S. Caron¹¹⁹, E. Carquin^{146d}, S. Carrá⁴⁶, G. Carratta^{23a,23b}, J. W. S. Carter¹⁶⁶, T. M. Carter⁵⁰, M. P. Casado^{14,f}, A. F. Casha¹⁶⁶, F. L. Castillo¹⁷³, L. Castillo Garcia¹⁴, V. Castillo Gimenez¹⁷³, N. F. Castro^{139a,139e}, A. Catinaccio³⁶, J. R. Catmore¹³³, A. Cattai³⁶, V. Cavaliere²⁹, V. Cavasinni^{72a,72b}, E. Celebi^{12b}, F. Celli¹³⁴, K. Cerny¹³⁰, A. S. Cerqueira^{81a}, A. Cerri¹⁵⁵, L. Cerrito^{74a,74b}, F. Cerutti¹⁸, A. Cervelli^{23a,23b}, S. A. Cetin^{12b}, Z. Chadi^{35a}, D. Chakraborty¹²¹, J. Chan¹⁸⁰, W. S. Chan¹²⁰, W. Y. Chan⁹¹, J. D. Chapman³², B. Chargeishvili^{158b}, D. G. Charlton²¹, T. P. Charman⁹³, C. C. Chau³⁴, S. Che¹²⁷, S. Chekanov⁶, S. V. Chekulaev^{167a}, G. A. Chelkov^{80,ag}, B. Chen⁷⁹, C. Chen^{60a}, C. H. Chen⁷⁹, H. Chen²⁹, J. Chen^{60a}, J. Chen³⁹, J. Chen²⁶, S. Chen¹³⁶, S. J. Chen^{15c}, X. Chen^{15b}, Y. Chen^{60a}, Y-H. Chen⁴⁶, H. C. Cheng^{63a}, H. J. Cheng^{15a}, A. Cheplakov⁸⁰, E. Cheremushkina¹²³, R. Cherkaoui El Moursli^{35e}, E. Cheu⁷, K. Cheung⁶⁴, T. J. A. Chevaléras¹⁴⁴, L. Chevalier¹⁴⁴, V. Chiarella⁵¹, G. Chiarelli^{72a}, G. Chiodini^{68a}, A. S. Chisholm²¹, A. Chitan^{27b}, I. Chiu¹⁶², Y. H. Chiu¹⁷⁵, M. V. Chizhov⁸⁰, K. Choi¹¹, A. R. Chomont^{73a,73b}, Y. S. Chow¹²⁰, L. D. Christopher^{33e}, M. C. Chu^{63a}, X. Chu^{15a,15d}, J. Chudoba¹⁴⁰, J. J. Chwastowski⁸⁵, L. Chytka¹³⁰, D. Cieri¹¹⁵, K. M. Ciesla⁸⁵, D. Cinca⁴⁷, V. Cindro⁹², I. A. Cioară^{27b}, A. Ciochio¹⁸, F. Ciroto^{70a,70b}, Z. H. Citron^{179,j}, M. Citterio^{69a}, D. A. Ciubotaru^{27b}, B. M. Ciungu¹⁶⁶, A. Clark⁵⁴, M. R. Clark³⁹, P. J. Clark⁵⁰, S. E. Clawson¹⁰¹, C. Clement^{45a,45b}, Y. Coadou¹⁰², M. Cobal^{67a,67c}

A. Coccaro^{55b}, J. Cochran⁷⁹, R. Coelho Lopes De Sa¹⁰³, H. Cohen¹⁶⁰, A. E. C. Coimbra³⁶, B. Cole³⁹, A. P. Colijn¹²⁰, J. Collot⁵⁸, P. Conde Muiño^{139a,139b}, S. H. Connell^{33c}, I. A. Connelly⁵⁷, S. Constantinescu^{27b}, F. Conventi^{70a.am}, A. M. Cooper-Sarkar¹³⁴, F. Cormier¹⁷⁴, K. J. R. Cormier¹⁶⁶, L. D. Corpe⁹⁵, M. Corradi^{73a,73b}, E. E. Corrigan⁹⁷, F. Corriveau^{104.ab}, M. J. Costa¹⁷³, F. Costanza⁵, D. Costanzo¹⁴⁸, G. Cowan⁹⁴, J. W. Cowley³², J. Crane¹⁰¹, K. Cranmer¹²⁵, R. A. Creager¹³⁶, S. Crépe-Renaudin⁵⁸, F. Crescioli¹³⁵, M. Cristinziani²⁴, V. Croft¹⁶⁹, G. Crosetti^{41a,41b}, A. Cueto⁵, T. Cuhadar Donszelmann¹⁷⁰, H. Cui^{15a,15d}, A. R. Cukierman¹⁵², W. R. Cunningham⁵⁷, S. Czekerda⁸⁵, P. Czodrowski³⁶, M. M. Czurylo^{61b}, M. J. Da Cunha Sargedas De Sousa^{60b}, J. V. Da Fonseca Pinto^{81b}, C. Da Via¹⁰¹, W. Dabrowski^{84a}, F. Dachs³⁶, T. Dado⁴⁷, S. Dahbi^{33e}, T. Dai¹⁰⁶, C. Dallapiccola¹⁰³, M. Dam⁴⁰, G. D'amen²⁹, V. D'Amico^{75a,75b}, J. Damp¹⁰⁰, J. R. Dandoy¹³⁶, M. F. Daneri³⁰, M. Danninger¹⁵¹, V. Dao³⁶, G. Darbo^{55b}, O. Dartsis⁵, A. Dattagupta¹³¹, T. Daubney⁴⁶, S. D'Auria^{69a,69b}, C. David^{167b}, T. Davidek¹⁴², D. R. Davis⁴⁹, I. Dawson¹⁴⁸, K. De⁸, R. De Asmundis^{70a}, M. De Beurs¹²⁰, S. De Castro^{23a,23b}, N. De Groot¹¹⁹, P. de Jong¹²⁰, H. De la Torre¹⁰⁷, A. De Maria^{15c}, D. De Pedis^{73a}, A. De Salvo^{73a}, U. De Sanctis^{74a,74b}, M. De Santis^{74a,74b}, A. De Santo¹⁵⁵, J. B. De Vivie De Regie⁶⁵, C. Debenedetti¹⁴⁵, D. V. Dedovich⁸⁰, A. M. Deiana⁴², J. Del Peso⁹⁹, Y. Delabat Diaz⁴⁶, D. Delgove⁶⁵, F. Deliot¹⁴⁴, C. M. Delitzsch⁷, M. Della Pietra^{70a,70b}, D. Della Volpe⁵⁴, A. Dell'Acqua³⁶, L. Dell'Asta^{74a,74b}, M. Delmastro⁵, C. Delporte⁶⁵, P. A. Delsart⁵⁸, D. A. DeMarco¹⁶⁶, S. Demers¹⁸², M. Demichev⁸⁰, G. Demontigny¹¹⁰, S. P. Denisov¹²³, L. D'Eramo¹²¹, D. Derendarz⁸⁵, J. E. Derkaoui^{35d}, F. Derue¹³⁵, P. Dervan⁹¹, K. Desch²⁴, K. Dette¹⁶⁶, C. Deutsch²⁴, M. R. Devesa³⁰, P. O. Deviveiros³⁶, F. A. Di Bello^{73a,73b}, A. Di Ciaccio^{74a,74b}, L. Di Ciaccio⁵, W. K. Di Clemente¹³⁶, C. Di Donato^{70a,70b}, A. Di Girolamo³⁶, G. Di Gregorio^{72a,72b}, B. Di Micco^{75a,75b}, R. Di Nardo^{75a,75b}, K. F. Di Petrillo⁵⁹, R. Di Sipio¹⁶⁶, C. Diaconu¹⁰², F. A. Dias⁴⁰, T. Dias Do Vale^{139a}, M. A. Diaz^{146a}, F. G. Diaz Capriles²⁴, J. Dickinson¹⁸, M. Didenko¹⁶⁵, E. B. Diehl¹⁰⁶, J. Dietrich¹⁹, S. Díez Cornell⁴⁶, A. Dimitrievska¹⁸, W. Ding^{15b}, J. Dingfelder²⁴, S. J. Dittmeier^{61b}, F. Dittus³⁶, F. Djama¹⁰², T. Djobava^{158b}, J. I. Djuvsland¹⁷, M. A. B. Do Vale^{81c}, M. Dobre^{27b}, D. Dodsworth²⁶, C. Doglioni⁹⁷, J. Dolejsi¹⁴², Z. Dolezal¹⁴², M. Donadelli^{81d}, B. Dong^{60c}, J. Donini³⁸, A. D'onofrio^{15c}, M. D'Onofrio⁹¹, J. Dopke¹⁴³, A. Doria^{70a}, M. T. Dova⁸⁹, A. T. Doyle⁵⁷, E. Drechsler¹⁵¹, E. Dreyer¹⁵¹, T. Dreyer⁵³, A. S. Drobac¹⁶⁹, D. Du^{60b}, T. A. du Pree¹²⁰, Y. Duan^{60d}, F. Dubinin¹¹¹, M. Dubovsky^{28a}, A. Dubreuil⁵⁴, E. Duchovni¹⁷⁹, G. Duckeck¹¹⁴, O. A. Ducu³⁶, D. Duda¹¹⁵, A. Dudarev³⁶, A. C. Dudder¹⁰⁰, E. M. Duffield¹⁸, M. D'uffizi¹⁰¹, L. Duflo⁶⁵, M. Dührssen³⁶, C. Dülsen¹⁸¹, M. Dumancic¹⁷⁹, A. E. Dumitriu^{27b}, M. Dunford^{61a}, A. Duperrin¹⁰², H. Duran Yildiz^{4a}, M. Düren⁵⁶, A. Durglishvili^{158b}, D. Duschinger⁴⁸, B. Dutta⁴⁶, D. Duvnjak¹, G. I. Dyckes¹³⁶, M. Dyndal³⁶, S. Dysch¹⁰¹, B. S. Dziedzic⁸⁵, M. G. Eggleston⁴⁹, T. Eifert⁸, G. Eigen¹⁷, K. Einsweiler¹⁸, T. Ekelof¹⁷¹, H. El Jarrari^{35e}, V. Ellajosyula¹⁷¹, M. Ellert¹⁷¹, F. Ellinghaus¹⁸¹, A. A. Elliot⁹³, N. Ellis³⁶, J. Elmsheuser²⁹, M. Elsing³⁶, D. Emelianov¹⁴³, A. Eberman³⁹, Y. Enari¹⁶², M. B. Epland⁴⁹, J. Erdmann⁴⁷, A. Ereditato²⁰, P. A. Erland⁸⁵, M. Errenst³⁶, M. Escalier⁶⁵, C. Escobar¹⁷³, O. Estrada Pastor¹⁷³, E. Etzion¹⁶⁰, H. Evans⁶⁶, M. O. Evans¹⁵⁵, A. Ezhilov¹³⁷, F. Fabbri⁵⁷, L. Fabbri^{23a,23b}, V. Fabiani¹¹⁹, G. Facini¹⁷⁷, R. M. Faisca Rodrigues Pereira^{139a}, R. M. Fakhruddinov¹²³, S. Falciano^{73a}, P. J. Falke²⁴, S. Falke³⁶, J. Faltova¹⁴², Y. Fang^{15a}, Y. Fang^{15a}, G. Fanourakis⁴⁴, M. Fanti^{69a,69b}, M. Faraj^{67a,67c,q}, A. Farbin⁸, A. Farilla^{75a}, E. M. Farina^{71a,71b}, T. Farooque¹⁰⁷, S. M. Farrington⁵⁰, P. Farthouat³⁶, F. Fassi^{35e}, P. Fassnacht³⁶, D. Fassouliotis⁹, M. Fauci Giannelli⁵⁰, W. J. Fawcett³², L. Fayard⁶⁵, O. L. Fedin^{137,o}, W. Fedorko¹⁷⁴, A. Fehr²⁰, M. Feickert¹⁷², L. Felgioni¹⁰², A. Fell¹⁴⁸, C. Feng^{60b}, M. Feng⁴⁹, M. J. Fenton¹⁷⁰, A. B. Fenyuk¹²³, S. W. Ferguson⁴³, J. Ferrando⁴⁶, A. Ferrante¹⁷², A. Ferrari¹⁷¹, P. Ferrari¹²⁰, R. Ferrari^{71a}, D. E. Ferreira de Lima^{61b}, A. Ferrer¹⁷³, D. Ferrere⁵⁴, C. Ferretti¹⁰⁶, F. Fiedler¹⁰⁰, A. Filipčič⁹², F. Filthaut¹¹⁹, K. D. Finelli²⁵, M. C. N. Fiolhais^{139a,139c.a}, L. Fiorini¹⁷³, F. Fischer¹¹⁴, J. Fischer¹⁰⁰, W. C. Fisher¹⁰⁷, T. Fitschen²¹, I. Fleck¹⁵⁰, P. Fleischmann¹⁰⁶, T. Flick¹⁸¹, B. M. Flierl¹¹⁴, L. Flores¹³⁶, L. R. Flores Castillo^{63a}, F. M. Follega^{76a,76b}, N. Fomin¹⁷, J. H. Foo¹⁶⁶, G. T. Forcolin^{76a,76b}, B. C. Forland⁶⁶, A. Formica¹⁴⁴, F. A. Förster¹⁴, A. C. Forti¹⁰¹, E. Fortin¹⁰², M. G. Foti¹³⁴, D. Fournier⁶⁵, H. Fox⁹⁰, P. Francavilla^{72a,72b}, S. Francescato^{73a,73b}, M. Franchini^{23a,23b}, S. Franchino^{61a}, D. Francis³⁶, L. Franco⁵, L. Franconi²⁰, M. Franklin⁵⁹, G. Frattari^{73a,73b}, A. N. Fray⁹³, P. M. Freeman²¹, B. Freund¹¹⁰, W. S. Freund^{81b}, E. M. Freundlich⁴⁷, D. C. Frizzell¹²⁸, D. Froidevaux³⁶, J. A. Frost¹³⁴, M. Fujimoto¹²⁶, C. Fukunaga¹⁶³, E. Fullana Torregrosa¹⁷³, T. Fusayasu¹¹⁶, J. Fuster¹⁷³, A. Gabrielli^{23a,23b}, A. Gabrielli³⁶, S. Gadatsch⁵⁴, P. Gadow¹¹⁵, G. Gagliardi^{55a,55b}, L. G. Gagnon¹¹⁰, G. E. Gallardo¹³⁴, E. J. Gallas¹³⁴, B. J. Gallop¹⁴³, G. Galster⁴⁰, R. Gamboa Goni⁹³, K. K. Gan¹²⁷, S. Ganguly¹⁷⁹, J. Gao^{60a}, Y. Gao⁵⁰, Y. S. Gao^{31,1}, F. M. Garay Walls^{146a}, C. García¹⁷³, J. E. García Navarro¹⁷³, J. A. García Pascual^{15a}























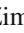

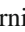





C. Garcia-Argos⁵², M. Garcia-Sciveres¹⁸, R. W. Gardner³⁷, N. Garelli¹⁵², S. Gargiulo⁵², C. A. Garner¹⁶⁶, V. Garonne¹³³, S. J. Gasiorowski¹⁴⁷, P. Gaspar^{81b}, A. Gaudiello^{55a,55b}, G. Gaudio^{71a}, I. L. Gavrilenko¹¹¹, A. Gavriluk¹²⁴, C. Gay¹⁷⁴, G. Gaycken⁴⁶, E. N. Gazis¹⁰, A. A. Geanta^{27b}, C. M. Gee¹⁴⁵, C. N. P. Gee¹⁴³, J. Geisen⁹⁷, M. Geisen¹⁰⁰, C. Gemme^{55b}, M. H. Genest⁵⁸, C. Geng¹⁰⁶, S. Gentile^{73a,73b}, S. George⁹⁴, T. Gerialis⁴⁴, L. O. Gerlach⁵³, P. Gessinger-Befurt¹⁰⁰, G. Gessner⁴⁷, S. Ghasemi¹⁵⁰, M. Ghasemi Bostanabad¹⁷⁵, M. Ghneimat¹⁵⁰, A. Ghosh⁶⁵, A. Ghosh⁷⁸, B. Giacobbe^{23b}, S. Giagu^{73a,73b}, N. Giangiacomi^{23a,23b}, P. Giannetti^{72a}, A. Giannini^{70a,70b}, G. Giannini¹⁴, S. M. Gibson⁹⁴, M. Gignac¹⁴⁵, D. T. Gil^{84b}, D. Gillberg³⁴, G. Gilles¹⁸¹, D. M. Gingrich^{3,al}, M. P. Giordani^{67a,67c}, P. F. Giraud¹⁴⁴, G. Giugliarelli^{67a,67c}, D. Giugni^{69a}, F. Giuli^{74a,74b}, S. Gkaitatzis¹⁶¹, I. Gkialas^{9,g}, E. L. Gkoukousis¹⁴, P. Gkoutoumis¹⁰, L. K. Gladilin¹¹³, C. Glasman⁹⁹, J. Glatzer¹⁴, P. C. F. Glaysher⁴⁶, A. Glazov⁴⁶, G. R. Gledhill¹³¹, I. Gnesi^{41b,b}, M. Goblirsch-Kolb²⁶, D. Godin¹¹⁰, S. Goldfarb¹⁰⁵, T. Golling⁵⁴, D. Golubkov¹²³, A. Gomes^{139a,139b}, R. Goncalves Gama⁵³, R. Gonçalo^{139a,139c}, G. Gonella¹³¹, L. Gonella²¹, A. Gongadze⁸⁰, F. Gonnella²¹, J. L. Gonski³⁹, S. González de la Hoz¹⁷³, S. Gonzalez Fernandez¹⁴, R. Gonzalez Lopez⁹¹, C. Gonzalez Renteria¹⁸, R. Gonzalez Suarez¹⁷¹, S. Gonzalez-Sevilla⁵⁴, G. R. Gonzalvo Rodriguez¹⁷³, L. Goossens³⁶, N. A. Gorasia²¹, P. A. Gorbounov¹²⁴, H. A. Gordon²⁹, B. Gorini³⁶, E. Gorini^{68a,68b}, A. Gorišek⁹², A. T. Goshaw⁴⁹, M. I. Gostkin⁸⁰, C. A. Gottardo¹¹⁹, M. Gouighri^{35b}, A. G. Goussiou¹⁴⁷, N. Govender^{33c}, C. Goy⁵, I. Grabowska-Bold^{84a}, E. C. Graham⁹¹, J. Gramling¹⁷⁰, E. Gramstad¹³³, S. Grancagnolo¹⁹, M. Grandi¹⁵⁵, V. Gratchev¹³⁷, P. M. Gravila^{27f}, F. G. Gravili^{68a,68b}, C. Gray⁵⁷, H. M. Gray¹⁸, C. Greife²⁴, K. Gregersen⁹⁷, I. M. Gregor⁴⁶, P. Grenier¹⁵², K. Grevtsov⁴⁶, C. Grieco¹⁴, N. A. Grieser¹²⁸, A. A. Grillo¹⁴⁵, K. Grimm^{31,k}, S. Grinstein^{14,w}, J.-F. Grivaz⁶⁵, S. Groh¹⁰⁰, E. Gross¹⁷⁹, J. Grosse-Knetter⁵³, Z. J. Grout⁹⁵, C. Grud¹⁰⁶, A. Grummer¹¹⁸, J. C. Grundy¹³⁴, L. Guan¹⁰⁶, W. Guan¹⁸⁰, C. Gubbels¹⁷⁴, J. Guenther³⁶, A. Guerguichon⁶⁵, J. G. R. Guerrero Rojas¹⁷³, F. Guescini¹¹⁵, D. Guest¹⁷⁰, R. Gugel¹⁰⁰, T. Guillemain⁵, S. Guindon³⁶, U. Gul⁵⁷, J. Guo^{60c}, W. Guo¹⁰⁶, Y. Guo^{60a}, Z. Guo¹⁰², R. Gupta⁴⁶, S. Gurbuz^{12c}, G. Gustavino¹²⁸, M. Guth⁵², P. Gutierrez¹²⁸, C. Gutsche⁹⁵, C. Guyot¹⁴⁴, C. Gwenlan¹³⁴, C. B. Gwilliam⁹¹, E. S. Haaland¹³³, A. Haas¹²⁵, C. Haber¹⁸, H. K. Hadavand⁸, A. Hader^{60a}, M. Haleem¹⁷⁶, J. Haley¹²⁹, J. J. Hall¹⁴⁸, G. Halladjian¹⁰⁷, G. D. Hallewell¹⁰², K. Hamano¹⁷⁵, H. Hamdaoui^{35c}, M. Hamer²⁴, G. N. Hamity⁵⁰, K. Han^{60a,v}, L. Han^{60a}, S. Han¹⁸, Y. F. Han¹⁶⁶, K. Hanagaki^{82,t}, M. Hance¹⁴⁵, D. M. Handl¹¹⁴, M. D. Hank³⁷, R. Hankache¹³⁵, E. Hansen⁹⁷, J. B. Hansen⁴⁰, J. D. Hansen⁴⁰, M. C. Hansen²⁴, P. H. Hansen⁴⁰, E. C. Hanson¹⁰¹, K. Hara¹⁶⁸, T. Harenberg¹⁸¹, S. Harkusha¹⁰⁸, P. F. Harrison¹⁷⁷, N. M. Hartman¹⁵², N. M. Hartmann¹¹⁴, Y. Hasegawa¹⁴⁹, A. Hasib⁵⁰, S. Hassani¹⁴⁴, S. Haug²⁰, R. Hauser¹⁰⁷, L. B. Havener³⁹, M. Havranek¹⁴¹, C. M. Hawkes²¹, R. J. Hawkins³⁶, S. Hayashida¹¹⁷, D. Hayden¹⁰⁷, C. Hayes¹⁰⁶, R. L. Hayes¹⁷⁴, C. P. Hays¹³⁴, J. M. Hays⁹³, H. S. Hayward⁹¹, S. J. Haywood¹⁴³, F. He^{60a}, Y. He¹⁶⁴, M. P. Heath⁵⁰, V. Hedberg⁹⁷, S. Heer²⁴, A. L. Heggelund¹³³, C. Heidegger⁵², K. K. Heidegger⁵², W. D. Heidorn⁷⁹, J. Heilman³⁴, S. Heim⁴⁶, T. Heim¹⁸, B. Heinemann^{46,aj}, J. J. Heinrich¹³¹, L. Heinrich³⁶, J. Hejbal¹⁴⁰, L. Helary⁴⁶, A. Held¹²⁵, S. Hellesund¹³³, C. M. Helling¹⁴⁵, S. Hellman^{45a,45b}, C. Helsen³⁶, R. C. W. Henderson⁹⁰, Y. Heng¹⁸⁰, L. Henkelmann³², A. M. Henriques Correia³⁶, H. Herde²⁶, Y. Hernández Jiménez^{33e}, H. Herr¹⁰⁰, M. G. Herrmann¹¹⁴, T. Herrmann⁴⁸, G. Herten⁵², R. Hertenberger¹¹⁴, L. Hervas³⁶, T. C. Herwig¹³⁶, G. G. Hesketh⁹⁵, N. P. Hessey^{167a}, H. Hibi⁸³, A. Higashida¹⁶², S. Higashino⁸², E. Higón-Rodríguez¹⁷³, K. Hildebrand³⁷, J. C. Hill³², K. K. Hill²⁹, K. H. Hiller⁴⁶, S. J. Hillier²¹, M. Hils⁴⁸, I. Hinchliffe¹⁸, F. Hinterkeuser²⁴, M. Hirose¹³², S. Hirose⁵², D. Hirschbuehl¹⁸¹, B. Hiti⁹², O. Hladik¹⁴⁰, D. R. Hlaluku^{33e}, J. Hobbs¹⁵⁴, N. Hod¹⁷⁹, M. C. Hodgkinson¹⁴⁸, A. Hoecker³⁶, D. Hohn⁵², D. Hohov⁶⁵, T. Holm²⁴, T. R. Holmes³⁷, M. Holzbock¹¹⁴, L. B. A. H. Hommels³², T. M. Hong¹³⁸, J. C. Honig⁵², A. Hönle¹¹⁵, B. H. Hooberman¹⁷², W. H. Hopkins⁶, Y. Horii¹¹⁷, P. Horn⁴⁸, L. A. Horyn³⁷, S. Hou¹⁵⁷, A. Hoummada^{35a}, J. Howarth⁵⁷, J. Hoya⁸⁹, M. Hrabovsky¹³⁰, J. Hrdinka⁷⁷, J. Hrivnac⁶⁵, A. Hrynevich¹⁰⁹, T. Hryn'ova⁵, P. J. Hsu⁶⁴, S.-C. Hsu¹⁴⁷, Q. Hu²⁹, S. Hu^{60c}, Y. F. Hu^{15a,15d,an}, D. P. Huang⁹⁵, Y. Huang^{60a}, Y. Huang^{15a}, Z. Hubacek¹⁴¹, F. Hubaut¹⁰², M. Huebner²⁴, F. Huegging²⁴, T. B. Huffman¹³⁴, M. Huhtinen³⁶, R. Hulsken⁵⁸, R. F. H. Hunter³⁴, P. Huo¹⁵⁴, N. Huseynov^{80,ac}, J. Huston¹⁰⁷, J. Huth⁵⁹, R. Hyneman¹⁰⁶, S. Hyrych^{28a}, G. Iacobucci⁵⁴, G. Iakovidis²⁹, I. Ibragimov¹⁵⁰, L. Iconomidou-Fayard⁶⁵, P. Iengo³⁶, R. Ignazzi⁴⁰, O. Igonkina^{120,y,*}, R. Iguchi¹⁶², T. Iizawa⁵⁴, Y. Ikegami⁸², M. Ikeno⁸², D. Iliadis¹⁶¹, N. Ilic^{119,166,ab}, F. Iltzsche⁴⁸, H. Imam^{35a}, G. Introzzi^{71a,71b}, M. Iodice^{75a}, K. Iordanidou^{167a}, V. Ippolito^{73a,73b}, M. F. Isacson¹⁷¹, M. Ishino¹⁶², W. Islam¹²⁹, C. Issever^{19,46}, S. Istin¹⁵⁹, F. Ito¹⁶⁸, J. M. Iturbe Ponce^{63a}, R. Iuppa^{76a,76b}, A. Ivina¹⁷⁹, H. Iwasaki⁸², J. M. Izen⁴³, V. Izzo^{70a}, P. Jacka¹⁴⁰, P. Jackson¹, R. M. Jacobs⁴⁶, B. P. Jaeger¹⁵¹, V. Jain², G. Jäkel¹⁸¹, K. B. Jakobi¹⁰⁰, K. Jakobs⁵², T. Jakoubek¹⁷⁹

M. Lokajicek¹⁴⁰, J. D. Long¹⁷², R. E. Long⁹⁰, I. Longarini^{73a,73b}, L. Longo³⁶, K. A. Looper¹²⁷, I. Lopez Paz¹⁰¹, A. Lopez Solis¹⁴⁸, J. Lorenz¹¹⁴, N. Lorenzo Martinez⁵, A. M. Lory¹¹⁴, P. J. Lösel¹¹⁴, A. Lösle⁵², X. Lou⁴⁶, X. Lou^{15a}, A. Lounis⁶⁵, J. Love⁶, P. A. Love⁹⁰, J. J. Lozano Bahilo¹⁷³, M. Lu^{60a}, Y. J. Lu⁶⁴, H. J. Lubatti¹⁴⁷, C. Luci^{73a,73b}, F. L. Lucio Alves^{15c}, A. Lucotte⁵⁸, F. Luehring⁶⁶, I. Luise¹³⁵, L. Luminari^{73a}, B. Lund-Jensen¹⁵³, M. S. Lutz¹⁶⁰, D. Lynn²⁹, H. Lyons⁹¹, R. Lysak¹⁴⁰, E. Lytken⁹⁷, F. Lyu^{15a}, V. Lyubushkin⁸⁰, T. Lyubushkina⁸⁰, H. Ma²⁹, L. L. Ma^{60b}, Y. Ma⁹⁵, D. M. Mac Donell¹⁷⁵, G. Maccarrone⁵¹, A. Macchiolo¹¹⁵, C. M. Macdonald¹⁴⁸, J. C. Macdonald¹⁴⁸, J. Machado Miguens¹³⁶, D. Madaffari¹⁷³, R. Madar³⁸, W. F. Mader⁴⁸, M. Madugoda Ralalage Don¹²⁹, N. Madysa⁴⁸, J. Maeda⁸³, T. Maeno²⁹, M. Maerker⁴⁸, V. Magerl⁵², N. Magini⁷⁹, J. Magro^{67a,67c,q}, D. J. Mahon³⁹, C. Maidantchik^{81b}, T. Maier¹¹⁴, A. Maio^{139a,139b,139d}, K. Maj^{84a}, O. Majersky^{28a}, S. Majewski¹³¹, Y. Makida⁸², N. Makovec⁶⁵, B. Malaescu¹³⁵, Pa. Malecki⁸⁵, V. P. Maleev¹³⁷, F. Malek⁵⁸, D. Malito^{41a,41b}, U. Mallik⁷⁸, D. Malon⁶, C. Malone³², S. Maltezos¹⁰, S. Malyukov⁸⁰, J. Mamuzic¹⁷³, G. Mancini^{70a,70b}, I. Mandić⁹², L. Manhaes de Andrade Filho^{81a}, I. M. Maniatis¹⁶¹, J. Manjarres Ramos⁴⁸, K. H. Mankinen⁹⁷, A. Mann¹¹⁴, A. Manousos⁷⁷, B. Mansoulie¹⁴⁴, I. Mantos¹⁶¹, S. Manzoni¹²⁰, A. Marantis¹⁶¹, G. Marceca³⁰, L. Marchese¹³⁴, G. Marchiori¹³⁵, M. Marcisovsky¹⁴⁰, L. Marcocchia^{74a,74b}, C. Marcon⁹⁷, C. A. Marin Tobon³⁶, M. Marjanovic¹²⁸, Z. Marshall¹⁸, M. U. F. Martensson¹⁷¹, S. Marti-Garcia¹⁷³, C. B. Martin¹²⁷, T. A. Martin¹⁷⁷, V. J. Martin⁵⁰, B. Martin dit Latour¹⁷, L. Martinelli^{75a,75b}, M. Martinez^{14,w}, P. Martinez Agullo¹⁷³, V. I. Martinez Outschoorn¹⁰³, S. Martin-Haugh¹⁴³, V. S. Martoiu^{27b}, A. C. Martyniuk⁹⁵, A. Marzin³⁶, S. R. Maschek¹¹⁵, L. Masetti¹⁰⁰, T. Mashimo¹⁶², R. Mashinistov¹¹¹, J. Masik¹⁰¹, A. L. Maslennikov^{122a,122b}, L. Massa^{23a,23b}, P. Massarotti^{70a,70b}, P. Mastrandrea^{72a,72b}, A. Mastroberardino^{41a,41b}, T. Masubuchi¹⁶², D. Matakias²⁹, A. Matic¹¹⁴, N. Matsuzawa¹⁶², P. Mättig²⁴, J. Maurer^{27b}, B. Maček⁹², D. A. Maximov^{122a,122b}, R. Mazini¹⁵⁷, I. Maznas¹⁶¹, S. M. Mazza¹⁴⁵, J. P. Mc Gowan¹⁰⁴, S. P. Mc Kee¹⁰⁶, T. G. McCarthy¹¹⁵, W. P. McCormack¹⁸, E. F. McDonald¹⁰⁵, J. A. Mcfayden³⁶, G. Mchedlidze^{158b}, M. A. McKay⁴², K. D. McLean¹⁷⁵, S. J. McMahon¹⁴³, P. C. McNamara¹⁰⁵, C. J. McNicol¹⁷⁷, R. A. McPherson^{175,ab}, J. E. Mdhluli^{33e}, Z. A. Meadows¹⁰³, S. Meehan³⁶, T. Megy³⁸, S. Mehlhase¹¹⁴, A. Mehta⁹¹, B. Meirose⁴³, D. Melini¹⁵⁹, B. R. Mellado Garcia^{33e}, J. D. Mellenthin⁵³, M. Melo^{28a}, F. Meloni⁴⁶, A. Melzer²⁴, E. D. Mendes Gouveia^{139a,139e}, L. Meng³⁶, X. T. Meng¹⁰⁶, S. Menke¹¹⁵, E. Meoni^{41a,41b}, S. Mergelmeyer¹⁹, S. A. M. Merkt¹³⁸, C. Merlassino¹³⁴, P. Mermod⁵⁴, L. Merola^{70a,70b}, C. Meroni^{69a}, G. Merz¹⁰⁶, O. Meshkov^{113,111}, J. K. R. Meshreki¹⁵⁰, J. Metcalfe⁶, A. S. Mete⁶, C. Meyer⁶⁶, J.-P. Meyer¹⁴⁴, M. Michetti¹⁹, R. P. Middleton¹⁴³, L. Mijovic⁵⁰, G. Mikenberg¹⁷⁹, M. Mikestikova¹⁴⁰, M. Mikuž⁹², H. Mildner¹⁴⁸, A. Milic¹⁶⁶, C. D. Milke⁴², D. W. Miller³⁷, A. Milov¹⁷⁹, D. A. Milstead^{45a,45b}, R. A. Mina¹⁵², A. A. Minaenko¹²³, I. A. Minashvili^{158b}, A. I. Mincer¹²⁵, B. Mindur^{84a}, M. Mineev⁸⁰, Y. Minegishi¹⁶², L. M. Mir¹⁴, M. Mironova¹³⁴, A. Mirto^{68a,68b}, K. P. Mistry¹³⁶, T. Mitani¹⁷⁸, J. Mitrevski¹¹⁴, V. A. Mitsou¹⁷³, M. Mittal^{60c}, O. Miu¹⁶⁶, A. Miucci²⁰, P. S. Miyagawa⁹³, A. Mizukami⁸², J. U. Mjörnmark⁹⁷, T. Mkrtchyan^{61a}, M. Mlynarikova¹⁴², T. Moa^{45a,45b}, S. Mobius⁵³, K. Mochizuki¹¹⁰, P. Mogg¹¹⁴, S. Mohapatra³⁹, R. Moles-Valls²⁴, K. Mönig⁴⁶, E. Monnier¹⁰², A. Montalbano¹⁵¹, J. Montejo Berlingen³⁶, M. Montella⁹⁵, F. Monticelli⁸⁹, S. Monzani^{69a}, N. Morange⁶⁵, D. Moreno^{22a}, M. Moreno Llácer¹⁷³, C. Moreno Martinez¹⁴, P. Morettini^{55b}, M. Morgenstern¹⁵⁹, S. Morgenstern⁴⁸, D. Mori¹⁵¹, M. Morii⁵⁹, M. Morinaga¹⁷⁸, V. Morisbak¹³³, A. K. Morley³⁶, G. Mornacchi³⁶, A. P. Morris⁹⁵, L. Morvaj¹⁵⁴, P. Moschovakos³⁶, B. Moser¹²⁰, M. Mosidze^{158b}, T. Moskalets¹⁴⁴, H. J. Moss¹⁴⁸, J. Moss^{31,m}, E. J. W. Moyses¹⁰³, S. Muanza¹⁰², J. Mueller¹³⁸, R. S. P. Mueller¹¹⁴, D. Muenstermann⁹⁰, G. A. Mullier⁹⁷, D. P. Mungo^{69a,69b}, J. L. Munoz Martinez¹⁴, F. J. Munoz Sanchez¹⁰¹, P. Murin^{28b}, W. J. Murray^{177,143}, A. Murrone^{69a,69b}, J. M. Muse¹²⁸, M. Muškinja¹⁸, C. Mwewa^{33a}, A. G. Myagkov^{123,ag}, A. A. Myers¹³⁸, J. Myers¹³¹, M. Myska¹⁴¹, B. P. Nachman¹⁸, O. Nackenhorst⁴⁷, A. Nag Nag⁴⁸, K. Nagai¹³⁴, K. Nagano⁸², Y. Nagasaka⁶², J. L. Nagle²⁹, E. Nagy¹⁰², A. M. Nairz³⁶, Y. Nakahama¹¹⁷, K. Nakamura⁸², T. Nakamura¹⁶², H. Nanjo¹³², F. Napolitano^{61a}, R. F. Naranjo Garcia⁴⁶, R. Narayan⁴², I. Naryshkin¹³⁷, T. Naumann⁴⁶, G. Navarro^{22a}, P. Y. Nechaeva¹¹¹, F. Nechansky⁴⁶, T. J. Neep²¹, A. Negri^{71a,71b}, M. Negrini^{23b}, C. Nellist¹¹⁹, C. Nelson¹⁰⁴, M. E. Nelson^{45a,45b}, S. Nemecek¹⁴⁰, M. Nessi^{36,e}, M. S. Neubauer¹⁷², F. Neuhaus¹⁰⁰, M. Neumann¹⁸¹, R. Newhouse¹⁷⁴, P. R. Newman²¹, C. W. Ng¹³⁸, Y. S. Ng¹⁹, Y. W. Y. Ng¹⁷⁰, B. Ngair^{35e}, H. D. N. Nguyen¹⁰², T. Nguyen Manh¹¹⁰, E. Nibigira³⁸, R. B. Nickerson¹³⁴, R. Nicolaidou¹⁴⁴, D. S. Nielsen⁴⁰, J. Nielsen¹⁴⁵, M. Niemeyer⁵³, N. Nikiforou¹¹, V. Nikolaenko^{123,ag}, I. Nikolic-Audit¹³⁵, K. Nikolopoulos²¹, P. Nilsson²⁹, H. R. Nindhito⁵⁴, Y. Ninomiya⁸², A. Nisati^{73a}, N. Nishu^{60c}, R. Nisius¹¹⁵, I. Nitsche⁴⁷, T. Nitta¹⁷⁸, T. Nobe¹⁶², D. L. Noel³², Y. Noguchi⁸⁶, I. Nomidis¹³⁵, M. A. Nomura²⁹

M. Nordberg³⁶, J. Novak⁹², T. Novak⁹², O. Novgorodova⁴⁸, R. Novotny¹⁴¹, L. Nozka¹³⁰, K. Ntekas¹⁷⁰, E. Nurse⁹⁵, F. G. Oakham^{34,al}, H. Oberlack¹¹⁵, J. Ocariz¹³⁵, A. Ochi⁸³, I. Ochoa³⁹, J. P. Ochoa-Ricoux^{146a}, K. O'Connor²⁶, S. Oda⁸⁸, S. Odaka⁸², S. Oerdek⁵³, A. Ogrodnik^{84a}, A. Oh¹⁰¹, S. H. Oh⁴⁹, C. C. Ohm¹⁵³, H. Oide¹⁶⁴, M. L. Ojeda¹⁶⁶, H. Okawa¹⁶⁸, Y. Okazaki⁸⁶, M. W. O'Keefe⁹¹, Y. Okumura¹⁶², T. Okuyama⁸², A. Olariu^{27b}, L. F. Oleiro Seabra^{139a}, S. A. Olivares Pino^{146a}, D. Oliveira Damazio²⁹, J. L. Oliver¹, M. J. R. Olsson¹⁷⁰, A. Olszewski⁸⁵, J. Olszowska⁸⁵, Ö.O. Öncel²⁴, D. C. O'Neil¹⁵¹, A. P. O'Neill¹³⁴, A. Onofre^{139a,139e}, P. U. E. Onyisi¹¹, H. Oppen¹³³, R. G. Oreamuno Madriz¹²¹, M. J. Oreglia³⁷, G. E. Orellana⁸⁹, D. Orestano^{75a,75b}, N. Orlando¹⁴, R. S. Orr¹⁶⁶, V. O'Shea⁵⁷, R. Ospanov^{60a}, G. Otero y Garzon³⁰, H. Otono⁸⁸, P. S. Ott^{61a}, G. J. Ottino¹⁸, M. Ouchrif^{35d}, J. Ouellette²⁹, F. Ould-Saada¹³³, A. Ouraou¹⁴⁴, Q. Ouyang^{15a}, M. Owen⁵⁷, R. E. Owen¹⁴³, V. E. Ozcan^{12c}, N. Ozturk⁸, J. Pacalt¹³⁰, H. A. Pacey³², K. Pachal⁴⁹, A. Pacheco Pages¹⁴, C. Padilla Aranda¹⁴, S. Pagan Griso¹⁸, G. Palacino⁶⁶, S. Palazzo⁵⁰, S. Palestini³⁶, M. Palka^{84b}, P. Palmi^{84a}, C. E. Pandini⁵⁴, J. G. Panduro Vazquez⁹⁴, P. Pani⁴⁶, G. Panizzo^{67a,67c}, L. Paolozzi⁵⁴, C. Papadatos¹¹⁰, K. Papageorgiou^{9,g}, S. Parajuli⁴², A. Paramonov⁶, C. Paraskevopoulos¹⁰, D. Paredes Hernandez^{63b}, S. R. Paredes Saenz¹³⁴, B. Parida¹⁷⁹, T. H. Park¹⁶⁶, A. J. Parker³¹, M. A. Parker³², F. Parodi^{55a,55b}, E. W. Parrish¹²¹, J. A. Parsons³⁹, U. Parzefall⁵², L. Pascual Dominguez¹³⁵, V. R. Pascuzzi¹⁸, J. M. P. Pasner¹⁴⁵, F. Pasquali¹²⁰, E. Pasqualucci^{73a}, S. Passaggio^{55b}, F. Pastore⁹⁴, P. Pasuwan^{45a,45b}, S. Patariaia¹⁰⁰, J. R. Pater¹⁰¹, A. Pathak^{180,i}, J. Patton⁹¹, T. Pauly³⁶, J. Pearkes¹⁵², B. Pearson¹¹⁵, M. Pedersen¹³³, L. Pedraza Diaz¹¹⁹, R. Pedro^{139a}, T. Peiffer⁵³, S. V. Peleganchuk^{122a,122b}, O. Penc¹⁴⁰, H. Peng^{60a}, B. S. Peralva^{81a}, M. M. Perego⁶⁵, A. P. Pereira Peixoto^{139a}, L. Pereira Sanchez^{45a,45b}, D. V. Perepelitsa²⁹, E. Perez Codina^{167a}, F. Peri¹⁹, L. Perini^{69a,69b}, H. Pernegger³⁶, S. Perrella³⁶, A. Perrevoort¹²⁰, K. Peters⁴⁶, R. F. Y. Peters¹⁰¹, B. A. Petersen³⁶, T. C. Petersen⁴⁰, E. Petit¹⁰², V. Petousis¹⁴¹, A. Petridis¹, C. Petridou¹⁶¹, P. Petroff⁶⁵, F. Petrucci^{75a,75b}, M. Pettee¹⁸², N. E. Pettersson¹⁰³, K. Petukhova¹⁴², A. Peyaud¹⁴⁴, R. Pezoa^{146d}, L. Pezzotti^{71a,71b}, T. Pham¹⁰⁵, F. H. Phillips¹⁰⁷, P. W. Phillips¹⁴³, M. W. Phipps¹⁷², G. Piacquadio¹⁵⁴, E. Pianori¹⁸, A. Picazio¹⁰³, R. H. Pickles¹⁰¹, R. Piegai³⁰, D. Pietreanu^{27b}, J. E. Pilcher³⁷, A. D. Pilkington¹⁰¹, M. Pinamonti^{67a,67c}, J. L. Pinfold³, C. Pitman Donaldson⁹⁵, M. Pitt¹⁶⁰, L. Pizzimento^{74a,74b}, M.-A. Pleier²⁹, V. Pleskot¹⁴², E. Plotnikova⁸⁰, P. Podberezko^{122a,122b}, R. Poettgen⁹⁷, R. Poggi⁵⁴, L. Poggioli¹³⁵, I. Pogrebnyak¹⁰⁷, D. Pohl²⁴, I. Pokharel⁵³, G. Polesello^{71a}, A. Poley^{151,167a}, A. Policicchio^{73a,73b}, R. Polifka¹⁴², A. Polini^{23b}, C. S. Pollard⁴⁶, V. Polychronakos²⁹, D. Ponomarenko¹¹², L. Pontecorvo³⁶, S. Popa^{27a}, G. A. Popeneciu^{27d}, L. Portales⁵, D. M. Portillo Quintero⁵⁸, S. Pospisil¹⁴¹, K. Potamianos⁴⁶, I. N. Potrap⁸⁰, C. J. Potter³², H. Potti¹¹, T. Poulsen⁹⁷, J. Poveda¹⁷³, T. D. Powell¹⁴⁸, G. Pownall⁴⁶, M. E. Pozo Astigarraga³⁶, P. Pralavorio¹⁰², S. Prell⁷⁹, D. Price¹⁰¹, M. Primavera^{68a}, M. L. Proffitt¹⁴⁷, N. Proklova¹¹², K. Prokofiev^{63c}, F. Prokoshin⁸⁰, S. Protopopescu²⁹, J. Proudfoot⁶, M. Przybycien^{84a}, D. Pudzha¹³⁷, A. Puri¹⁷², P. Puzo⁶⁵, D. Pyatizbyantseva¹¹², J. Qian¹⁰⁶, Y. Qin¹⁰¹, A. Quadt⁵³, M. Queitsch-Maitland³⁶, A. Qureshi¹, M. Racko^{28a}, F. Ragusa^{69a,69b}, G. Rahal⁹⁸, J. A. Raine⁵⁴, S. Rajagopalan²⁹, A. Ramirez Morales⁹³, K. Ran^{15a,15d}, D. M. Rauch⁴⁶, F. Rauscher¹¹⁴, S. Rave¹⁰⁰, B. Ravina¹⁴⁸, I. Ravinovich¹⁷⁹, J. H. Rawling¹⁰¹, M. Raymond³⁶, A. L. Read¹³³, N. P. Readioff⁵⁸, M. Reale^{68a,68b}, D. M. Rebuffi^{71a,71b}, G. Redlinger²⁹, K. Reeves⁴³, J. Reichert¹³⁶, D. Reikher¹⁶⁰, A. Reiss¹⁰⁰, A. Rej¹⁵⁰, C. Rembsen³⁶, A. Renardi⁴⁶, M. Renda^{27b}, M. B. Rendel¹¹⁵, S. Resconi^{69a}, E. D. Resseguie¹⁸, S. Rettie⁹⁵, B. Reynolds¹²⁷, E. Reynolds²¹, O. L. Rezanova^{122a,122b}, P. Reznicek¹⁴², E. Ricci^{76a,76b}, R. Richter¹¹⁵, S. Richter⁴⁶, E. Richter-Was^{84b}, M. Ridel¹³⁵, P. Rieck¹¹⁵, O. Rifki⁴⁶, M. Rijssenbeek¹⁵⁴, A. Rimoldi^{71a,71b}, M. Rimoldi⁴⁶, L. Rinaldi^{23b}, T. T. Rinn¹⁷², G. Ripellino¹⁵³, I. Riu¹⁴, P. Rivadeneira⁴⁶, J. C. Rivera Vergara¹⁷⁵, F. Rizatdinova¹²⁹, E. Rizvi⁹³, C. Rizzi³⁶, S. H. Robertson^{104,ab}, M. Robin⁴⁶, D. Robinson³², C. M. Robles Gajardo^{146d}, M. Robles Manzano¹⁰⁰, A. Robson⁵⁷, A. Rocchi^{74a,74b}, E. Rocco¹⁰⁰, C. Roda^{72a,72b}, S. Rodriguez Bosca¹⁷³, A. M. Rodríguez Vera^{167b}, S. Roe³⁶, J. Roggel¹⁸¹, O. Röhne¹³³, R. Röhrig¹¹⁵, R. A. Rojas^{146d}, B. Roland⁵², C. P. A. Roland⁶⁶, J. Roloff²⁹, A. Romaniouk¹¹², M. Romano^{23a,23b}, N. Rompotis⁹¹, M. Ronzani¹²⁵, L. Roos¹³⁵, S. Rosati^{73a}, G. Rosin¹⁰³, B. J. Rosser¹³⁶, E. Rossi⁴⁶, E. Rossi^{75a,75b}, E. Rossi^{70a,70b}, L. P. Rossi^{55b}, L. Rossini^{69a,69b}, R. Rosten¹⁴, M. Rotaru^{27b}, B. Rottler⁵², D. Rousseau⁶⁵, G. Rovelli^{71a,71b}, A. Roy¹¹, D. Roy^{33e}, A. Rozanov¹⁰², Y. Rozen¹⁵⁹, X. Ruan^{33e}, F. Rühr⁵², A. Ruiz-Martinez¹⁷³, A. Rummler³⁶, Z. Rurikova⁵², N. A. Rusakovich⁸⁰, H. L. Russell¹⁰⁴, L. Rustige^{38,47}, J. P. Rutherford⁷, E. M. Rüttinger¹⁴⁸, M. Rybar³⁹, G. Rybkin⁶⁵, E. B. Rye¹³³, A. Ryzhov¹²³, J. A. Sabater Iglesias⁴⁶, P. Sabatini⁵³, L. Sabetta^{73a,73b}, S. Sacerdoti⁶⁵, H.F.-W. Sadrozinski¹⁴⁵, R. Sadykov⁸⁰, F. Safai Tehrani^{73a}, B. Safarzadeh Samani¹⁵⁵, M. Safdari¹⁵²

P. Saha¹²¹, S. Saha¹⁰⁴, M. Sahinsoy¹¹⁵, A. Sahu¹⁸¹, M. Saimpert³⁶, M. Saito¹⁶², T. Saito¹⁶², H. Sakamoto¹⁶², D. Salamani⁵⁴, G. Salamanna^{75a,75b}, A. Salmikov¹⁵², J. Salt¹⁷³, A. Salvador Salas¹⁴, D. Salvatore^{41a,41b}, F. Salvatore¹⁵⁵, A. Salvucci^{63a,63b,63c}, A. Salzburger³⁶, J. Samarati³⁶, D. Sammel⁵², D. Sampsonidis¹⁶¹, D. Sampsonidou¹⁶¹, J. Sánchez¹⁷³, A. Sanchez Pineda^{67a,67c}, H. Sandaker¹³³, C. O. Sander⁴⁶, I. G. Sanderswood⁹⁰, M. Sandhoff¹⁸¹, C. Sandoval^{22a}, D. P. C. Sankey¹⁴³, M. Sannino^{55a,55b}, Y. Sano¹¹⁷, A. Sansoni⁵¹, C. Santoni³⁸, H. Santos^{139a,139b}, S. N. Santpur¹⁸, A. Santra¹⁷³, K. A. Saouha¹⁴⁸, A. Sapronov⁸⁰, J. G. Saraiva^{139a,139d}, O. Sasaki⁸², K. Sato¹⁶⁸, F. Sauerburger⁵², E. Sauvan⁵, P. Savard^{166,al}, R. Sawada¹⁶², C. Sawyer¹⁴³, L. Sawyer^{96,af}, I. Sayago Galvan¹⁷³, C. Sbarra^{23b}, A. Sbrizzi^{67a,67c}, T. Scanlon⁹⁵, J. Schaarschmidt¹⁴⁷, P. Schacht¹¹⁵, D. Schaefer³⁷, L. Schaefer¹³⁶, S. Schaepe³⁶, U. Schäfer¹⁰⁰, A. C. Schaffer⁶⁵, D. Schaile¹¹⁴, R. D. Schamberger¹⁵⁴, E. Schanet¹¹⁴, N. Scharmberg¹⁰¹, V. A. Schegelsky¹³⁷, D. Scheirich¹⁴², F. Schenck¹⁹, M. Schernau¹⁷⁰, C. Schiavi^{55a,55b}, L. K. Schildgen²⁴, Z. M. Schillaci²⁶, E. J. Schioppa^{68a,68b}, M. Schioppa^{41a,41b}, K. E. Schleicher⁵², S. Schlenker³⁶, K. R. Schmidt-Sommerfeld¹¹⁵, K. Schmieden³⁶, C. Schmitt¹⁰⁰, S. Schmitt⁴⁶, J. C. Schmoedel⁴⁶, L. Schoeffel¹⁴⁴, A. Schoening^{61b}, P. G. Scholer⁵², E. Schopf¹³⁴, M. Schott¹⁰⁰, J. F. P. Schouwenberg¹¹⁹, J. Schovancova³⁶, S. Schramm⁵⁴, F. Schroeder¹⁸¹, A. Schulte¹⁰⁰, H-C. Schultz-Coulon^{61a}, M. Schumacher⁵², B. A. Schumm¹⁴⁵, Ph. Schune¹⁴⁴, A. Schwartzman¹⁵², T. A. Schwarz¹⁰⁶, Ph. Schwemling¹⁴⁴, R. Schwienhorst¹⁰⁷, A. Sciandra¹⁴⁵, G. Sciolla²⁶, M. Scornajenghi^{41a,41b}, F. Scuri^{72a}, F. Scutti¹⁰⁵, L. M. Scyboz¹¹⁵, C. D. Sebastiani⁹¹, P. Seema¹⁹, S. C. Seidel¹¹⁸, A. Seiden¹⁴⁵, B. D. Seidlitz²⁹, T. Seiss³⁷, C. Seitz⁴⁶, J. M. Seixas^{81b}, G. Sekhniaidze^{70a}, S. J. Sekula⁴², N. Semprini-Cesari^{23a,23b}, S. Sen⁴⁹, C. Serfon²⁹, L. Serin⁶⁵, L. Serkin^{67a,67b}, M. Sessa^{60a}, H. Severini¹²⁸, S. Sevova¹⁵², F. Sforza^{55a,55b}, A. Sfyrla⁵⁴, E. Shabalina⁵³, J. D. Shahinian¹⁴⁵, N. W. Shaikh^{45a,45b}, D. Shaked Renous¹⁷⁹, L. Y. Shan^{15a}, M. Shapiro¹⁸, A. Sharma¹³⁴, A. S. Sharma¹, P. B. Shatalov¹²⁴, K. Shaw¹⁵⁵, S. M. Shaw¹⁰¹, M. Shehade¹⁷⁹, Y. Shen¹²⁸, A. D. Sherman²⁵, P. Sherwood⁹⁵, L. Shi⁹⁵, S. Shimizu⁸², C. O. Shimmin¹⁸², Y. Shimogama¹⁷⁸, M. Shimojima¹¹⁶, I. P. J. Shipsey¹³⁴, S. Shirabe¹⁶⁴, M. Shiyakova^{80,z}, J. Shlomi¹⁷⁹, A. Shmeleva¹¹¹, M. J. Shochet³⁷, J. Shojaii¹⁰⁵, D. R. Shope¹²⁸, S. Shrestha¹²⁷, E. M. Shrif^{33e}, E. Shulga¹⁷⁹, P. Sicho¹⁴⁰, A. M. Sickles¹⁷², E. Sideras Haddad^{33e}, O. Sidiropoulou³⁶, A. Sidoti^{23a,23b}, F. Siegert⁴⁸, Dj. Sijacki¹⁶, M. Jr. Silva¹⁸⁰, M. V. Silva Oliveira³⁶, S. B. Silverstein^{45a}, S. Simion⁶⁵, R. Simoniello¹⁰⁰, C. J. Simpson-allso²¹, S. Simsek^{12b}, P. Sinervo¹⁶⁶, V. Sinetkii¹¹³, S. Singh¹⁵¹, M. Sioli^{23a,23b}, I. Siral¹³¹, S. Yu. Sivoklokov¹¹³, J. Sjölin^{45a,45b}, A. Skaf⁵³, E. Skorda⁹⁷, P. Skubic¹²⁸, M. Slawinska⁸⁵, K. Sliwa¹⁶⁹, R. Slovak¹⁴², V. Smakhtin¹⁷⁹, B. H. Smart¹⁴³, J. Smiesko^{28b}, N. Smirnov¹¹², S. Yu. Smirnov¹¹², Y. Smirnov¹¹², L. N. Smirnova^{113,r}, O. Smirnova⁹⁷, H. A. Smith¹³⁴, M. Smizanska⁹⁰, K. Smolek¹⁴¹, A. Smykiewicz⁸⁵, A. A. Snesarev¹¹¹, H. L. Snoek¹²⁰, I. M. Snyder¹³¹, S. Snyder²⁹, R. Sobie^{175,ab}, A. Soffer¹⁶⁰, A. Søgaard⁵⁰, F. Sohns⁵³, C. A. Solans Sanchez³⁶, E. Yu. Soldatov¹¹², U. Soldevila¹⁷³, A. A. Solodkov¹²³, A. Soloshenko⁸⁰, O. V. Solovyanov¹²³, V. Solovyev¹³⁷, P. Sommer¹⁴⁸, H. Son¹⁶⁹, W. Song¹⁴³, W. Y. Song^{167b}, A. Sopczak¹⁴¹, A. L. Sopio⁹⁵, F. Sopkova^{28b}, S. Sottocornola^{71a,71b}, R. Soualah^{67a,67c}, A. M. Soukharev^{122a,122b}, D. South⁴⁶, S. Spagnolo^{68a,68b}, M. Spalla¹¹⁵, M. Spangenberg¹⁷⁷, F. Spanò⁹⁴, D. Sperlich⁵², T. M. Spieker^{61a}, G. Spigo³⁶, M. Spina¹⁵⁵, D. P. Spiteri⁵⁷, M. Spousta¹⁴², A. Stabile^{69a,69b}, B. L. Stamas¹²¹, R. Stamen^{61a}, M. Stamenkovic¹²⁰, E. Stanekca⁸⁵, B. Stanislaus¹³⁴, M. M. Stanitzki⁴⁶, M. Stankaityte¹³⁴, B. Stapf¹²⁰, E. A. Starchenko¹²³, G. H. Stark¹⁴⁵, J. Stark⁵⁸, P. Staroba¹⁴⁰, P. Starovoitov^{61a}, S. Stärz¹⁰⁴, R. Staszewski⁸⁵, G. Stavropoulos⁴⁴, M. Stegler⁴⁶, P. Steinberg²⁹, A. L. Steinhebel¹³¹, B. Stelzer¹⁵¹, H. J. Stelzer¹³⁸, O. Stelzer-Chilton^{167a}, H. Stenzel⁵⁶, T. J. Stevenson¹⁵⁵, G. A. Stewart³⁶, M. C. Stockton³⁶, G. Stoicea^{27b}, M. Stolarski^{139a}, S. Stonjek¹¹⁵, A. Straessner⁴⁸, J. Strandberg¹⁵³, S. Strandberg^{45a,45b}, M. Strauss¹²⁸, T. Strebler¹⁰², P. Striznec^{28b}, R. Ströhmer¹⁷⁶, D. M. Strom¹³¹, R. Stroynowski⁴², A. Strubig⁵⁰, S. A. Stucci²⁹, B. Stugu¹⁷, J. Stupak¹²⁸, N. A. Styles⁴⁶, D. Su¹⁵², W. Su^{60c,147}, S. Suchek^{61a}, V. V. Sulin¹¹¹, M. J. Sullivan⁹¹, D. M. S. Sultan⁵⁴, S. Sultansoy^{4c}, T. Sumida⁸⁶, S. Sun¹⁰⁶, X. Sun¹⁰¹, K. Suruliz¹⁵⁵, C. J. E. Suster¹⁵⁶, M. R. Sutton¹⁵⁵, S. Suzuki⁸², M. Svatos¹⁴⁰, M. Swiatlowski^{167a}, S. P. Swift², T. Swirski¹⁷⁶, A. Sydorenko¹⁰⁰, I. Sykora^{28a}, M. Sykora¹⁴², T. Sykora¹⁴², D. Ta¹⁰⁰, K. Tackmann^{46,x}, J. Taenzer¹⁶⁰, A. Taffard¹⁷⁰, R. Tafirout^{167a}, R. Takashima⁸⁷, K. Takeda⁸³, T. Takeshita¹⁴⁹, E. P. Takeva⁵⁰, Y. Takubo⁸², M. Talby¹⁰², A. A. Talyshev^{122a,122b}, K. C. Tam^{63b}, N. M. Tamir¹⁶⁰, J. Tanaka¹⁶², R. Tanaka⁶⁵, S. Tapia Araya¹⁷², S. Tapprogge¹⁰⁰, A. Tarek Abouelfadl Mohamed¹⁰⁷, S. Tarem¹⁵⁹, K. Tariq^{60b}, G. Tarna^{27b,d}, G. F. Tartarelli^{69a}, P. Tas¹⁴², M. Tasevsky¹⁴⁰, T. Tashiro⁸⁶, E. Tassi^{41a,41b}, A. Tavares Delgado^{139a}, Y. Tayalati^{35e}, A. J. Taylor⁵⁰, G. N. Taylor¹⁰⁵, W. Taylor^{167b}, H. Teagle⁹¹, A. S. Tee⁹⁰, R. Teixeira De Lima¹⁵², P. Teixeira-Dias⁹⁴, H. Ten Kate³⁶, J. J. Teoh¹²⁰, S. Terada⁸², K. Terashi¹⁶², J. Terron⁹⁹, S. Terzo¹⁴, M. Testa⁵¹

R. J. Teuscher^{166,ab}, S. J. Thais¹⁸², N. Themistokleous⁵⁰, T. Thevenaux-Pelzer⁴⁶, F. Thiele⁴⁰, D. W. Thomas⁹⁴, J. O. Thomas⁴², J. P. Thomas²¹, E. A. Thompson⁴⁶, P. D. Thompson²¹, E. Thomson¹³⁶, E. J. Thorpe⁹³, R. E. Ticse Torres⁵³, V. O. Tikhomirov^{111,ah}, Yu. A. Tikhonov^{122a,122b}, S. Timoshenko¹¹², P. Tipton¹⁸², S. Tisserant¹⁰², K. Todome^{23a,23b}, S. Todorova-Nova¹⁴², S. Todt⁴⁸, J. Tojo⁸⁸, S. Tokár^{28a}, K. Tokushuku⁸², E. Tolley¹²⁷, R. Tombs³², K. G. Tomiwa^{33e}, M. Tomoto¹¹⁷, L. Tompkins¹⁵², P. Tornambe¹⁰³, E. Torrence¹³¹, H. Torres⁴⁸, E. Torró Pastor¹⁴⁷, C. Tosciri¹³⁴, J. Toth^{102,aa}, D. R. Tovey¹⁴⁸, A. Traet¹⁷, C. J. Treado¹²⁵, T. Trefzger¹⁷⁶, F. Tresoldi¹⁵⁵, A. Tricoli²⁹, I. M. Trigger^{167a}, S. Trincaz-Duvoid¹³⁵, D. A. Trischuk¹⁷⁴, W. Trischuk¹⁶⁶, B. Trocmé⁵⁸, A. Trofymov⁶⁵, C. Troncon^{69a}, F. Trovato¹⁵⁵, L. Truong^{33c}, M. Trzebinski⁸⁵, A. Trzupek⁸⁵, F. Tsai⁴⁶, J.C-L. Tseng¹³⁴, P. V. Tsiarehka^{108,ac}, A. Tsigotis^{161,u}, V. Tsiskaridze¹⁵⁴, E. G. Tskhadadze^{158a}, M. Tsopoulou¹⁶¹, I. I. Tsukerman¹²⁴, V. Tsulaia¹⁸, S. Tsuno⁸², D. Tsybychev¹⁵⁴, Y. Tu^{63b}, A. Tudorache^{27b}, V. Tudorache^{27b}, T. T. Tulbure^{27a}, A. N. Tuna⁵⁹, S. Turchikhin⁸⁰, D. Turgeman¹⁷⁹, I. Turk Cakir^{4b,s}, R. J. Turner²¹, R. Turra^{69a}, P. M. Tuts³⁹, S. Tzamarias¹⁶¹, E. Tzovara¹⁰⁰, K. Uchida¹⁶², F. Ukegawa¹⁶⁸, G. Unal³⁶, M. Unal¹¹, A. Undrus²⁹, G. Unel¹⁷⁰, F. C. Ungaro¹⁰⁵, Y. Unno⁸², K. Uno¹⁶², J. Urban^{28b}, P. Urquijo¹⁰⁵, G. Usai⁸, Z. Uysal^{12d}, V. Vacek¹⁴¹, B. Vachon¹⁰⁴, K. O. H. Vadla¹³³, T. Vafeiadis³⁶, A. Vaidya⁹⁵, C. Valderanis¹¹⁴, E. Valdes Santurio^{45a,45b}, M. Valente⁵⁴, S. Valentinetti^{23a,23b}, A. Valero¹⁷³, L. Valéry⁴⁶, R. A. Vallance²¹, A. Vallier³⁶, J. A. Valls Ferrer¹⁷³, T. R. Van Daalen¹⁴, P. Van Gemmeren⁶, I. Van Vulpen¹²⁰, M. Vanadia^{74a,74b}, W. Vandelli³⁶, M. Vandenbroucke¹⁴⁴, E. R. Vandewall¹²⁹, A. Vaniachine¹⁶⁵, D. Vannicola^{73a,73b}, R. Vari^{73a}, E. W. Varnes⁷, C. Varni^{55a,55b}, T. Varol¹⁵⁷, D. Varouchas⁶⁵, K. E. Varvell¹⁵⁶, M. E. Vasile^{27b}, G. A. Vasquez¹⁷⁵, F. Vazeille³⁸, D. Vazquez Furelos¹⁴, T. Vazquez Schroeder³⁶, J. Veatch⁵³, V. Vecchio¹⁰¹, M. J. Veen¹²⁰, L. M. Veloce¹⁶⁶, F. Veloso^{139a,139c}, S. Veneziano^{73a}, A. Ventura^{68a,68b}, A. Verbytskyi¹¹⁵, V. Vercesi^{71a}, M. Verducci^{72a,72b}, C. M. Vergel Infante⁷⁹, C. Vergis²⁴, W. Verkerke¹²⁰, A. T. Vermeulen¹²⁰, J. C. Vermeulen¹²⁰, C. Vernieri¹⁵², M. C. Vetterli^{151,al}, N. Viaux Maira^{146d}, T. Vickey¹⁴⁸, O. E. Vickey Boeriu¹⁴⁸, G. H. A. Viehhauser¹³⁴, L. Vigani^{61b}, M. Villa^{23a,23b}, M. Villaplana Perez³, E. M. Villhauer⁵⁰, E. Vilucchi⁵¹, M. G. Vincker³⁴, G. S. Virdee²¹, A. Vishwakarma⁵⁰, C. Vittori^{23a,23b}, I. Vivarelli¹⁵⁵, M. Vogel¹⁸¹, P. Vokac¹⁴¹, S. E. von Buddenbrock^{33e}, E. Von Toerne²⁴, V. Vorobel¹⁴², K. Vorobev¹¹², M. Vos¹⁷³, J. H. Vosseveld⁹¹, M. Vozak¹⁰¹, N. Vranjes¹⁶, M. Vranjes Milosavljevic¹⁶, V. Vrba¹⁴¹, M. Vreeswijk¹²⁰, R. Vuillermet³⁶, I. Vukotic³⁷, S. Wada¹⁶⁸, P. Wagner²⁴, W. Wagner¹⁸¹, J. Wagner-Kuhr¹¹⁴, S. Wahdan¹⁸¹, H. Wahlberg⁸⁹, R. Wakasa¹⁶⁸, V. M. Walbrecht¹¹⁵, J. Walder⁹⁰, R. Walker¹¹⁴, S. D. Walker⁹⁴, W. Walkowiak¹⁵⁰, V. Wallangen^{45a,45b}, A. M. Wang⁵⁹, A. Z. Wang¹⁸⁰, C. Wang^{60a}, C. Wang^{60c}, F. Wang¹⁸⁰, H. Wang¹⁸, H. Wang³, J. Wang^{63a}, P. Wang⁴², Q. Wang¹²⁸, R.-J. Wang¹⁰⁰, R. Wang^{60a}, R. Wang⁶, S. M. Wang¹⁵⁷, W. T. Wang^{60a}, W. Wang^{15c}, W. X. Wang^{60a}, Y. Wang^{60a}, Z. Wang¹⁰⁶, C. Wanotayaroj⁴⁶, A. Warburton¹⁰⁴, C. P. Ward³², D. R. Wardrop⁹⁵, N. Warrack⁵⁷, A. T. Watson²¹, M. F. Watson²¹, G. Watts¹⁴⁷, B. M. Waugh⁹⁵, A. F. Webb¹¹, C. Weber²⁹, M. S. Weber²⁰, S. A. Weber³⁴, S. M. Weber^{61a}, A. R. Weidberg¹³⁴, J. Weingarten⁴⁷, M. Weirich¹⁰⁰, C. Weiser⁵², P. S. Wells³⁶, T. Wenaus²⁹, B. Wendland⁴⁷, T. Wengler³⁶, S. Wenig³⁶, N. Wermes²⁴, M. Wessels^{61a}, T. D. Weston²⁰, K. Whalen¹³¹, N. L. Whallon¹⁴⁷, A. M. Wharton⁹⁰, A. S. White¹⁰⁶, A. White⁸, M. J. White¹, D. Whiteson¹⁷⁰, B. W. Whitmore⁹⁰, W. Wiedenmann¹⁸⁰, C. Wiel⁴⁸, M. Wielers¹⁴³, N. Wieseotte¹⁰⁰, C. Wiglesworth⁴⁰, L. A. M. Wiik-Fuchs⁵², H. G. Wilkens³⁶, L. J. Wilkins⁹⁴, H. H. Williams¹³⁶, S. Williams³², S. Willocq¹⁰³, P. J. Windischhofer¹³⁴, I. Wingerter-Seez⁵, E. Winkels¹⁵⁵, F. Winklmeier¹³¹, B. T. Winter⁵², M. Wittgen¹⁵², M. Wobisch⁹⁶, A. Wolf¹⁰⁰, R. Wölker¹³⁴, J. Wollrath⁵², M. W. Wolter⁸⁵, H. Wolters^{139a,139c}, V. W. S. Wong¹⁷⁴, N. L. Woods¹⁴⁵, S. D. Worm⁴⁶, B. K. Wosiek⁸⁵, K. W. Woźniak⁸⁵, K. Wraight⁵⁷, S. L. Wu¹⁸⁰, X. Wu⁵⁴, Y. Wu^{60a}, J. Wuerzinger¹³⁴, T. R. Wyatt¹⁰¹, B. M. Wynne⁵⁰, S. Xella⁴⁰, L. Xia¹⁷⁷, J. Xiang^{63c}, X. Xiao¹⁰⁶, X. Xie^{60a}, I. Xiotidis¹⁵⁵, D. Xu^{15a}, H. Xu^{60a}, H. Xu^{60a}, L. Xu²⁹, T. Xu¹⁴⁴, W. Xu¹⁰⁶, Z. Xu^{60b}, Z. Xu¹⁵², B. Yabsley¹⁵⁶, S. Yacoub^{33a}, K. Yajima¹³², D. P. Yallup⁹⁵, N. Yamaguchi⁸⁸, Y. Yamaguchi¹⁶⁴, A. Yamamoto⁸², M. Yamatani¹⁶², T. Yamazaki¹⁶², Y. Yamazaki⁸³, J. Yan^{60c}, Z. Yan²⁵, H. J. Yang^{60c,60d}, H. T. Yang¹⁸, S. Yang^{60a}, T. Yang^{63c}, X. Yang^{60b,58}, Y. Yang¹⁶², Z. Yang^{60a}, W.-M. Yao¹⁸, Y. C. Yap⁴⁶, Y. Yasu⁸², E. Yatsenko^{60c}, H. Ye^{15c}, J. Ye⁴², S. Ye²⁹, I. Yeletsikh⁸⁰, M. R. Yexley⁹⁰, E. Yigitbasi²⁵, P. Yin³⁹, K. Yorita¹⁷⁸, K. Yoshihara⁷⁹, C. J. S. Young³⁶, C. Young¹⁵², J. Yu⁷⁹, R. Yuan^{60b,h}, X. Yue^{61a}, M. Zaazoua^{35e}, B. Zabinski⁸⁵, G. Zacharis¹⁰, E. Zaffaroni⁵⁴, J. Zahreddine¹³⁵, A. M. Zaitsev^{123,ag}, T. Zakareishvili^{158b}, N. Zakharchuk³⁴, S. Zambito³⁶, D. Zanzi³⁶, D. R. Zaripovas⁵⁷, S. V. Zeifner⁴⁷, C. Zeitnitz¹⁸¹, G. Zemaityte¹³⁴, J. C. Zeng¹⁷², O. Zenin¹²³, T. Ženiš^{28a}, D. Zerwas⁶⁵, M. Zgubić¹³⁴, B. Zhang^{15c}, D. F. Zhang^{15b}, G. Zhang^{15b}, J. Zhang⁶, Kaili. Zhang^{15a}, L. Zhang^{15c}, L. Zhang^{60a}, M. Zhang¹⁷², R. Zhang¹⁸⁰, S. Zhang¹⁰⁶, X. Zhang^{60c}

X. Zhang^{60b} , Y. Zhang^{15a,15d} , Z. Zhang^{63a}, Z. Zhang⁶⁵ , P. Zhao⁴⁹ , Z. Zhao^{60a}, A. Zhemchugov⁸⁰ , Z. Zheng¹⁰⁶, D. Zhong¹⁷² , B. Zhou¹⁰⁶, C. Zhou¹⁸⁰ , H. Zhou⁷ , M. S. Zhou^{15a,15d} , M. Zhou¹⁵⁴ , N. Zhou^{60c} , Y. Zhou⁷, C. G. Zhu^{60b} , C. Zhu^{15a,15d} , H. L. Zhu^{60a} , H. Zhu^{15a} , J. Zhu¹⁰⁶ , Y. Zhu^{60a} , X. Zhuang^{15a} , K. Zhukov¹¹¹ , V. Zhulanov^{122a,122b} , D. Zieminska⁶⁶ , N. I. Zimine⁸⁰ , S. Zimmermann⁵² , Z. Zinonos¹¹⁵, M. Ziolkowski¹⁵⁰, L. Živković¹⁶ , G. Zobernig¹⁸⁰ , A. Zoccoli^{23a,23b} , K. Zoch⁵³ , T. G. Zorbas¹⁴⁸ , R. Zou³⁷ , L. Zwalinski³⁶ 

- ¹ Department of Physics, University of Adelaide, Adelaide, Australia
- ² Physics Department, SUNY Albany, Albany, NY, USA
- ³ Department of Physics, University of Alberta, Edmonton, AB, Canada
- ⁴ (a)Department of Physics, Ankara University, Ankara, Turkey; (b)Application and Research Center for Advanced Studies, Istanbul Aydin University, Istanbul, Turkey; (c)Division of Physics, TOBB University of Economics and Technology, Ankara, Turkey
- ⁵ LAPP, Université Grenoble Alpes, Université Savoie Mont Blanc, CNRS/IN2P3, Annecy, France
- ⁶ High Energy Physics Division, Argonne National Laboratory, Argonne, IL, USA
- ⁷ Department of Physics, University of Arizona, Tucson, AZ, USA
- ⁸ Department of Physics, University of Texas at Arlington, Arlington, TX, USA
- ⁹ Physics Department, National and Kapodistrian University of Athens, Athens, Greece
- ¹⁰ Physics Department, National Technical University of Athens, Zografou, Greece
- ¹¹ Department of Physics, University of Texas at Austin, Austin, TX, USA
- ¹² (a)Faculty of Engineering and Natural Sciences, Bahcesehir University, Istanbul, Turkey; (b)Faculty of Engineering and Natural Sciences, Istanbul Bilgi University, Istanbul, Turkey; (c)Department of Physics, Bogazici University, Istanbul, Turkey; (d)Department of Physics Engineering, Gaziantep University, Gaziantep, Turkey
- ¹³ Institute of Physics, Azerbaijan Academy of Sciences, Baku, Azerbaijan
- ¹⁴ Institut de Física d'Altes Energies (IFAE), Barcelona Institute of Science and Technology, Barcelona, Spain
- ¹⁵ (a)Institute of High Energy Physics, Chinese Academy of Sciences, Beijing, China; (b)Physics Department, Tsinghua University, Beijing, China; (c)Department of Physics, Nanjing University, Nanjing, China; (d)University of Chinese Academy of Science (UCAS), Beijing, China
- ¹⁶ Institute of Physics, University of Belgrade, Belgrade, Serbia
- ¹⁷ Department for Physics and Technology, University of Bergen, Bergen, Norway
- ¹⁸ Physics Division, Lawrence Berkeley National Laboratory and University of California, Berkeley, CA, USA
- ¹⁹ Institut für Physik, Humboldt Universität zu Berlin, Berlin, Germany
- ²⁰ Albert Einstein Center for Fundamental Physics and Laboratory for High Energy Physics, University of Bern, Bern, Switzerland
- ²¹ School of Physics and Astronomy, University of Birmingham, Birmingham, UK
- ²² (a)Facultad de Ciencias y Centro de Investigaciones, Universidad Antonio Nariño, Bogotá, Colombia; (b)Departamento de Física, Universidad Nacional de Colombia, Bogotá, Colombia, Colombia
- ²³ (a)Dipartimento di Fisica, INFN Bologna and Università di Bologna, Bologna, Italy; (b)INFN Sezione di Bologna, Bologna, Italy
- ²⁴ Physikalisches Institut, Universität Bonn, Bonn, Germany
- ²⁵ Department of Physics, Boston University, Boston, MA, USA
- ²⁶ Department of Physics, Brandeis University, Waltham, MA, USA
- ²⁷ (a)Transilvania University of Brasov, Brasov, Romania; (b)Horia Hulubei National Institute of Physics and Nuclear Engineering, Bucharest, Romania; (c)Department of Physics, Alexandru Ioan Cuza University of Iasi, Iasi, Romania; (d)Physics Department, National Institute for Research and Development of Isotopic and Molecular Technologies, Cluj-Napoca, Romania; (e)University Politehnica Bucharest, Bucharest, Romania; (f)West University in Timisoara, Timisoara, Romania
- ²⁸ (a)Faculty of Mathematics, Physics and Informatics, Comenius University, Bratislava, Slovak Republic; (b)Department of Subnuclear Physics, Institute of Experimental Physics of the Slovak Academy of Sciences, Kosice, Slovak Republic
- ²⁹ Physics Department, Brookhaven National Laboratory, Upton, NY, USA
- ³⁰ Departamento de Física, Universidad de Buenos Aires, Buenos Aires, Argentina
- ³¹ California State University, CA, USA
- ³² Cavendish Laboratory, University of Cambridge, Cambridge, UK

- 33 (a)Department of Physics, University of Cape Town, Cape Town, South Africa; (b)iThemba Labs, Western Cape, South Africa; (c)Department of Mechanical Engineering Science, University of Johannesburg, Johannesburg, South Africa; (d)Department of Physics, University of South Africa, Pretoria, South Africa; (e)School of Physics, University of the Witwatersrand, Johannesburg, South Africa
- 34 Department of Physics, Carleton University, Ottawa, ON, Canada
- 35 (a)Faculté des Sciences Ain Chock, Réseau Universitaire de Physique des Hautes Energies - Université Hassan II, Casablanca, Morocco; (b)Faculté des Sciences, Université Ibn-Tofail, Kénitra, Morocco; (c)Faculté des Sciences Semlalia, Université Cadi Ayyad, LPHEA, Marrakech, Morocco; (d)Faculté des Sciences, Université Mohamed Premier and LPTPM, Oujda, Morocco; (e)Faculté des sciences, Université Mohammed V, Rabat, Morocco
- 36 CERN, Geneva, Switzerland
- 37 Enrico Fermi Institute, University of Chicago, Chicago, IL, USA
- 38 LPC, Université Clermont Auvergne, CNRS/IN2P3, Clermont-Ferrand, France
- 39 Nevis Laboratory, Columbia University, Irvington, NY, USA
- 40 Niels Bohr Institute, University of Copenhagen, Copenhagen, Denmark
- 41 (a)Dipartimento di Fisica, Università della Calabria, Rende, Italy; (b)INFN Gruppo Collegato di Cosenza, Laboratori Nazionali di Frascati, Italy
- 42 Physics Department, Southern Methodist University, Dallas, TX, USA
- 43 Physics Department, University of Texas at Dallas, Richardson, TX, USA
- 44 National Centre for Scientific Research “Demokritos”, Agia Paraskevi, Greece
- 45 (a)Department of Physics, Stockholm University, Stockholm, Sweden; (b)Oskar Klein Centre, Stockholm, Sweden
- 46 Deutsches Elektronen-Synchrotron DESY, Hamburg and Zeuthen, Germany
- 47 Lehrstuhl für Experimentelle Physik IV, Technische Universität Dortmund, Dortmund, Germany
- 48 Institut für Kern- und Teilchenphysik, Technische Universität Dresden, Dresden, Germany
- 49 Department of Physics, Duke University, Durham, NC, USA
- 50 SUPA - School of Physics and Astronomy, University of Edinburgh, Edinburgh, UK
- 51 INFN e Laboratori Nazionali di Frascati, Frascati, Italy
- 52 Physikalisches Institut, Albert-Ludwigs-Universität Freiburg, Freiburg, Germany
- 53 II. Physikalisches Institut, Georg-August-Universität Göttingen, Göttingen, Germany
- 54 Département de Physique Nucléaire et Corpusculaire, Université de Genève, Genève, Switzerland
- 55 (a)Dipartimento di Fisica, Università di Genova, Genova, Italy; (b)INFN Sezione di Genova, Genova, Italy
- 56 II. Physikalisches Institut, Justus-Liebig-Universität Giessen, Giessen, Germany
- 57 SUPA - School of Physics and Astronomy, University of Glasgow, Glasgow, UK
- 58 LPSC, Université Grenoble Alpes, CNRS/IN2P3, Grenoble INP, Grenoble, France
- 59 Laboratory for Particle Physics and Cosmology, Harvard University, Cambridge, MA, USA
- 60 (a)Department of Modern Physics and State Key Laboratory of Particle Detection and Electronics, University of Science and Technology of China, Hefei, China; (b)Institute of Frontier and Interdisciplinary Science and Key Laboratory of Particle Physics and Particle Irradiation (MOE), Shandong University, Qingdao, China; (c)School of Physics and Astronomy, Shanghai Jiao Tong University, KLPPAC-MoE, SKLPPC, Shanghai, China; (d)Tsung-Dao Lee Institute, Shanghai, China
- 61 (a)Kirchhoff-Institut für Physik, Ruprecht-Karls-Universität Heidelberg, Heidelberg, Germany; (b)Physikalisches Institut, Ruprecht-Karls-Universität Heidelberg, Heidelberg, Germany
- 62 Faculty of Applied Information Science, Hiroshima Institute of Technology, Hiroshima, Japan
- 63 (a)Department of Physics, Chinese University of Hong Kong, Shatin, N.T., Hong Kong, China; (b)Department of Physics, University of Hong Kong, Hong Kong, China; (c)Department of Physics and Institute for Advanced Study, Hong Kong University of Science and Technology, Clear Water Bay, Kowloon, Hong Kong, China
- 64 Department of Physics, National Tsing Hua University, Hsinchu, Taiwan
- 65 IJCLab, Université Paris-Saclay, CNRS/IN2P3, 91405, Orsay, France
- 66 Department of Physics, Indiana University, Bloomington, IN, USA
- 67 (a)INFN Gruppo Collegato di Udine, Sezione di Trieste, Udine, Italy; (b)ICTP, Trieste, Italy; (c)Dipartimento Politecnico di Ingegneria e Architettura, Università di Udine, Udine, Italy
- 68 (a)INFN Sezione di Lecce, Lecce, Italy; (b)Dipartimento di Matematica e Fisica, Università del Salento, Lecce, Italy
- 69 (a)INFN Sezione di Milano, Milano, Italy; (b)Dipartimento di Fisica, Università di Milano, Milano, Italy
- 70 (a)INFN Sezione di Napoli, Napoli, Italy; (b)Dipartimento di Fisica, Università di Napoli, Napoli, Italy

- 71 (a) INFN Sezione di Pavia, Pavia, Italy; (b) Dipartimento di Fisica, Università di Pavia, Pavia, Italy
- 72 (a) INFN Sezione di Pisa, Pisa, Italy; (b) Dipartimento di Fisica E. Fermi, Università di Pisa, Pisa, Italy
- 73 (a) INFN Sezione di Roma, Roma, Italy; (b) Dipartimento di Fisica, Sapienza Università di Roma, Roma, Italy
- 74 (a) INFN Sezione di Roma Tor Vergata, Roma, Italy; (b) Dipartimento di Fisica, Università di Roma Tor Vergata, Roma, Italy
- 75 (a) INFN Sezione di Roma Tre, Roma, Italy; (b) Dipartimento di Matematica e Fisica, Università Roma Tre, Roma, Italy
- 76 (a) INFN-TIFPA, Trento, Italy; (b) Università degli Studi di Trento, Trento, Italy
- 77 Institut für Astro- und Teilchenphysik, Leopold-Franzens-Universität, Innsbruck, Austria
- 78 University of Iowa, Iowa City, IA, USA
- 79 Department of Physics and Astronomy, Iowa State University, Ames, IA, USA
- 80 Joint Institute for Nuclear Research, Dubna, Russia
- 81 (a) Departamento de Engenharia Elétrica, Universidade Federal de Juiz de Fora (UFJF), Juiz de Fora, São Paulo, Brazil; (b) Universidade Federal do Rio De Janeiro COPPE/EE/IF, Rio de Janeiro, São Paulo, Brazil; (c) Universidade Federal de São João del Rei (UFSJ), São João del Rei, São Paulo, Brazil; (d) Instituto de Física, Universidade de São Paulo, São Paulo, Brazil
- 82 KEK, High Energy Accelerator Research Organization, Tsukuba, Japan
- 83 Graduate School of Science, Kobe University, Kobe, Japan
- 84 (a) Faculty of Physics and Applied Computer Science, AGH University of Science and Technology, Krakow, Poland; (b) Marian Smoluchowski Institute of Physics, Jagiellonian University, Krakow, Poland
- 85 Institute of Nuclear Physics Polish Academy of Sciences, Krakow, Poland
- 86 Faculty of Science, Kyoto University, Kyoto, Japan
- 87 Kyoto University of Education, Kyoto, Japan
- 88 Research Center for Advanced Particle Physics and Department of Physics, Kyushu University, Fukuoka, Japan
- 89 Instituto de Física La Plata, Universidad Nacional de La Plata and CONICET, La Plata, Argentina
- 90 Physics Department, Lancaster University, Lancaster, UK
- 91 Oliver Lodge Laboratory, University of Liverpool, Liverpool, UK
- 92 Department of Experimental Particle Physics, Jožef Stefan Institute and Department of Physics, University of Ljubljana, Ljubljana, Slovenia
- 93 School of Physics and Astronomy, Queen Mary University of London, London, UK
- 94 Department of Physics, Royal Holloway University of London, Egham, UK
- 95 Department of Physics and Astronomy, University College London, London, UK
- 96 Louisiana Tech University, Ruston, LA, USA
- 97 Fysiska institutionen, Lunds universitet, Lund, Sweden
- 98 Centre de Calcul de l'Institut National de Physique Nucléaire et de Physique des Particules (IN2P3), Villeurbanne, France
- 99 Departamento de Física Teórica C-15 and CIAFF, Universidad Autónoma de Madrid, Madrid, Spain
- 100 Institut für Physik, Universität Mainz, Mainz, Germany
- 101 School of Physics and Astronomy, University of Manchester, Manchester, UK
- 102 CPPM, Aix-Marseille Université, CNRS/IN2P3, Marseille, France
- 103 Department of Physics, University of Massachusetts, Amherst, MA, USA
- 104 Department of Physics, McGill University, Montreal, QC, Canada
- 105 School of Physics, University of Melbourne, Victoria, Australia
- 106 Department of Physics, University of Michigan, Ann Arbor, MI, USA
- 107 Department of Physics and Astronomy, Michigan State University, East Lansing, MI, USA
- 108 B.I. Stepanov Institute of Physics, National Academy of Sciences of Belarus, Minsk, Belarus
- 109 Research Institute for Nuclear Problems of Byelorussian State University, Minsk, Belarus
- 110 Group of Particle Physics, University of Montreal, Montreal, QC, Canada
- 111 P.N. Lebedev Physical Institute of the Russian Academy of Sciences, Moscow, Russia
- 112 National Research Nuclear University MEPhI, Moscow, Russia
- 113 D.V. Skobel'syn Institute of Nuclear Physics, M.V. Lomonosov Moscow State University, Moscow, Russia
- 114 Fakultät für Physik, Ludwig-Maximilians-Universität München, München, Germany
- 115 Max-Planck-Institut für Physik (Werner-Heisenberg-Institut), München, Germany
- 116 Nagasaki Institute of Applied Science, Nagasaki, Japan

- 117 Graduate School of Science and Kobayashi-Maskawa Institute, Nagoya University, Nagoya, Japan
- 118 Department of Physics and Astronomy, University of New Mexico, Albuquerque, NM, USA
- 119 Institute for Mathematics, Astrophysics and Particle Physics, Radboud University Nijmegen/Nikhef, Nijmegen, The Netherlands
- 120 Nikhef National Institute for Subatomic Physics and University of Amsterdam, Amsterdam, The Netherlands
- 121 Department of Physics, Northern Illinois University, DeKalb, IL, USA
- 122 (a) Budker Institute of Nuclear Physics and NSU, SB RAS, Novosibirsk, Russia; (b) Novosibirsk State University, Novosibirsk, Russia
- 123 Institute for High Energy Physics of the National Research Centre Kurchatov Institute, Protvino, Russia
- 124 Institute for Theoretical and Experimental Physics named by A.I. Alikhanov of National Research Centre “Kurchatov Institute”, Moscow, Russia
- 125 Department of Physics, New York University, New York, NY, USA
- 126 Ochanomizu University, Otsuka, Bunkyo-ku, Tokyo, Japan
- 127 Ohio State University, Columbus, OH, USA
- 128 Homer L. Dodge Department of Physics and Astronomy, University of Oklahoma, Norman, OK, USA
- 129 Department of Physics, Oklahoma State University, Stillwater, OK, USA
- 130 Palacký University, RCPTM, Joint Laboratory of Optics, Olomouc, Czech Republic
- 131 Institute for Fundamental Science, University of Oregon, Eugene, OR, USA
- 132 Graduate School of Science, Osaka University, Osaka, Japan
- 133 Department of Physics, University of Oslo, Oslo, Norway
- 134 Department of Physics, Oxford University, Oxford, UK
- 135 LPNHE, Sorbonne Université, Université de Paris, CNRS/IN2P3, Paris, France
- 136 Department of Physics, University of Pennsylvania, Philadelphia, PA, USA
- 137 Konstantinov Nuclear Physics Institute of National Research Centre “Kurchatov Institute”, PNPI, St. Petersburg, Russia
- 138 Department of Physics and Astronomy, University of Pittsburgh, Pittsburgh, PA, USA
- 139 (a) Laboratório de Instrumentação e Física Experimental de Partículas - LIP, Lisboa, Portugal; (b) Departamento de Física, Faculdade de Ciências, Universidade de Lisboa, Lisboa, Portugal; (c) Departamento de Física, Universidade de Coimbra, Coimbra, Portugal; (d) Centro de Física Nuclear da Universidade de Lisboa, Lisboa, Portugal; (e) Departamento de Física, Universidade do Minho, Braga, Portugal; (f) Departamento de Física Teórica y del Cosmos, Universidad de Granada, Granada, Spain; (g) Dep Física and CEFITEC of Faculdade de Ciências e Tecnologia, Universidade Nova de Lisboa, Caparica, Portugal; (h) Instituto Superior Técnico, Universidade de Lisboa, Lisboa, Portugal
- 140 Institute of Physics of the Czech Academy of Sciences, Prague, Czech Republic
- 141 Czech Technical University in Prague, Prague, Czech Republic
- 142 Charles University, Faculty of Mathematics and Physics, Prague, Czech Republic
- 143 Particle Physics Department, Rutherford Appleton Laboratory, Didcot, UK
- 144 IRFU, CEA, Université Paris-Saclay, Gif-sur-Yvette, France
- 145 Santa Cruz Institute for Particle Physics, University of California Santa Cruz, Santa Cruz, CA, USA
- 146 (a) Departamento de Física, Pontificia Universidad Católica de Chile, Santiago, Chile; (b) Department of Physics, Universidad Andres Bello, Santiago, Chile; (c) Instituto de Alta Investigación, Universidad de Tarapacá, Santiago, Chile; (d) Departamento de Física, Universidad Técnica Federico Santa María, Valparaíso, Chile
- 147 Department of Physics, University of Washington, Seattle, WA, USA
- 148 Department of Physics and Astronomy, University of Sheffield, Sheffield, UK
- 149 Department of Physics, Shinshu University, Nagano, Japan
- 150 Department Physik, Universität Siegen, Siegen, Germany
- 151 Department of Physics, Simon Fraser University, Burnaby, BC, Canada
- 152 SLAC National Accelerator Laboratory, Stanford, CA, USA
- 153 Physics Department, Royal Institute of Technology, Stockholm, Sweden
- 154 Departments of Physics and Astronomy, Stony Brook University, Stony Brook, NY, USA
- 155 Department of Physics and Astronomy, University of Sussex, Brighton, UK
- 156 School of Physics, University of Sydney, Sydney, Australia
- 157 Institute of Physics, Academia Sinica, Taipei, Taiwan
- 158 (a) E. Andronikashvili Institute of Physics, Iv. Javakhishvili Tbilisi State University, Tbilisi, Georgia; (b) High Energy Physics Institute, Tbilisi State University, Tbilisi, Georgia

- 159 Department of Physics, Technion, Israel Institute of Technology, Haifa, Israel
- 160 Raymond and Beverly Sackler School of Physics and Astronomy, Tel Aviv University, Tel Aviv, Israel
- 161 Department of Physics, Aristotle University of Thessaloniki, Thessaloniki, Greece
- 162 International Center for Elementary Particle Physics and Department of Physics, University of Tokyo, Tokyo, Japan
- 163 Graduate School of Science and Technology, Tokyo Metropolitan University, Tokyo, Japan
- 164 Department of Physics, Tokyo Institute of Technology, Tokyo, Japan
- 165 Tomsk State University, Tomsk, Russia
- 166 Department of Physics, University of Toronto, Toronto, ON, Canada
- 167 ^(a)TRIUMF, Vancouver, BC, Canada; ^(b)Department of Physics and Astronomy, York University, Toronto, ON, Canada
- 168 Division of Physics and Tomonaga Center for the History of the Universe, Faculty of Pure and Applied Sciences, University of Tsukuba, Tsukuba, Japan
- 169 Department of Physics and Astronomy, Tufts University, Medford, MA, USA
- 170 Department of Physics and Astronomy, University of California Irvine, Irvine, CA, USA
- 171 Department of Physics and Astronomy, University of Uppsala, Uppsala, Sweden
- 172 Department of Physics, University of Illinois, Urbana, IL, USA
- 173 Instituto de Física Corpuscular (IFIC), Centro Mixto Universidad de Valencia - CSIC, Valencia, Spain
- 174 Department of Physics, University of British Columbia, Vancouver, BC, Canada
- 175 Department of Physics and Astronomy, University of Victoria, Victoria, BC, Canada
- 176 Fakultät für Physik und Astronomie, Julius-Maximilians-Universität Würzburg, Würzburg, Germany
- 177 Department of Physics, University of Warwick, Coventry, UK
- 178 Waseda University, Tokyo, Japan
- 179 Department of Particle Physics, Weizmann Institute of Science, Rehovot, Israel
- 180 Department of Physics, University of Wisconsin, Madison, WI, USA
- 181 Fakultät für Mathematik und Naturwissenschaften, Fachgruppe Physik, Bergische Universität Wuppertal, Wuppertal, Germany
- 182 Department of Physics, Yale University, New Haven, CT, USA
- ^a Also at Borough of Manhattan Community College, City University of New York, New York NY, USA
- ^b Also at Centro Studi e Ricerche Enrico Fermi, Italy
- ^c Also at CERN, Geneva, Switzerland
- ^d Also at CPPM, Aix-Marseille Université, CNRS/IN2P3, Marseille, France
- ^e Also at Département de Physique Nucléaire et Corpusculaire, Université de Genève, Genève, Switzerland
- ^f Also at Departament de Física de la Universitat Autònoma de Barcelona, Barcelona, Spain
- ^g Also at Department of Financial and Management Engineering, University of the Aegean, Chios, Greece
- ^h Also at Department of Physics and Astronomy, Michigan State University, East Lansing MI, USA
- ⁱ Also at Department of Physics and Astronomy, University of Louisville, Louisville, KY, USA
- ^j Also at Department of Physics, Ben Gurion University of the Negev, Beer Sheva, Israel
- ^k Also at Department of Physics, California State University, East Bay, USA
- ^l Also at Department of Physics, California State University, Fresno, USA
- ^m Also at Department of Physics, California State University, Sacramento, USA
- ⁿ Also at Department of Physics, King's College London, London, UK
- ^o Also at Department of Physics, St. Petersburg State Polytechnical University, St. Petersburg, Russia
- ^p Also at Department of Physics, University of Fribourg, Fribourg, Switzerland
- ^q Also at Dipartimento di Matematica, Informatica e Fisica, Università di Udine, Udine, Italy
- ^r Also at Faculty of Physics, M.V. Lomonosov Moscow State University, Moscow, Russia
- ^s Also at Giresun University, Faculty of Engineering, Giresun, Turkey
- ^t Also at Graduate School of Science, Osaka University, Osaka, Japan
- ^u Also at Hellenic Open University, Patras, Greece
- ^v Also at IJCLab, Université Paris-Saclay, CNRS/IN2P3, 91405, Orsay, France
- ^w Also at Institutio Catalana de Recerca i Estudis Avancats, ICREA, Barcelona, Spain
- ^x Also at Institut für Experimentalphysik, Universität Hamburg, Hamburg, Germany
- ^y Also at Institute for Mathematics, Astrophysics and Particle Physics, Radboud University Nijmegen/Nikhef, Nijmegen, Netherlands

- ^{aa} Also at Institute for Nuclear Research and Nuclear Energy (INRNE) of the Bulgarian Academy of Sciences, Sofia, Bulgaria
- ^{ab} Also at Institute for Particle and Nuclear Physics, Wigner Research Centre for Physics, Budapest, Hungary.
- ^{ac} Also at Institute of Particle Physics (IPP), Vancouver, Canada
- ^{ad} Also at Institute of Physics, Azerbaijan Academy of Sciences, Baku, Azerbaijan
- ^{ae} Also at Instituto de Fisica Teorica, IFT-UAM/CSIC, Madrid, Spain
- ^{af} Also at Joint Institute for Nuclear Research, Dubna, Russia
- ^{ag} Also at Louisiana Tech University, Ruston LA, USA
- ^{ah} Also at Moscow Institute of Physics and Technology State University, Dolgoprudny, Russia
- ^{ai} Also at National Research Nuclear University MEPhI, Moscow, Russia
- ^{aj} Also at Physics Department, An-Najah National University, Nablus, Palestine
- ^{ak} Also at Physikalisches Institut, Albert-Ludwigs-Universität Freiburg, Freiburg, Germany
- ^{al} Also at The City College of New York, New York NY, USA
- ^{am} Also at TRIUMF, Vancouver BC, Canada.
- ^{an} Also at Universita di Napoli Parthenope, Napoli, Italy
- ^{ao} Also at University of Chinese Academy of Sciences (UCAS), Beijing, China.
- *Deceased